

# REPORT DOCUMENTATION PAGE

Form Approved OMB No. 0704-0188

Public reporting burden for this collection of information is estimated to average 1 hour per response, including the time for reviewing instructions, searching existing data sources, gathering and maintaining the data needed, and completing and reviewing the collection of information. Send comments regarding this burden estimate or any other aspect of this collection of information, including suggestions for reducing this burden to Washington Headquarters Services, Directorate for Information Operations and Reports, 1215 Jefferson Davis Highway, Suite 1204, Arlington, VA 22202-4302, and to the Office of Management and Budget, Paperwork Reduction Project (0704-0188), Washington, DC 20503.

1. AGENCY USE ONLY (Leave blank)		2. REPORT DATE July 2000	3. REPORT TYPE AND DATES COVERED Final Report	
4. TITLE AND SUBTITLE Active Materials For Lasing In The 4-5 Micron Spectral Range			5. FUNDING NUMBERS F61775-99-WE	
6. AUTHOR(S) Academician V. V. Osiko				
7. PERFORMING ORGANIZATION NAME(S) AND ADDRESS(ES) General Physics Institute of the RAS, 38 Vavilov str., Bld. D, Moscow 117942 Russia			8. PERFORMING ORGANIZATION REPORT NUMBER N/A	
9. SPONSORING/MONITORING AGENCY NAME(S) AND ADDRESS(ES) EOARD PSC 802 BOX 14 FPO 09499-0200			10. SPONSORING/MONITORING AGENCY REPORT NUMBER SPC 99-4033	
11. SUPPLEMENTARY NOTES Report is .pdf file. <i>Original Charts in color</i>				
12a. DISTRIBUTION/AVAILABILITY STATEMENT Approved for public release; distribution is unlimited.			12b. DISTRIBUTION CODE A	
13. ABSTRACT (Maximum 200 words)  This report results from a contract tasking General Physics Institute of the RAS, as follows: The contractor will investigate new laser host materials having a "short" phonon spectrum and doped with rare earths to achieve efficient, near-room-temperature operation of solid state lasers operating in the 4-5 micron spectral range.				
14. SUBJECT TERMS  EOARD, Mid-IR lasers, Solid state lasers			15. NUMBER OF PAGES 132	
			16. PRICE CODE N/A	
17. SECURITY CLASSIFICATION OF REPORT  UNCLASSIFIED	18. SECURITY CLASSIFICATION OF THIS PAGE  UNCLASSIFIED	19. SECURITY CLASSIFICATION OF ABSTRACT  UNCLASSIFIED	20. LIMITATION OF ABSTRACT  UL	

NSN 7540-01-280-5500

Standard Form 298 (Rev. 2-89)  
Prescribed by ANSI Std. Z39-18  
298-102

**RUSSIAN ACADEMY OF SCIENCES  
LASER MATERIALS AND TECHNOLOGIES RESEARCH  
CENTER OF GENERAL PHYSICS INSTITUTE**

**ACTIVE MATERIALS FOR LASING IN THE 4-5 MICRON  
SPECTRAL RANGE**

Final report

Contract No F61775-99-WE033

July, 2000

Moscow, Russia

20000907 085

## **Content**

### **Introduction**

**Chapter 1 Crystals and glasses doped with erbium ions.**

**Chapter 2 Crystals and glasses doped with dysprosium ions.**

**Chapter 3 Energy levels scheme analysis of holmium ion.**

**Chapter 4 Energy levels scheme of thulium ion.**

**Chapter 5 Energy levels scheme analysis of praseodymium ion.**

**Chapter 6 Energy levels scheme of neodymium ion.**

**Chapter 7 Nonradiative energy transfer and sensitization in fluoride co-doped with  $\text{Er}^{3+}$ - $\text{Ce}^{3+}$  and  $\text{Nd}^{3+}$ - $\text{Ce}^{3+}$  with respect to 4-5 micron laser transitions in  $\text{Ce}^{3+}$  ions.**

**Chapter 8 Pumping sources and cavities arrangement.**

**Chapter 9 The preparation and characterization of crystals and glasses.**

## **Chapter 1**

### **Crystals and glasses doped with erbium ions.**

#### **1.1 Energy level scheme analysis.**

First of all to choose appropriate electronic transitions for 4- 5  $\mu\text{m}$  lasing we analyzed energy level scheme of erbium ion. Fig. 1.1 presents erbium scheme of population inversion creation at the  $^4\text{I}_{9/2}$  state (4.9 $\mu\text{m}$  transition ( $^4\text{I}_{9/2} \rightarrow ^4\text{I}_{11/2}$ )) with the cooperative excitation in concentrated samples under the 1.54  $\mu\text{m}$  of erbium laser. Excitation by 1.54  $\mu\text{m}$  of erbium glass laser of two erbium ions into the  $^4\text{I}_{13/2}$  state is followed by up- conversion due to sequential sensitization from one excited ion to another excited ion with the summation of excitation energy. Here the term of up- conversion is used in the sense of the process opposite to cross- relaxation (down- conversion). As the result of up- conversion one of the excited erbium ions loses its excitation while the another one increases its excitation energy and goes into the  $^4\text{I}_{9/2}$  excited state which can be used as initial laser level for mid-IR oscillation. After that one step generation at 4.9  $\mu\text{m}$  ( $^4\text{I}_{9/2} \rightarrow ^4\text{I}_{11/2}$ ) or 2.7  $\mu\text{m}$  ( $^4\text{I}_{11/2} \rightarrow ^4\text{I}_{13/2}$ ) is expected. For each participated transition the column of the reduced matrix elements  $U(k)$  is presented in the Fig. 1.1.

In the Judd-Ofelt theory [1,2] the line strength for electric-dipole transition between  $\{\text{LSJ}\}$  states is expressed as

$$S_{ed}(J,J') = \sum_k \Omega_k |(SLJ \| U^{(k)} \| S'L'J')|^2 \quad (k=2,4,6), \quad (1.1)$$

where  $\Omega_k$  is intensity parameter and  $(SLJ \| U^{(k)} \| S'L'J')$  is the doubly reduced matrix element of the unit spherical operator of rank  $k$ .

Values of  $(SLJ \| U^{(k)} \| S'L'J')^2$  are listed in [3].

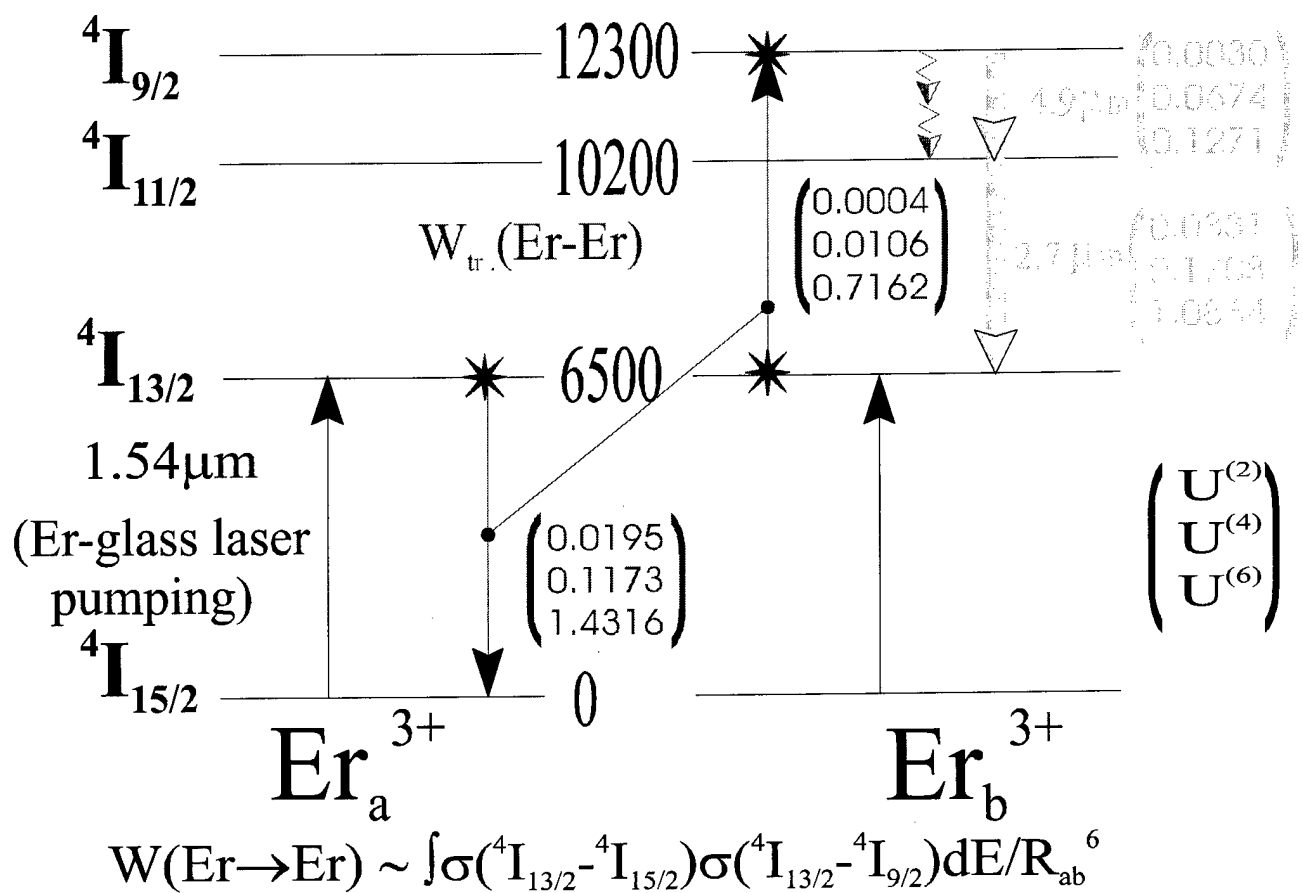
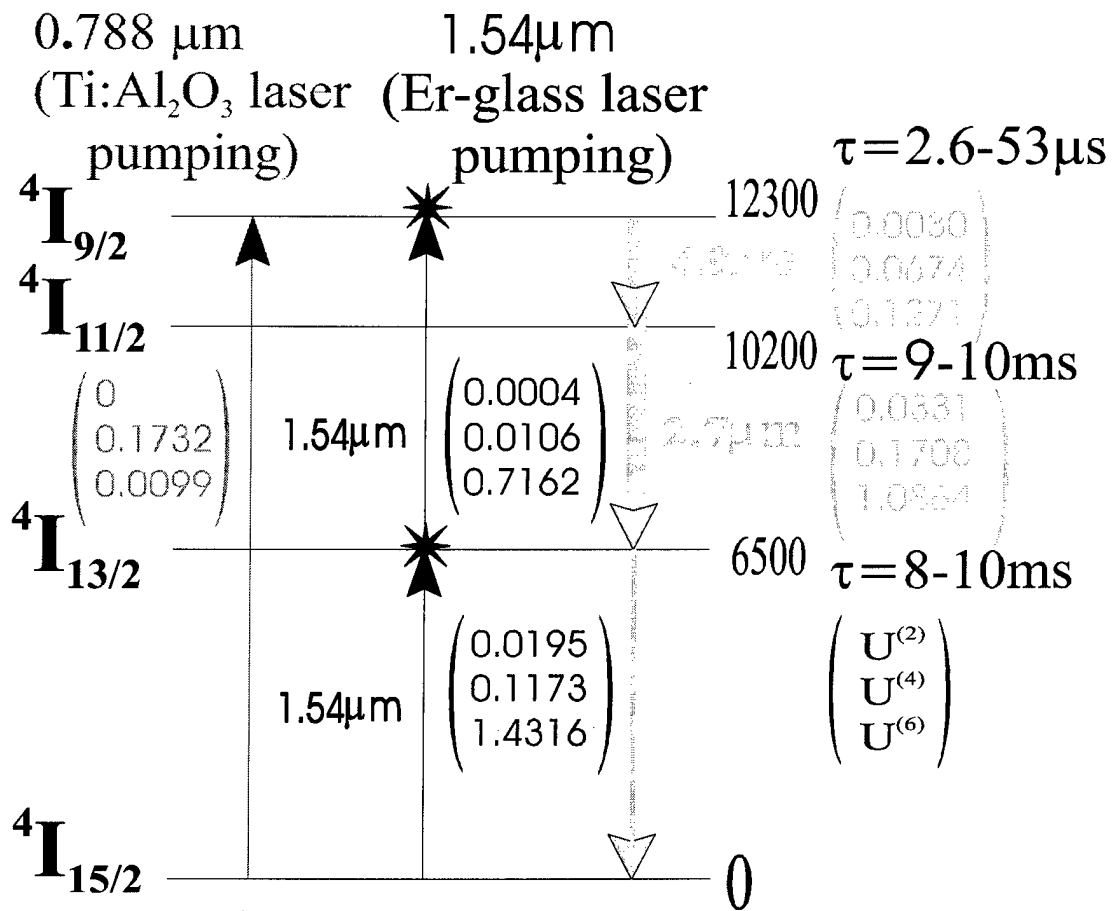


Fig. 1.1 Up-conversion  $\text{Er}^{3+}$  excitation scheme for 4.9  $\mu\text{m}$  lasing.



ZBLAN  $\Omega_4 = 2.82$   $\Omega_6 = 3.94 \times [10^{20} \text{cm}^{-2}]$

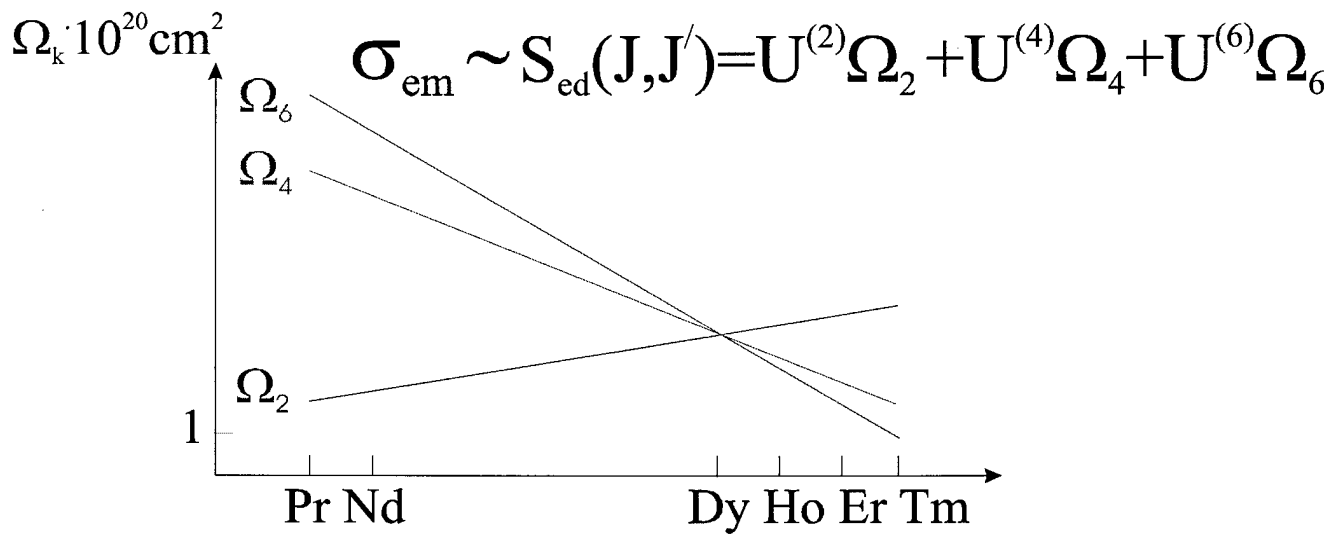


Fig. 1.2 Direct and two-step excitation of 4.9  $\mu\text{m}$  Er<sup>3+</sup> lasing transition  $4I_{9/2} \rightarrow 4I_{11/2}$ .

Having the intensity parameters  $\Omega_k$  one can determine the line strength  $S_{ed}(J, J')$  for all transitions within the 4f electronic configuration.

Reduced matrix element  $\langle LSJ || L + 2S || L'S'J' \rangle^2$  were evaluated from expression given elsewhere (see, as an example, [4]).

1.1 expression can be rewritten as the product of two matrixes

$$S_{ed}(J, J') = \begin{pmatrix} U(2) \\ U(4) \\ U(6) \end{pmatrix} \times (\Omega(2) \ \Omega(4) \ \Omega(6)). \quad (1.2)$$

The larger the matrix elements of the transition  $U(k)$  and the larger intensity parameters  $\Omega(k)$  the larger the line strength of the transition. Analysis of Fig. 1.1 shows that all transitions participated in the population inversion creation as well as in the depletion of the low laser level have large matrix elements  $U(6)$ , medium  $U(4)$  and low  $U(2)$ . 4.9  $\mu\text{m}$  laser transition shows 5- 10 times smaller matrix elements than pumping transition and 2.7  $\mu\text{m}$  laser transition. This is one of the difficulties to get oscillation and amplification at 4.9  $\mu\text{m}$  in erbium doped optical matrixes because  $\sigma_{em} \sim S_{ed}$ . For the laser scheme under consideration it is necessary to find out the solid state matrices (crystals or glasses) with the intensity parameters  $\Omega(4)$  and  $\Omega(6)$  as large as possible to have the larger lines strengths  $S_{ed}$  of pumping and laser transition. Our analysis of the dependence of available experimentally determined intensity parameters  $\Omega(k)$  in the doped crystals and glasses on the rare- earth ion type gives weak dependence for  $\Omega(2)$  and decrease of  $\Omega(4)$  and  $\Omega(6)$  from left to right in the row of rare- earth ions, i.e. from  $\text{Pr}^{3+}$  to  $\text{Tm}^{3+}$  (Fig. 1.2). Unfortunately, for most known erbium doped crystals and glasses the last two parameters are equal or even less than  $10^{-20}$ . From the literature analysis only ZBLAN glass has rather large  $\Omega(4) = 2.82 \times 10^{-20} \text{ cm}^2$  and  $\Omega(6) = 3.94 \times 10^{-20} \text{ cm}^2$ . For the crystals with fluorite structure these values are available for  $\text{SrF}_2$  ( $2.01 \times 10^{-20} \text{ cm}^2$  and  $1.34 \times 10^{-20} \text{ cm}^2$ , respectively).

Two step excitation of single  $\text{Er}^{3+}$  ion into the  ${}^4\text{I}_{9/2}$  state with the same erbium glass laser as well as direct laser excitation by  $\text{Ti}^{3+}:\text{Al}_2\text{O}_3$  is also leads to population inversion of the  ${}^4\text{I}_{9/2}$  initial laser level (Fig. 1.2). But from the analysis of the reduced matrix elements and absorption spectra of the pumping transitions it is seen that the direct pumping of the initial laser level by  $\text{Ti}:\text{Al}_2\text{O}_3$  laser is less effective because of smaller matrix elements  $U(2)=0$  and  $U(6)=0.0099$  for the  $({}^4\text{I}_{15/2} \rightarrow {}^4\text{I}_{9/2})$  transition in comparison with  $({}^4\text{I}_{15/2} \rightarrow {}^4\text{I}_{13/2})$  ( $U(2)=0.0195$ ;  $U(6)=1.4316$ ) and  $({}^4\text{I}_{13/2} \rightarrow {}^4\text{I}_{9/2})$  ( $U(2)=0.0004$ ;  $U(6)=0.7162$ ) ones.



## 1.2. Lifetimes measurements of the $^4I_{9/2}$ initial laser level of erbium ion in fluoride crystals

While choosing promising crystal matrixes for lasing in the mid-IR region we dwell on the fluorides with heavy cations. Our previous study shows that the multiphonon relaxation (MR) rate is proportional to the  $n$ -th power of the phonon factor  $\eta$  ( $W \sim \eta^n$ ) [5]. In its turn this factor is inversely proportional to the reduced mass of the lattice and the distance between rare- earth ion and the ligand  $R_0$ . Therefore, in order to decrease MR rate it is necessary to increase cation mass and the distance  $R_0$  (i.e. increase crystal lattice parameter  $a$ ) to decrease the phonon factor  $\eta$ . To check this we measured the kinetics of fluorescence decay of the  $^4I_{9/2}$  state of  $Er^{3+}$  in the series of crystals having fluorite type structure with increasing cation mass. The following series of crystals doped with different erbium concentrations was grown:  $CaF_2$ ,  $SrF_2$ ,  $CdF_2$ ,  $BaF_2$ , and  $PbF_2$ . The lattice parameter in this row of crystals is also increase (see Table 1.1). The exceptions are  $CdF_2$ , which has the lowest lattice parameter and  $PbF_2$ , which has smaller lattice parameter than  $BaF_2$ . Fluorescence was excited by Ti- Sapphire laser pumped by second harmonics of YAG: Nd pulsed laser ( $t_p = 100$  ns) and registered at the  $^4I_{9/2} \rightarrow ^4I_{15/2}$  resonant transition using interference filter IF 825 (Carl Zeiss, Germany) and grating monochromator for fluorescence selection. PMT FEU-83 and digital oscilloscope Tektronix TDS- 380 with 350MHz bandwidth were used for signal registration, acquisition and averaging. By slow tuning of excitation wavelength of the Ti- Sapphire laser we get off the resonance of the second energy photon with the  $^4I_{9/2} \rightarrow ^2H_{9/2}$  transition. The second photon absorption is characterized by strong green luminescence at the  $^4S_{3/2} \rightarrow ^4I_{15/2}$  transition after fast multiphonon relaxation from the  $^2H_{9/2}$  state. So, we tried to minimize it to the best advantage because this process change significantly the kinetics behavior of the population for all participated multiplets. Most of the

measured kinetics of fluorescence decay were nonexponential (Fig. 1.3) because of different optical centers existed in the rare- earth doped crystals with fluorite structure. The results of measurements of the lifetimes at the final stage of kinetics decay for low erbium concentrations at room temperature are presented in Table 1.1. It is seen that lifetime increases with the cation mass except for  $\text{CdF}_2$  and  $\text{PbF}_2$  because of smaller lattice parameter  $a$  which increases the multiphonon relaxation rate which in its turn decreases  $\tau$ . This is in consistence with the nonlinear theory of multiphonon relaxation. The detailed analysis of this dependence will be the subject of future studies. The largest lifetime was obtained in  $\text{BaF}_2$ . Increasing lifetime gives rise to the fluorescence quantum yield.

- 1 -  $\text{CdF}_2:\text{ErF}_3$  (1 mol.%)  $\tau=7.7 \mu\text{s}$
- 2 -  $\text{BaF}_2:\text{ErF}_3$  (0.3 mol.%)  $\tau=40 \mu\text{s}$
- 3 -  $\text{PbF}_2:\text{ErF}_3$  (2 mol.%)  $\tau=33.2 \mu\text{s}$
- 4 -  $\text{CaF}_2:\text{ErF}_3$  (0.03 mol.%)  $\tau=1.07 \mu\text{s}$
- 5 -  $\text{SrF}_2:\text{ErF}_3$  (0.1 mol.%)  $\tau=22.6 \mu\text{s}$

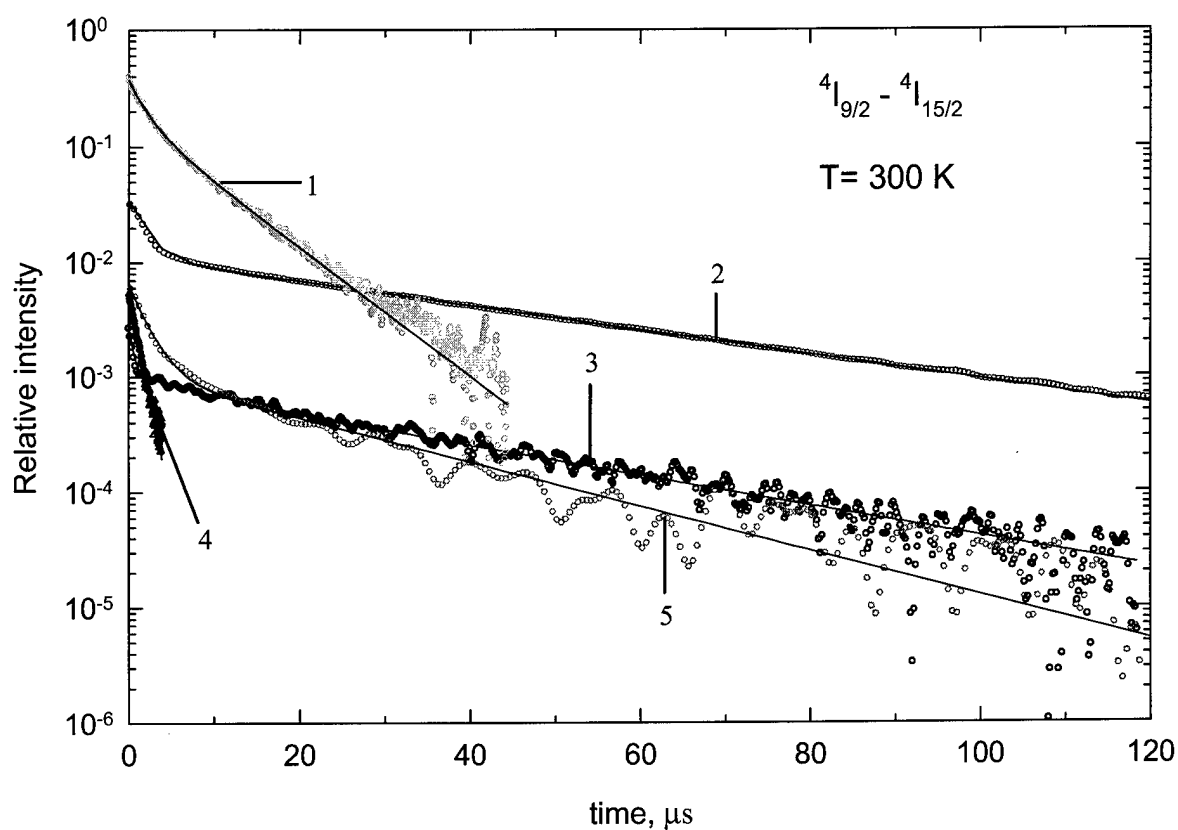


Fig. 1.3 Kinetics of fluorescence decay of the  $4I_{9/2}$  state of  $\text{Er}^{3+}$  in different fluoride crystals at 300 K.

Table 1.1. The lifetimes of the  $^4I_{9/2}$   $Er^{3+}$  state in different fluoride crystals at the final stage of kinetics decay at 300K.

Crystal type	CaF <sub>2</sub>	CdF <sub>2</sub>	SrF <sub>2</sub>	PbF <sub>2</sub>	BaF <sub>2</sub>
Atomic weights of cations	40.08	112.41	87.62	207.2	137.33
Crystal lattice parameter a, Å	5.45	5.40	5.78	5.94	6.19
Erbium concentration, Mol. %	0.03	1	0.1	2	0.3
Measured lifetime, μs	1.07	7.7	22.6	33.2	40

When concentration of erbium is increased the lifetime is decreased because of quenching energy transfer. The measured lifetime concentration dependencies for all studied crystals are presented in Tables 1.2- 1.6. When, for example, the CaF<sub>2</sub> erbium doped crystals were co-doped with Yb<sup>3+</sup> or Y<sup>3+</sup> ions the duration of the final stage of fluorescence kinetics decay is increased (Table 1.2 and Fig 1.4). The reason of this increase might be substitution of the second Er<sup>3+</sup> ion in the Er- Er pair center to Yb<sup>3+</sup> or Y<sup>3+</sup>. This avoids the energy transfer in the erbium pair and thus consequently increases the fluorescence kinetics decay and radiative quantum yield. This phenomenon have to be investigated more precisely at liquid helium temperatures at different erbium concentrations as was done, for example, in Ref. [6] for the CaF<sub>2</sub> and SrF<sub>2</sub> Nd<sup>3+</sup> doped crystals.

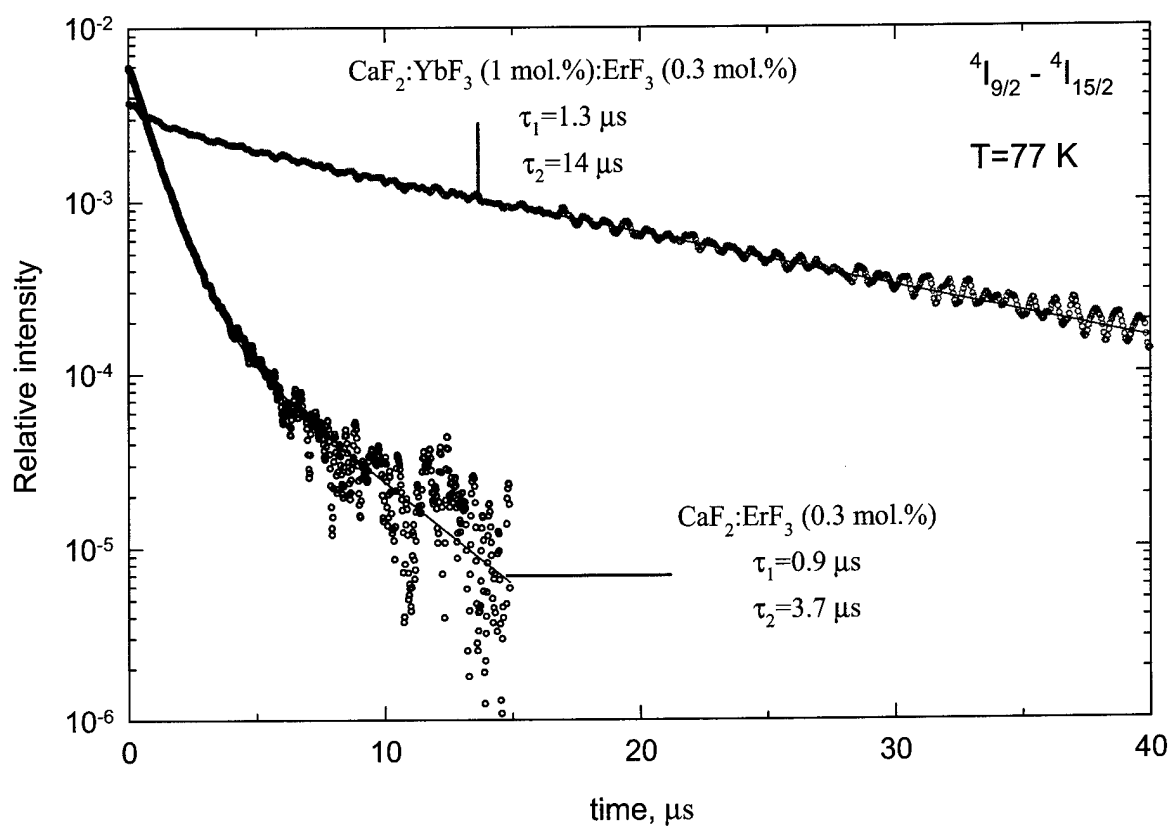


Fig. 1.4 Kinetics of fluorescence decay of the  $4I_{9/2}$  state of  $\text{Er}^{3+}$  in  $\text{CaF}_2:\text{ErF}_3$  (0.3 mol.%) and  $\text{CaF}_2:\text{YbF}_3$  (1 mol.): $\text{ErF}_3$  (0.3 mol.%) crystals at 77 K.

Table 1.2. **CaF<sub>2</sub>: ErF<sub>3</sub>**.

Erbium Concentration, mol. %	0.03	0.3		2
			1% YbF <sub>3</sub>	
The measured lifetime, $\mu$ s, T=300 K	1.1	1.1		2.2/ 8.7
T=77 K		0.9/ 3.7	1.3/14	

Table 1.3 and Fig. 1.5 presents the concentration dependence of fluorescence kinetics decay from the  $^4I_{9/2}$  state of erbium in the SrF<sub>2</sub> crystals at 77 and 300K. The significant changes of the shape and duration of kinetics decay deals with the changes of the partial concentrations of different optical centers at different total concentrations as well as with inter center energy transfer at moderate concentrations of erbium. For the concentrations higher than 1 mol.% disordering processes prevail which may increase concentration quenching because of energy migration to the acceptors and thus shorten the kinetics decay. Similar situation was found for concentration dependence in BaF<sub>2</sub>: ErF<sub>3</sub> (Table 1.4 and Fig. 1.6). All this facts require time and money consumptive spectroscopic investigations at liquid helium temperatures. See, for example, analysis for the CaF<sub>2</sub>:NdF<sub>3</sub> crystal in Ref [7].

Table 1.3. **SrF<sub>2</sub>: ErF<sub>3</sub>**.

Erbium concentration mol. %	0.1	0.5	0.8	1	5	10	20	30
The measured lifetime, $\mu$ s, T=300 K	2.5/ 22.6	2.75/ 20.5	2.45/ 21.4	20.2	12.1/ 26.9	7.8/ 18.3	7.7	5.0
T=77K	3.4/ 40.8	3.9/ 45.5	7.3/ 47.1					

- 1 -  $\text{SrF}_2:\text{ErF}_3$  (0.1 mol.%);  $\tau_1 = 2.5 \mu\text{s}$ ;  $\tau_2 = 22.6 \mu\text{s}$ ;  $T=300 \text{ K}$
- 2 -  $\text{SrF}_2:\text{ErF}_3$  (0.1 mol.%);  $\tau_1 = 3.4 \mu\text{s}$ ;  $\tau_2 = 40.8 \mu\text{s}$ ;  $T=77 \text{ K}$
- 3 -  $\text{SrF}_2:\text{ErF}_3$  (0.5 mol.%);  $\tau_1 = 2.75 \mu\text{s}$ ;  $\tau_2 = 20.5 \mu\text{s}$ ;  $T=300 \text{ K}$
- 4 -  $\text{SrF}_2:\text{ErF}_3$  (0.5 mol.%);  $\tau_1 = 3.9 \mu\text{s}$ ;  $\tau_2 = 45.5 \mu\text{s}$ ;  $T=77 \text{ K}$
- 5 -  $\text{SrF}_2:\text{ErF}_3$  (0.8 mol.%);  $\tau_1 = 2.45 \mu\text{s}$ ;  $\tau_2 = 21.4 \mu\text{s}$ ;  $T=300 \text{ K}$
- 6 -  $\text{SrF}_2:\text{ErF}_3$  (0.8 mol.%);  $\tau_1 = 7.3 \mu\text{s}$ ;  $\tau_2 = 47.1 \mu\text{s}$ ;  $T=77 \text{ K}$

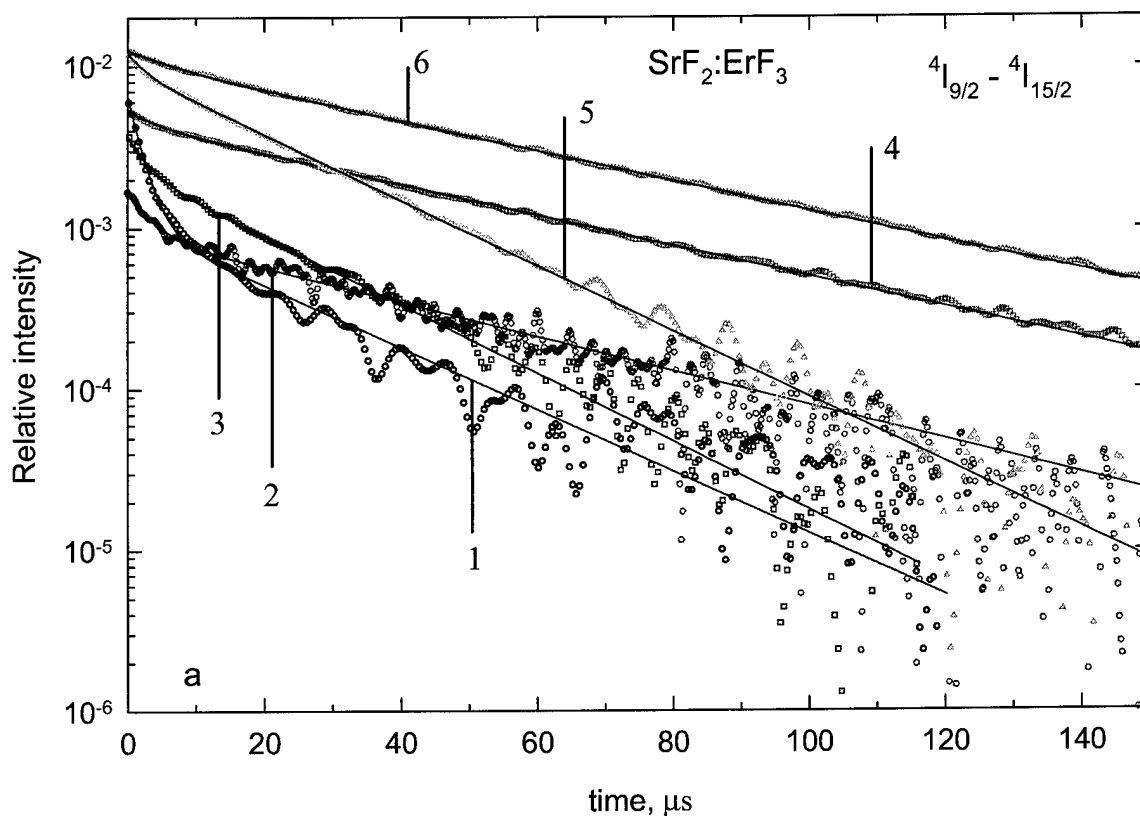


Fig. 1.5 (a) Kinetics of fluorescence decay of the  $4I_{9/2}$  state of  $\text{Er}^{3+}$  in  $\text{SrF}_2:\text{ErF}_3$  crystals with different concentrations of  $\text{Er}^{3+}$  ion at 77 and 300 K.

- 1 -  $\text{SrF}_2:\text{ErF}_3$  (1 mol.%);  $\tau_1 = 20.2 \mu\text{s}$   
 2 -  $\text{SrF}_2:\text{ErF}_3$  (5 mol.%);  $\tau_1 = 12.1 \mu\text{s}$ ;  $\tau_2 = 26.9 \mu\text{s}$   
 3 -  $\text{SrF}_2:\text{ErF}_3$  (10 mol.%);  $\tau_1 = 7.8 \mu\text{s}$ ;  $\tau_2 = 18.3 \mu\text{s}$   
 4 -  $\text{SrF}_2:\text{ErF}_3$  (20 mol.%);  $\tau_1 = 7.7 \mu\text{s}$   
 5 -  $\text{SrF}_2:\text{ErF}_3$  (30 mol.%);  $\tau_1 = 5.0 \mu\text{s}$

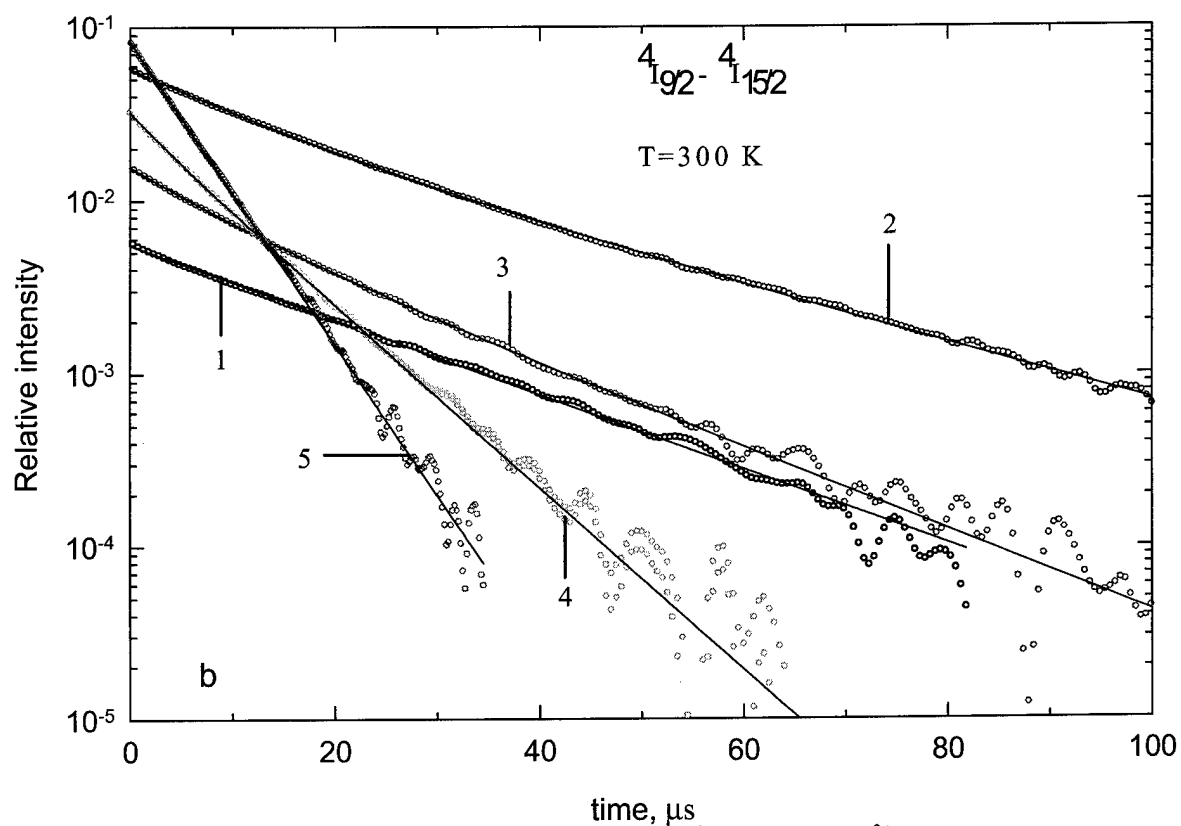


Fig. 1.5 (b) Kinetics of fluorescence decay of the  $4I_{9/2}$  state of  $\text{Er}^{3+}$  in  $\text{SrF}_2:\text{ErF}_3$  crystals with different concentrations of  $\text{Er}^{3+}$  ion at 300 K.



- 1 - BaF<sub>2</sub>:ErF<sub>3</sub> (0.1 mol.%);  $\tau_1 = 2.7 \mu\text{s}$ ;  $\tau_2 = 101 \mu\text{s}$ ; T=77 K  
 2 - BaF<sub>2</sub>:ErF<sub>3</sub> (0.3 mol.%);  $\tau_1 = 1.9 \mu\text{s}$ ;  $\tau_2 = 40.1 \mu\text{s}$ ; T=300 K  
 3 - BaF<sub>2</sub>:ErF<sub>3</sub> (0.3 mol.%);  $\tau_1 = 1.68 \mu\text{s}$ ;  $\tau_2 = 101 \mu\text{s}$ ; T=77 K  
 4 - BaF<sub>2</sub>:ErF<sub>3</sub> (1 mol.%);  $\tau_1 = 3.5 \mu\text{s}$ ;  $\tau_2 = 40.0 \mu\text{s}$ ; T=300 K

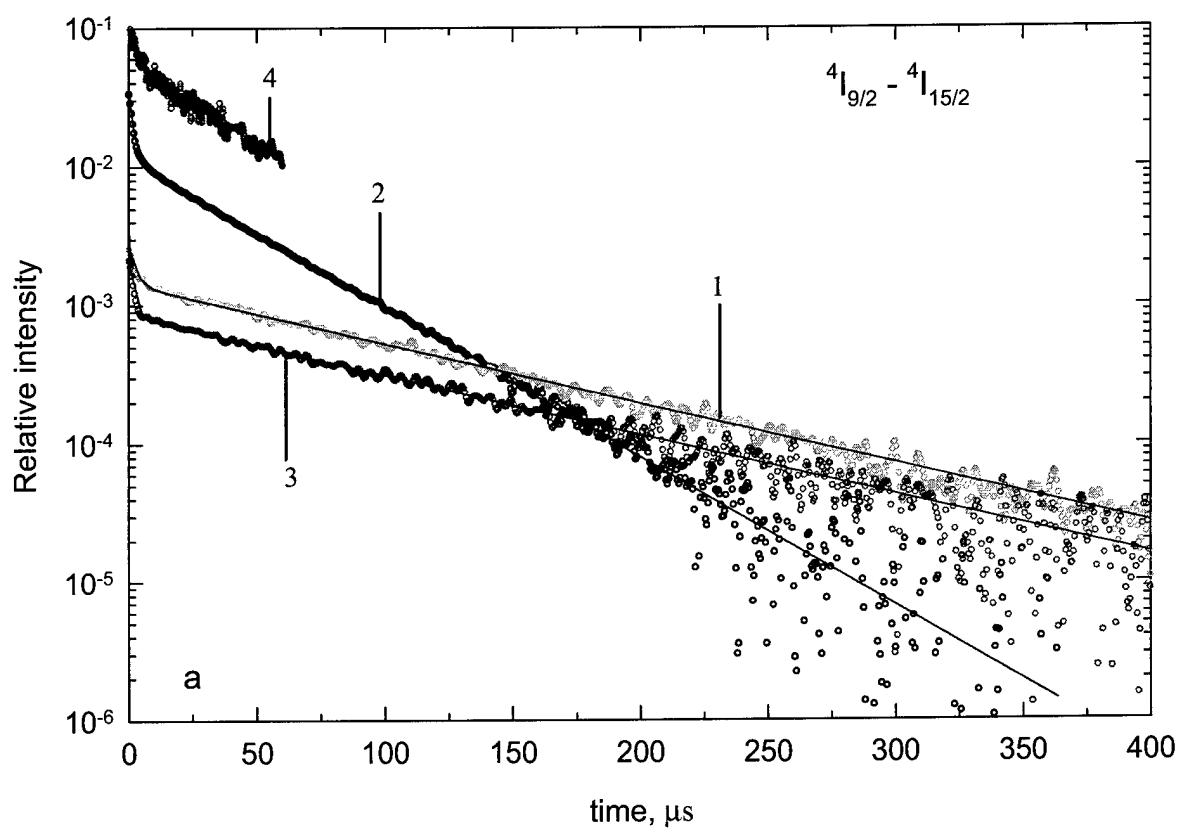


Fig. 1.6 (a) Kinetics of fluorescence decay of the  $^4I_{9/2}$  state of  $\text{Er}^{3+}$  in BaF<sub>2</sub>:ErF<sub>3</sub> crystals with different concentrations of  $\text{Er}^{3+}$  ion at 77 and 300 K.

- 1 -  $\text{BaF}_2:\text{ErF}_3$  (5 mol.%);  $\tau_1 = 25.2 \mu\text{s}$ ;  $\tau_2 = 55.1 \mu\text{s}$   
 2 -  $\text{BaF}_2:\text{ErF}_3$  (14 mol.%);  $\tau_1 = 14.1 \mu\text{s}$ ;  $\tau_2 = 27.7 \mu\text{s}$   
 3 -  $\text{BaF}_2:\text{ErF}_3$  (15 mol.%);  $\tau = 5.2 \mu\text{s}$ ;  $\tau_2 = 23.1 \mu\text{s}$

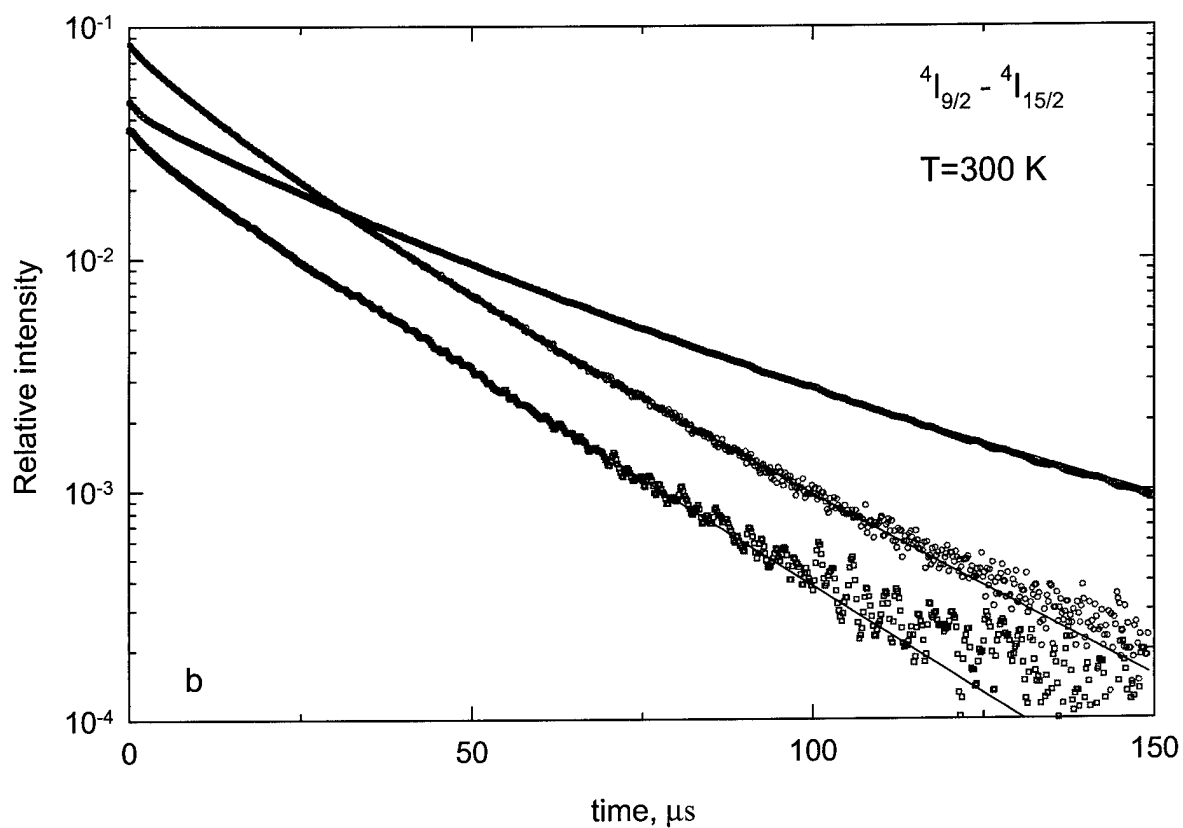


Fig. 1.6 (b) Kinetics of fluorescence decay of the  $4I_{9/2}$  state of  $\text{Er}^{3+}$  in  $\text{BaF}_2:\text{ErF}_3$  crystals with different concentrations of  $\text{Er}^{3+}$  ion at 300 K.

- 1 -  $\text{BaF}_2:\text{ErF}_3$  (16.7 mol.%);  $\tau_1 = 8.7 \mu\text{s}$ ;  $\tau_2 = 17.7 \mu\text{s}$   
 2 -  $\text{BaF}_2:\text{ErF}_3$  (23 mol.%);  $\tau_1 = 2.3 \mu\text{s}$ ;  $\tau_2 = 20.9 \mu\text{s}$   
 3 -  $\text{BaF}_2:\text{ErF}_3$  (41 mol.%);  $\tau = 8.7 \mu\text{s}$

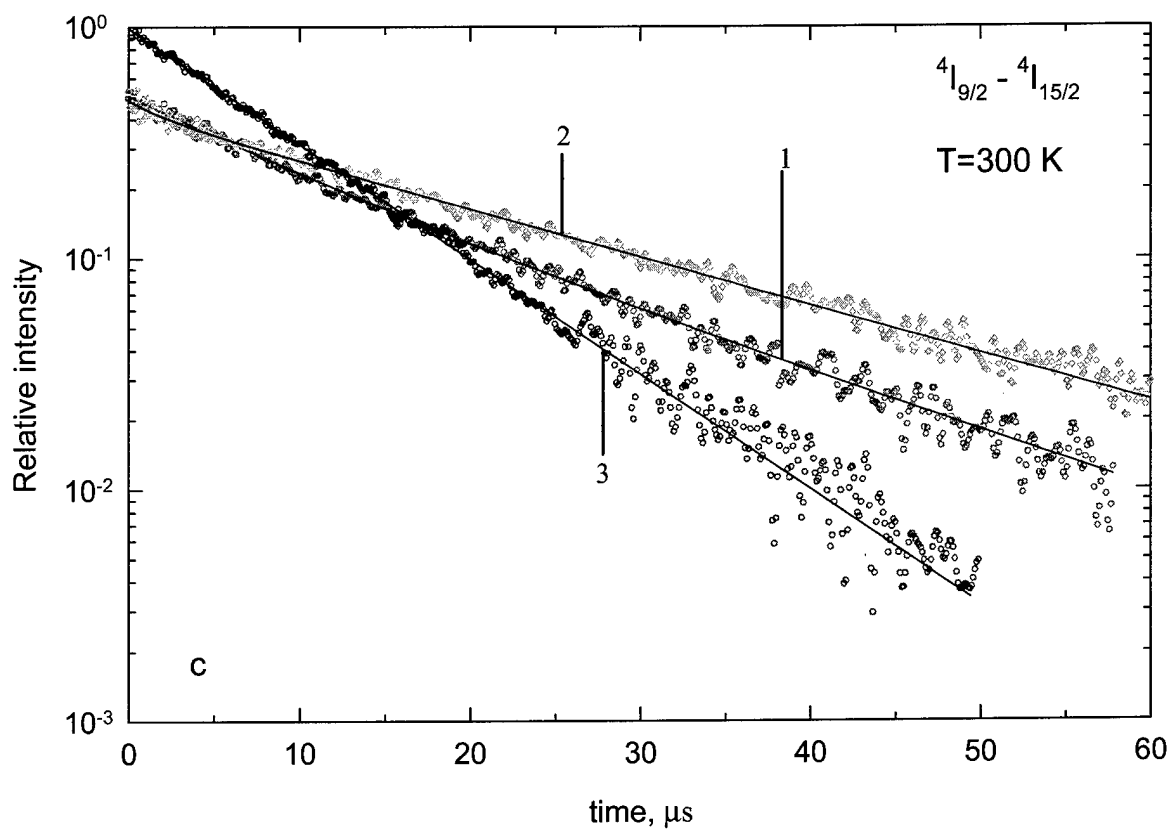


Fig. 1.6 (c) Kinetics of fluorescence decay of the  $4I_{9/2}$  state of  $\text{Er}^{3+}$  in  $\text{BaF}_2:\text{ErF}_3$  crystals with different concentrations of  $\text{Er}^{3+}$  ion at 300 K.

Table 1.4.  $\text{BaF}_2:\text{ErF}_3$ .

Erbium concentration Mol.%	0.1	0.3	1	5	14	15	16.7	23	41
The measured lifetime, $\mu\text{s}$ , T=300 K		1.9/ 40.1	3.5/ 40	25.2/ 55.1	14.1/ 27.7	5.2/ 23.1	8.7/ 17.7	2.3/ 20.9	8.7
T=77K	2.7/ 101	1.68/ 101							

Increasing the concentration of erbium in  $\text{CdF}_2$  at room temperature from 1 to 10 mol.% (Table 1.5 and Fig. 1.7a) slightly increases the measured lifetime. Codoping by  $\text{YF}_3$  (5 mol%) increases the duration of kinetics decay final stage like as in the case of  $\text{CaF}_2$  (Fig. 1.7b).

Concentration dependence of the lifetime for  $\text{PbF}_2:\text{ErF}_3$  crystals is presented in Table 1.6 and Fig. 1.8. The shortest decay was found for 10 mol.% of erbium concentration. These crystals require x-rays analysis for the determination of the crystal structure because  $\alpha$ - and  $\beta$ - modifications of the lattice (cubic and orthorhombic) are possible.

Also mixed crystals like  $(1-x) \text{CdF}_2: x \text{YF}_3: \text{ErF}_3$  (5 mol.%) and  $(1-x) \text{CdF}_2: x \text{YbF}_3: \text{ErF}_3$  (5 mol.%) were synthesized. The results of lifetime measurements of the  $^4\text{I}_{9/2}$  state are presented in Tables 1.7 (Fig. 1.9) and 1.8 (Fig. 1.10). As yttrium is lighter than cadmium we did not observe any significant increase of the lifetime in the  $(1-x) \text{CdF}_2: x \text{YF}_3: \text{ErF}_3$  (5 mol.%) crystals in comparison with  $\text{CdF}_2:\text{ErF}_3$  (5 mol.%). Changing of yttrium content does not change significantly the measured lifetimes though the longest lifetime was found for 20 mol.% of yttrium.

Though ytterbium is heavier than yttrium the lifetimes determined at the final stage of kinetics decay are almost the same at 10 mol.% of  $\text{YbF}_3$ . But in the latter case reliable identification of the final stage is rather doubtful because of the small signal-

to-noise ratio there. Changing of ytterbium from 10 to 20 mol.% increases the lifetime of the far stage of kinetics decay almost three times. But the latter measurement have to be checked.

Table 1.5. **CdF<sub>2</sub>: ErF<sub>3</sub>.**

Erbium concentration, mol. %	0.1	0.3	1	5	10
The measured lifetime, $\mu$ s T= 300K	YF <sub>3</sub> – 5 mol. %		2.1/8.0	3.1/9.1	4.8/10.7
T= 77K	2.8/19.7	1.6/14.6			

Table 1.6. **PbF<sub>2</sub>: ErF<sub>3</sub> at 300K.**

Erbium Concentration, mol. %	2	10	20
The measured lifetime, $\mu$ s	8.3/33.2	6.7/17.6	13.1/33.3

Table 1.7. **(1-x) CdF<sub>2</sub>: x YF<sub>3</sub>: ErF<sub>3</sub> (5 mol. %).**

Yttrium concentration, Mol. %	5	10	15	20	25
The measured lifetime, $\mu$ s	5.3/11.3	4.6/11.6	8.1/15.3	8.1/15.6	6.1/12.9

Table 1.8. **(1-x) CdF<sub>2</sub>: x YbF<sub>3</sub>: ErF<sub>3</sub> (5 mol. %) at 300K.**

Ytterbium concentration, mol. %	10	20
The measured lifetime, $\mu$ s	5.4/12.4	9.7/34.4

- 1 -  $\text{CdF}_2:\text{ErF}_3$  (1 mol.%);  $\tau_1 = 2.1 \mu\text{s}$ ;  $\tau_2 = 8.0 \mu\text{s}$   
 2 -  $\text{CdF}_2:\text{ErF}_3$  (5 mol.%);  $\tau_1 = 3.1 \mu\text{s}$ ;  $\tau_2 = 9.1 \mu\text{s}$   
 3 -  $\text{CdF}_2:\text{ErF}_3$  (10 mol.%);  $\tau_1 = 4.8 \mu\text{s}$ ;  $\tau_2 = 10.7 \mu\text{s}$

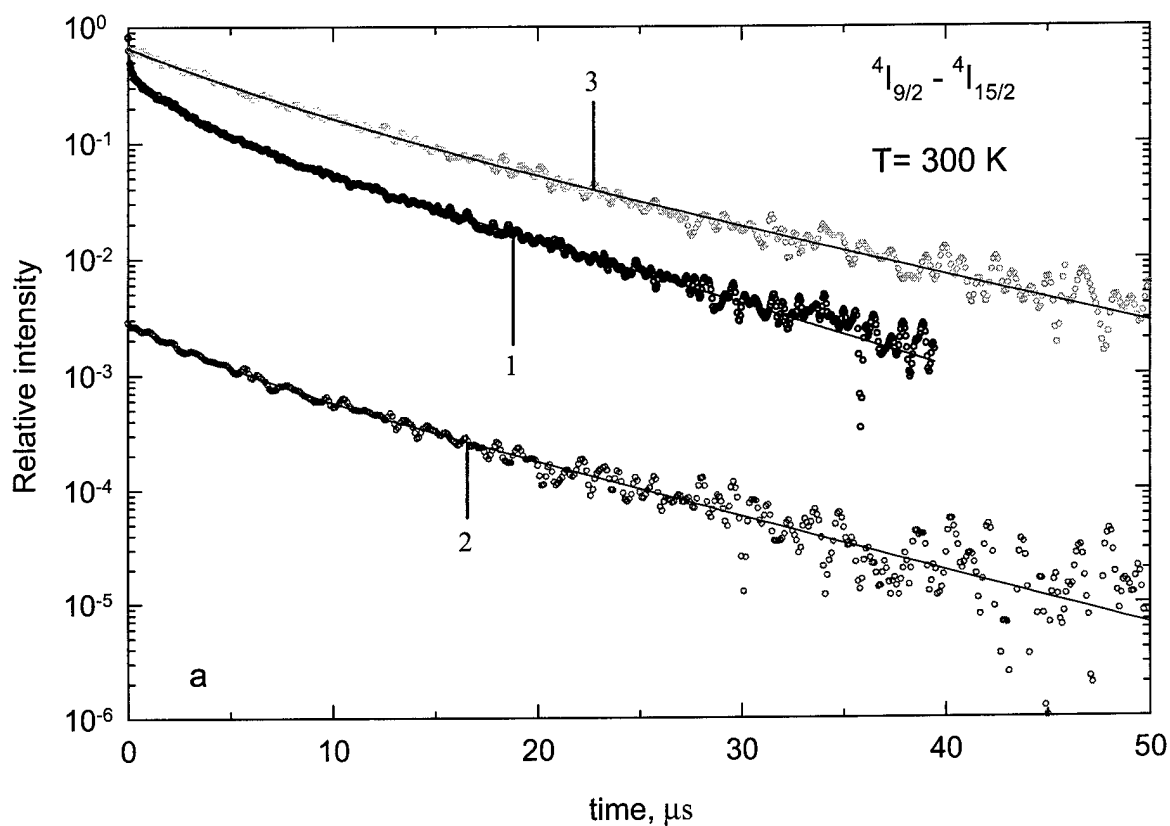


Fig. 1.7 (a) Kinetics of fluorescence decay of the  $^4I_{9/2}$  state of  $\text{Er}^{3+}$  in  $\text{CdF}_2:\text{ErF}_3$  crystals with different concentrations of  $\text{Er}^{3+}$  ion at 300 K.

1 -  $\text{CdF}_2:\text{YF}_3$  (5 mol.%): $\text{ErF}_3$  (0.1 mol.%);  $\tau_1 = 2.8 \mu\text{s}$ ;  $\tau_2 = 19.7 \mu\text{s}$

2 -  $\text{CdF}_2:\text{YF}_3$  (5 mol.%): $\text{ErF}_3$  (0.3 mol.%);  $\tau_1 = 1.6 \mu\text{s}$ ;  $\tau_2 = 14.6 \mu\text{s}$

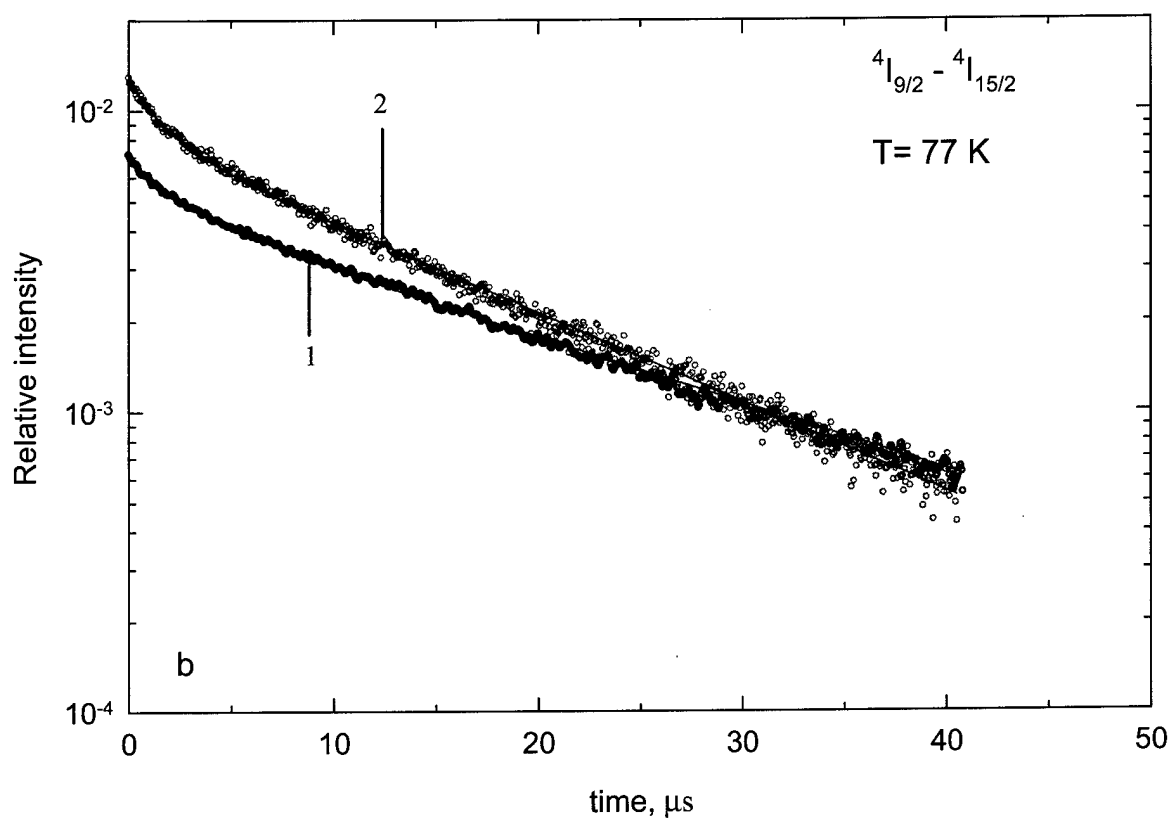


Fig. 1.7 (b) Kinetics of fluorescence decay of the  $4I_{9/2}$  state of  $\text{Er}^{3+}$  in  $\text{CdF}_2:\text{YF}_3$  (5 mol.%): $\text{ErF}_3$  crystals with different concentrations of  $\text{Er}^{3+}$  ion at 77 K.

- 1 -  $\text{PbF}_2:\text{ErF}_3$  (2 mol.%);  $\tau_1 = 8.3 \mu\text{s}$ ;  $\tau_2 = 33.2 \mu\text{s}$   
 2 -  $\text{PbF}_2:\text{ErF}_3$  (10 mol.%);  $\tau_1 = 6.7 \mu\text{s}$ ;  $\tau_2 = 17.6 \mu\text{s}$   
 3 -  $\text{PbF}_2:\text{ErF}_3$  (20 mol.%);  $\tau_1 = 13.1 \mu\text{s}$ ;  $\tau_2 = 33.3 \mu\text{s}$

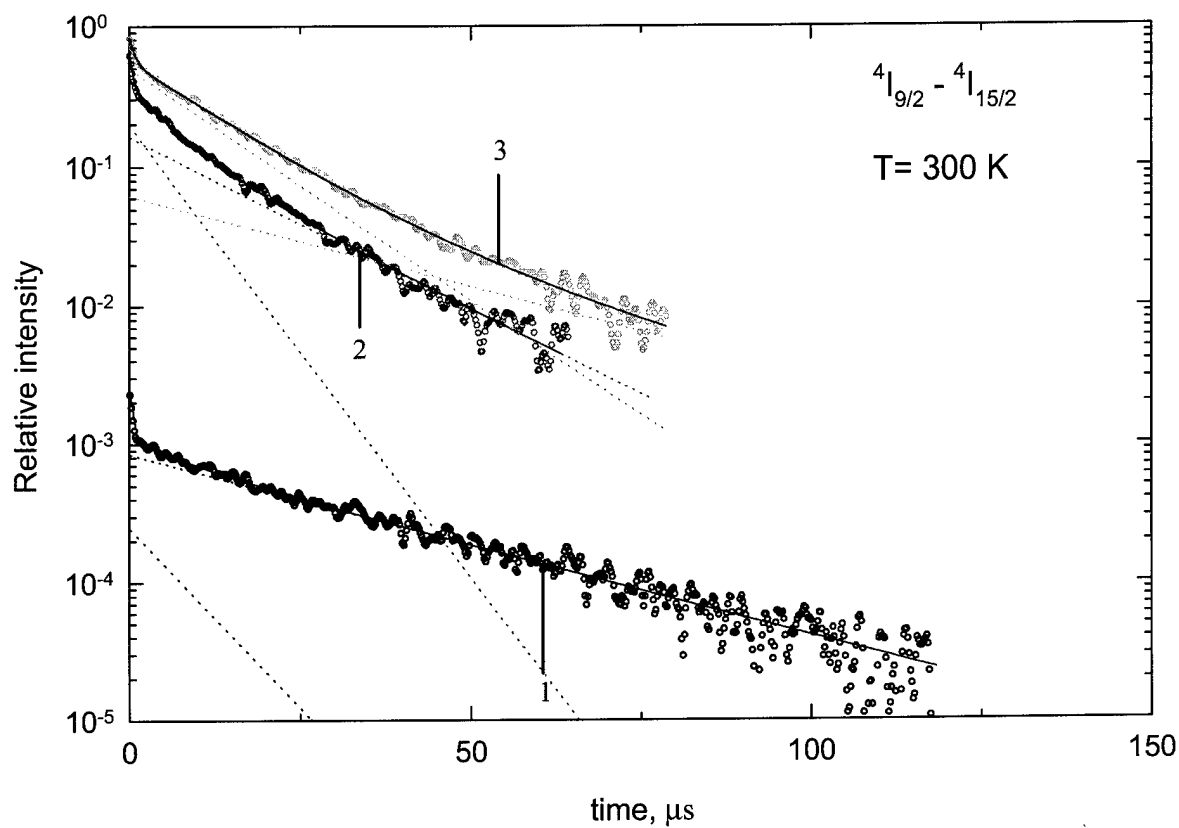


Fig. 1.8 Kinetics of fluorescence decay of the  $4I_{9/2}$  state of  $\text{Er}^{3+}$  in  $\text{PbF}_2:\text{ErF}_3$  crystals with different concentrations of  $\text{Er}^{3+}$  ion at 300 K.



- 1 -  $\text{CdF}_2:\text{YF}_3$  (5 mol.%):  $\text{ErF}_3$  (5 mol.%);  $\tau_1 = 5.3 \mu\text{s}$ ;  $\tau_2 = 11.3 \mu\text{s}$   
 2 -  $\text{CdF}_2:\text{YF}_3$  (10 mol.%):  $\text{ErF}_3$  (5 mol.%);  $\tau_1 = 4.6 \mu\text{s}$ ;  $\tau_2 = 11.6 \mu\text{s}$   
 3 -  $\text{CdF}_2:\text{YF}_3$  (15 mol.%):  $\text{ErF}_3$  (5 mol.%);  $\tau_1 = 8.1 \mu\text{s}$ ;  $\tau_2 = 15.3 \mu\text{s}$   
 4 -  $\text{CdF}_2:\text{YF}_3$  (20 mol.%):  $\text{ErF}_3$  (5 mol.%);  $\tau_1 = 8.1 \mu\text{s}$ ;  $\tau_2 = 15.3 \mu\text{s}$   
 5 -  $\text{CdF}_2:\text{YF}_3$  (25 mol.%):  $\text{ErF}_3$  (5 mol.%);  $\tau_1 = 6.1 \mu\text{s}$ ;  $\tau_2 = 12.9 \mu\text{s}$

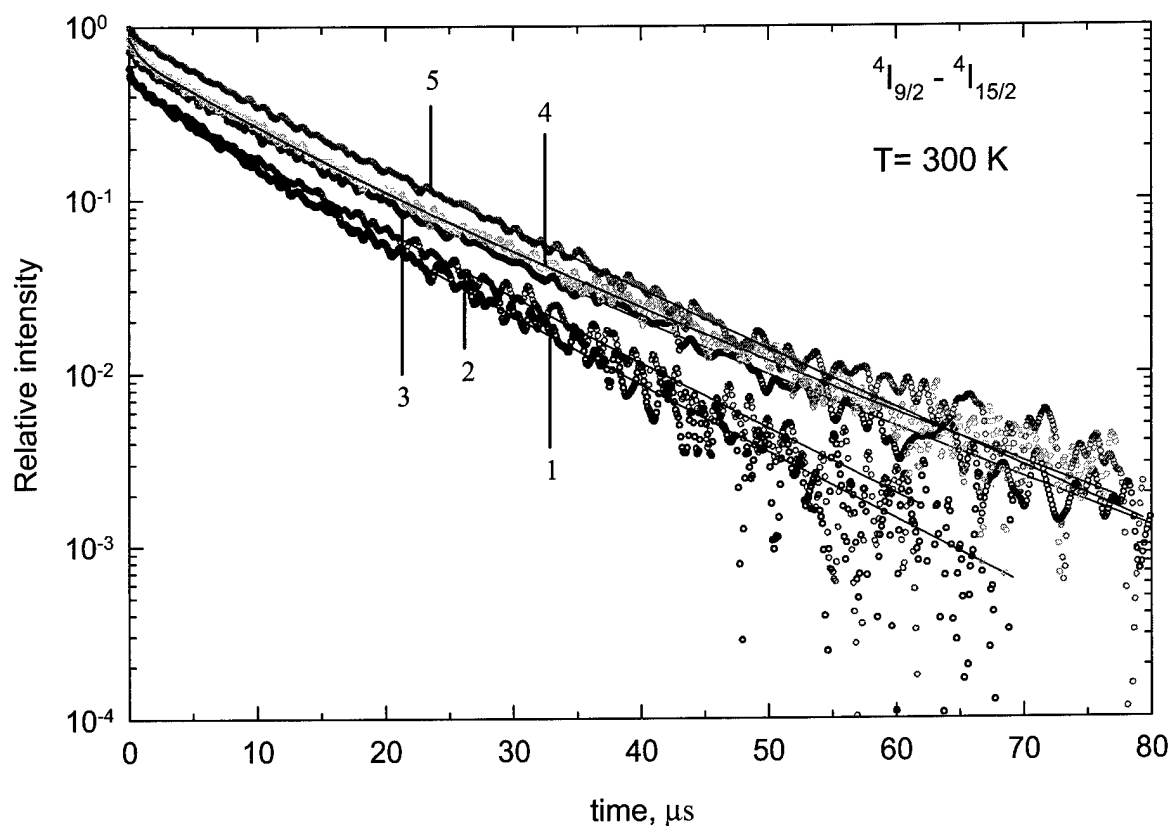


Fig. 1.9 Kinetics of fluorescence decay of the  $4I_{9/2}$  state of  $\text{Er}^{3+}$  in  $\text{CdF}_2:\text{YF}_3:\text{ErF}_3$  (5 mol.%) crystals with different concentrations of  $\text{Y}^{3+}$  ion at 300 K.

1 -  $\text{CdF}_2:\text{YbF}_3$  (10 mol.%):  $\text{ErF}_3$  (5 mol.%);  $\tau_1 = 5.4 \mu\text{s}$ ;  $\tau_2 = 12.4 \mu\text{s}$

2 -  $\text{CdF}_2:\text{YbF}_3$  (20 mol.%):  $\text{ErF}_3$  (5 mol.%);  $\tau_1 = 9.7 \mu\text{s}$ ;  $\tau_2 = 34.4 \mu\text{s}$

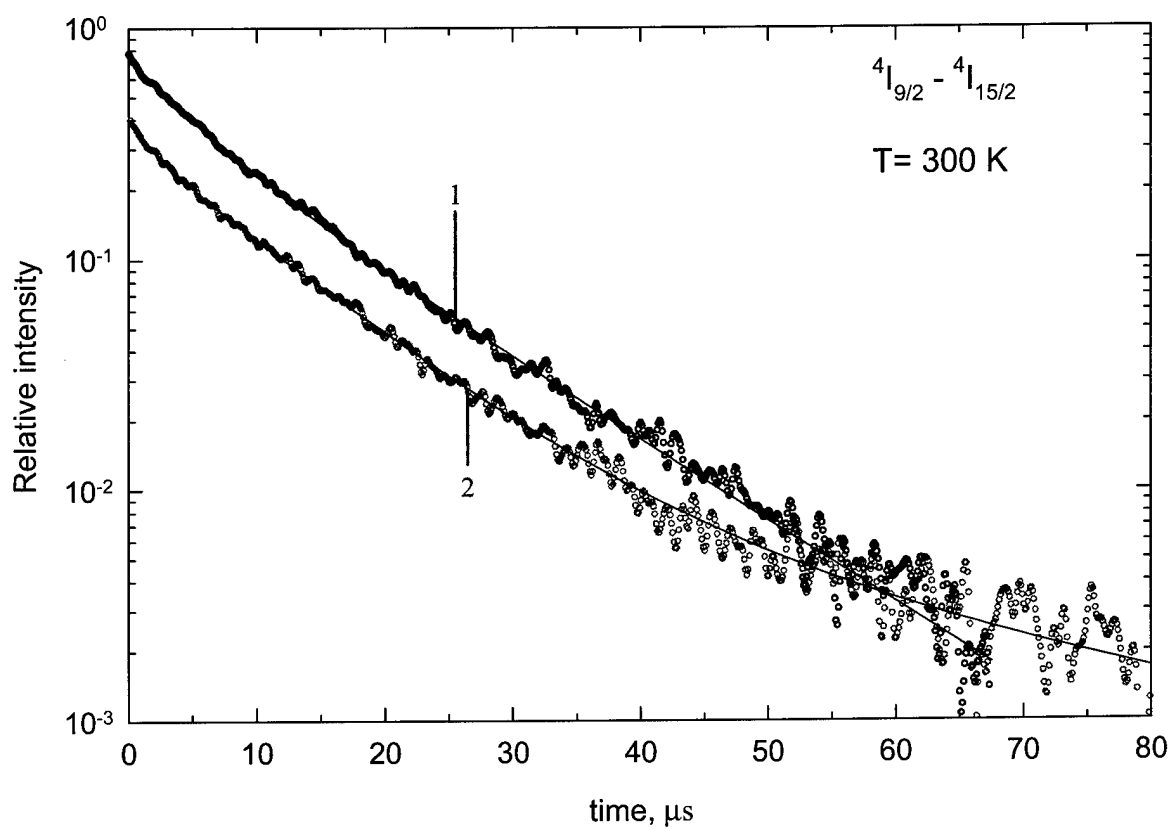


Fig. 1.10 Kinetics of fluorescence decay of the  $4I_{9/2}$  state of  $\text{Er}^{3+}$  in  $\text{CdF}_2:\text{YbF}_3:\text{ErF}_3$  (5 mol.%) crystals with different concentrations of  $\text{Yb}^{3+}$  ion at 300 K.

Similar measurements were done in the  $\text{LaF}_3$  erbium doped crystals. The results are presented in Table 1.9 and Fig. 1.11. All measured fluorescence kinetics decay curves were exponential, because  $\text{LaF}_3$  as opposed to fluorites is the single –site crystal at low concentrations. The lifetime ( $\tau = 31.6 \mu\text{s}$ ) at 1 mol.% concentration of erbium is less than in  $\text{BaF}_2$  ( $\tau = 40.0 \mu\text{s}$ ) though the atom mass for La is larger than for Ba. The reason is the smaller distance  $R_0$  between the  $\text{La}^{3+}$  ion and the nearest fluorine ions in  $\text{LaF}_3$  ( $R_0 = 2.42 \text{ \AA}$ ) in comparison with  $\text{BaF}_2$  ( $R_0 = 2.68 \text{ \AA}$ ). In  $\text{LaF}_3$  the measured fluorescence lifetime is almost constant at up to 6.17% of erbium concentration and decreases significantly (6 times) at 11.3% due to concentration quenching.

Table 1.9.  $\text{LaF}_3$ :  $\text{ErF}_3$  at 300K.

Erbium concentration, mol. %	1.23	2.97	6.17	11.3
The measured lifetime, $\mu\text{s}$	31.6	34.0	29.9	5.8

Preliminary analysis of the main spectroscopic parameters characterizing the efficiency of laser generation was provided. In doing so the radiative lifetimes, quantum efficiencies, branching ratios and total emission cross- sections from the main  $^4\text{I}_{9/2}$  laser level to the low  $^4\text{I}_{11/2}$  laser level and to the  $^4\text{I}_{13/2}$  intermediate and the  $^4\text{I}_{15/2}$  ground levels were calculated in the  $\text{LaF}_3$ :  $\text{Er}^{3+}$  crystal. The equations used for calculations are presented in the section 1.3. The  $\Omega_k$  –parameters were taken from Ref. [3] ( $\Omega_2 = 1.07 \cdot 10^{-20}$ ;  $\Omega_4 = 0.28 \cdot 10^{-20}$ ;  $\Omega_6 = 0.63 \cdot 10^{-20} \text{ cm}^2$ ). All these parameters along with  $\sigma_{\text{em}}$ ,  $\tau_{\text{meas}}$ , product which characterizing laser threshold are presented in Table 1.10. It is seen that the  $\sigma_{\text{em}}$ ,  $\tau_{\text{meas}}$ , product for  $4.3 \mu\text{m}$  is comparable with the known laser transitions. The lifetime of the  $^4\text{I}_{9/2}$  state ( $\tau_{\text{meas}} = 133 \mu\text{s}$ ) was measured at 4.2K in Ref. [8]. Because of the temperature stimulation of multiphonon relaxation

the measured lifetime of the  $^4I_{9/2}$  state decreases from the  $\tau=150 \mu\text{s}$  at  $T=77 \text{ K}$  [9] to  $\tau=30 \mu\text{s}$  at room temperature. This lifetime depends also on the purity of raw materials. In the case of unintentional doping with  $\text{Ce}^{3+}$  ions and/or other rare- earth ions the energy transfer quenched processes is possible which decrease the upper laser level lifetime. Therefore, the raw materials for crystal growth of high purity are necessary to use.

Table 1.10 The wavelengths, radiative rates, measured lifetime, quantum efficiencies, branching ratios and integrated emission cross- sections from Judd- Ofelt analysis in the  $\text{LaF}_3: \text{Er}^{3+}$  crystal.

Transition	$\lambda_{\mu\text{m}}$	$A_{\text{rad}}, \text{sec}^{-1}$		$\tau_{\text{meas.}}, \mu\text{s}$ ( $T=300\text{K}$ )	$\eta = \tau_{\text{meas.}} \times \Sigma A_{ij}$	$\beta$	$10^{19} \times \sigma_{\text{em.}}, \text{cm}$	$\sigma_{\text{em.}} \tau_{\text{meas.}} \times 10^{20}, \text{cm ms}$
$^4I_{9/2} \rightarrow ^4I_{11/2}$	4.95	Ed	0.36	~30	$1.53 \times 10^{-3}$	0.029	1.5	0.45
		Md	1.11					
		$\Sigma$	1.47					
$^4I_{9/2} \rightarrow ^4I_{13/2}$	1.72	Ed	24.7			0.485	3.7	1.1
		Md	0					
		$\Sigma$	24.7					
$^4I_{9/2} \rightarrow ^4I_{15/2}$	0.81	Ed	24.8			0.486	0.84	0.25
		Md	0					
		$\Sigma$	24.8					

1 -  $\text{LaF}_3:\text{ErF}_3$  (2.97 mol.%);  $\tau = 34.0 \mu\text{s}$

2 -  $\text{LaF}_3:\text{ErF}_3$  (6.17 mol.%);  $\tau_1 = 29.9 \mu\text{s}$

3 -  $\text{LaF}_3:\text{ErF}_3$  (11.3 mol.%);  $\tau_1 = 5.8 \mu\text{s}$

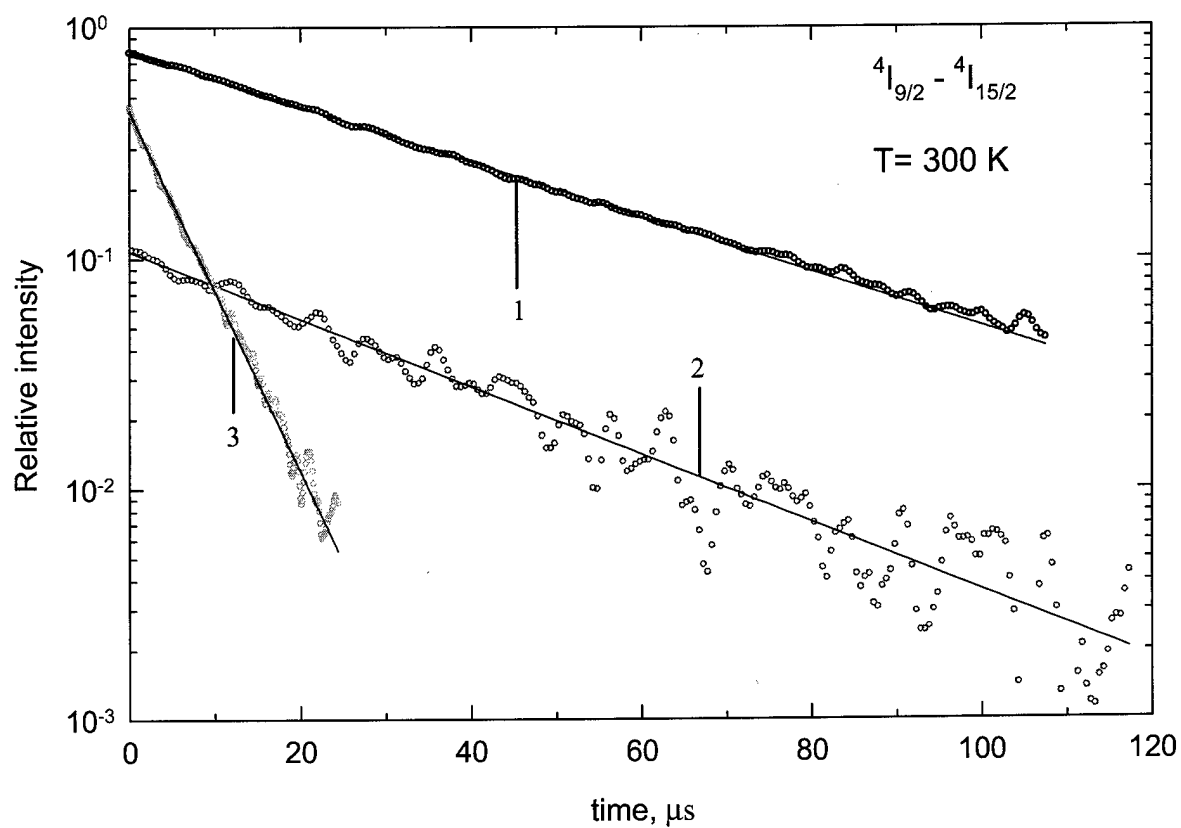


Fig. 1.11 Kinetics of fluorescence decay of the  $4I_{9/2}$  state of  $\text{Er}^{3+}$  in  $\text{LaF}_3:\text{ErF}_3$  crystals with different concentrations of  $\text{Er}^{3+}$  ion at 300 K.

### 1.3. Theoretical background.

Absorption and radiative characteristics of RE ions can be expressed in term of line strength.

In the theory, the line strength  $S_{ed}(J, J')$  for electric-dipole transition  $[LSJ] \rightarrow [L'S'J']$  is defined as:

$$S_{ed}(J, J') = (1/e^2) \sum_{\alpha} \sum_{\beta} |(LSJ\alpha | P | L'S'J'\beta)|^2 \quad (1.3)$$

Here  $e$  is electronic charge,

$$\mathbf{P} = e \sum_i \mathbf{r}_i \quad (1.4)$$

is electric-dipole moment of optical electrons (4f electrons for RE ions),  $\mathbf{r}_i$  is coordinate of  $i$ -th optical electron,  $|LSJ\alpha\rangle$  is wave function of  $\alpha$ -th crystal field state of  $[LSJ]$  multiplet.

The line strength  $S_{md}(J, J')$  for magnetic-dipole transition  $[LSJ] \rightarrow [L'S'J']$  is defined as

$$S_{md}(J, J') = (\beta/e)^2 (LSJ || \mathbf{L} + 2\mathbf{S} || L'S'J')^2, \quad (1.5)$$

where  $\beta = e\hbar/2mc$  is Bohr magneton, and  $(LSJ || \mathbf{L} + 2\mathbf{S} || L'S'J')$  is the reduced matrix element for vector  $\mathbf{L} + 2\mathbf{S}$  ( $\mathbf{L}$  is orbital angular momentum and  $\mathbf{S}$  is spin momentum).

The probability of spontaneous electric-dipole emission from the excited  $[LSJ]$  multiplet to the lower  $[L'S'J']$  multiplet is given by expression presented in Ref. [10]:

$$A_{ed}(J \rightarrow J') = \left[ 32\pi^3 e^2 E^3 n / 3\hbar (2J+1) \right] S_{ed}(J, J') . \quad (1.6)$$

Here,  $E=1/\lambda$ ,  $\lambda$  is the mean wave length for [LSJ]  $\rightarrow$  [L'S'J'] interstate transition ,  $n$  is the refractive index, and factor

$$\chi = [(n^2 + 2)/3]^2 \quad (1.7)$$

is the Lorentz field correction. In Eq. (1.6) factor  $1/(2J+1)$  accounts for the statistical weight of the initial level.

The probability of spontaneous magnetic-dipole emission from the excited [LSJ] multiplet to the lower [L'S'J'] multiplet is given by expression presented in Ref. [11]:

$$A_{md}(J \rightarrow J') = \left[ 32\pi^3 e^2 E^3 n^3 / 3\hbar(2J+1) \right] S_{md}(J, J') \quad (1.8)$$

The total probability  $A(J \rightarrow J')$  of spontaneous dipole emission is

$$A(J \rightarrow J') = A_{ed}(J \rightarrow J') + A_{md}(J \rightarrow J') \quad (1.9)$$

The radiative lifetime of a [LSJ] state is

$$\tau_J = 1 / \sum_{J'} A(J \rightarrow J') \quad (1.10)$$

The branching ratio for a [LSJ]  $\rightarrow$  [L'S'J'] transition is

$$\beta(J, J') = A(J \rightarrow J') / \sum_{J'} A(J \rightarrow J') = A(J \rightarrow J') \tau_J \quad (1.11)$$

Experimentally, the total absorption cross-section ( $\sigma_{abs}$ ) is found as

$$\sigma_{abs} = \int \sigma(E) dE = \int \ln[I_{inc}(E)/I_{tran}(E)] dE / Nl \quad (1.12)$$

where  $\sigma(E)$  is the absorption cross-section for specific wavelength,  $I_{inc}$  and  $I_{tran}$  are intensities of incident and transmitted light, respectively.  $N$  is number of RE ions in  $\text{cm}^3$ , and  $l$  is the sample thickness.

The total absorption cross-section of a  $[LSJ] \rightarrow [L'S'J']$  interstate transition is related with  $A(J' \rightarrow J)$  as [10]

$$\sigma_{abs}(J \rightarrow J') = A(J' \rightarrow J)(2J'+1) / [8\pi c n^2 E^2 (2J+1)] \quad (1.13)$$

Taking into account Eqs. (1.6)-(1.9), we obtain

$$\sigma_{abs}(J \rightarrow J') = 4\pi^2 e^2 E \left[ \chi \left( \frac{1}{n} \right) S_{ed} + n S_{md} \right] / [3\hbar c (2J+1)] \quad (1.14)$$

The total stimulated emission cross-section of a  $[LSJ] \rightarrow [L'S'J']$  interstate transition is related to  $A(J, J')$  as

$$\sigma_{em}(J \rightarrow J') = A(J \rightarrow J') / 8\pi c n^2 E^2 \quad (1.15)$$

Having the line strength  $S(J, J')$  one can determine the above enumerated absorption and radiative characteristics of RE ions.

#### 1.4. Absorption properties of erbium doped fluoride crystals at the $^4I_{15/2} \rightarrow ^4I_{13/2}$ transition at T=300 K.

This section was mainly dedicated to the optical properties of Er-doped fluoride crystals that are prospective for producing laser elements to be pumped by 1.54  $\mu\text{m}$  of Er glass laser.

Concentration series of erbium doped crystals have been synthesized in such systems as  $\text{BaF}_2\text{-ErF}_3$ ;  $\text{PbF}_2\text{-ErF}_3$ ;  $\text{SrF}_2\text{-ErF}_3$ . A special attention has been paid to the  $\text{CdF}_2\text{-}$



YF<sub>3</sub>-ErF<sub>3</sub> based system for which we have managed to synthesize high optical quality crystals with the concentration of both YF<sub>3</sub> and ErF<sub>3</sub> varied in a rather wide range (up to 30 mol. %). From the obtained crystals the cut and polished plates of 6 mm in diameter and of 0.8 to 5 mm thickness have been prepared. Er<sup>3+</sup> absorption spectrum at the  $^4I_{15/2} \rightarrow ^4I_{13/2}$  transition have been measured and its maximum as well as its absorption coefficient at 1.54  $\mu\text{m}$  (Er glass pumping laser wavelength) have been determined. In the CdF<sub>2</sub>- YF<sub>3</sub>- ErF<sub>3</sub> based system the absorption coefficient and the form factor did not actually show the dependence on Y concentration and the correspondent absorption coefficient has been linearly increased with Er concentration. The example of absorption coefficient trend versus wavelength for a certain compositions of Cd<sub>0.85</sub>Y<sub>0.1</sub>Er<sub>0.05</sub>F<sub>2.15</sub> is shown in Fig.1.12. From the figure it is seen that the position of the maximum is shifted towards the short-wavelengths relatively to 1.54  $\mu\text{m}$  pumping wavelength. Anyway, even for rather low Er concentration (5 mol. %) the absorption coefficient at 1.54  $\mu\text{m}$  is rather high (4 cm<sup>-1</sup>).

The next figure (Fig. 1.13) shows absorption spectra for the crystal samples based on BaF<sub>2</sub>- ErF<sub>3</sub> system. The optical quality of obtained crystals was not good enough. A light scattering in the object has been observed. In contrast with Fig.1.12 there is no significant central peak in the absorption band. The absorption band has complex structure and when Er concentration is raised a redistribution of the intensity of three peaks takes place in favour of one with the shortest wavelength. In this case the absorption coefficient at 1.54  $\mu\text{m}$  is approximately 30% lower than that for CdF<sub>2</sub>- YF<sub>3</sub>-ErF<sub>3</sub> crystals with the same Er concentration. The similar spectra study has been done for the crystal samples based on PbF<sub>2</sub>-ErF<sub>3</sub>; and SrF<sub>2</sub>-ErF<sub>3</sub> systems. The examples of absorption spectra are shown in Fig.1.14.

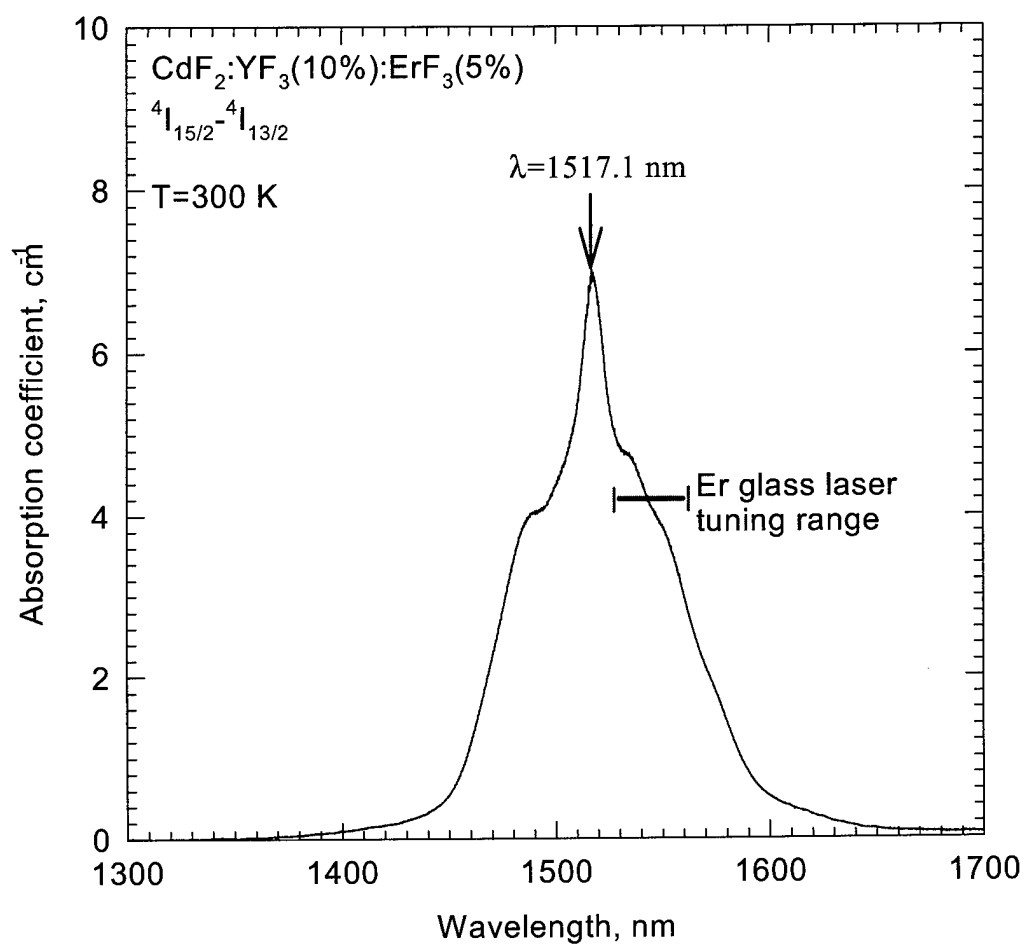


Fig. 1.12 Absorption spectrum

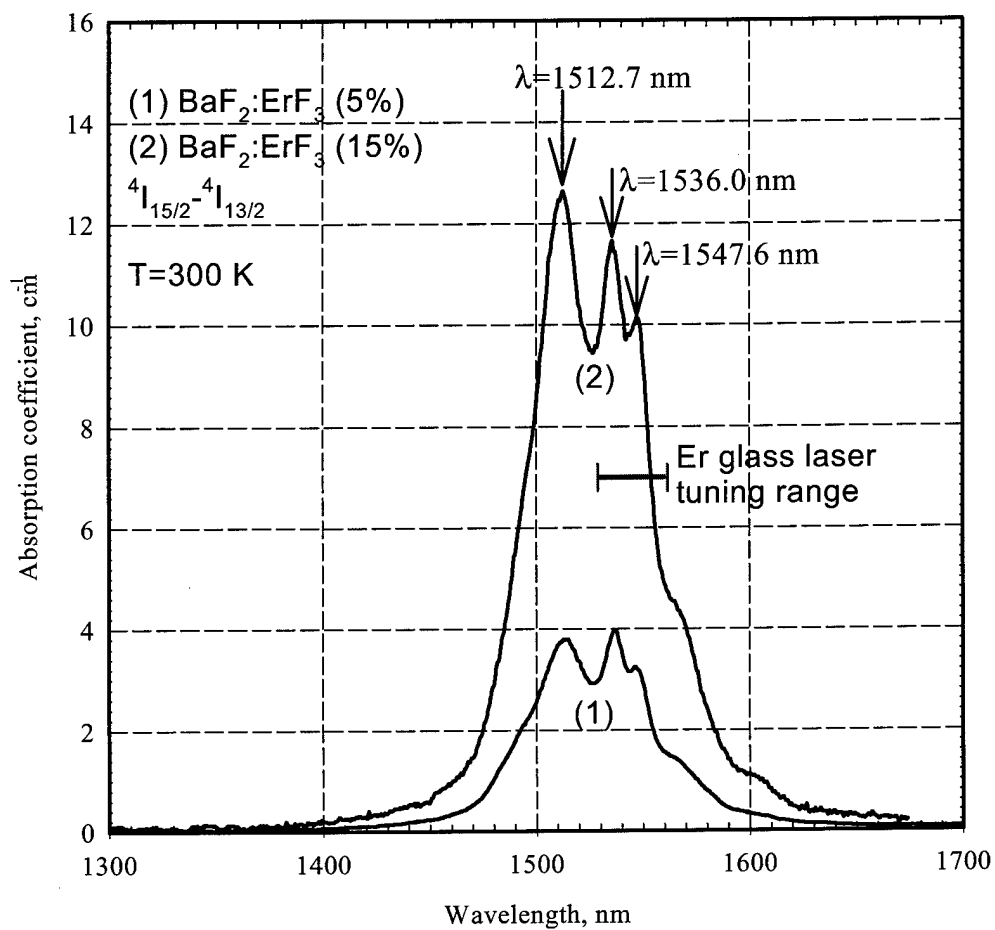


Fig. 1.13 Absorption spectra

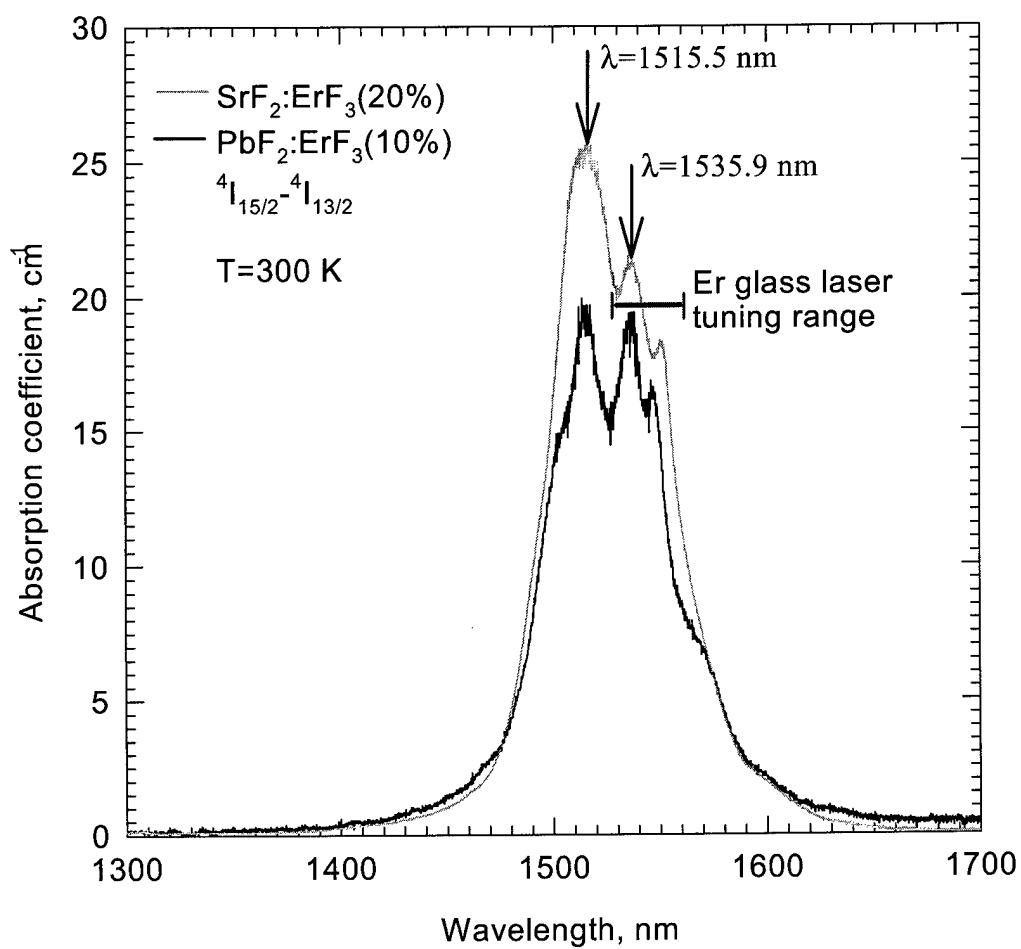


Fig. 1.14 Absorption spectra

Table 1.11 lists the absorption coefficient values at 1.54  $\mu\text{m}$  in different crystals with  $\text{Er}^{3+}$  ions concentration of 5 mol. %.

Table 1.11 Absorption coefficients of different fluoride crystals doped with 5 mol. %  $\text{Er}^{3+}$  at 1.54  $\mu\text{m}$ .

Crystal	$K_{\lambda=1.54\mu\text{m}}, \text{cm}^{-1}$
$\text{CdF}_2\text{-YF}_3\text{-ErF}_3$	4.5
$\text{BaF}_2\text{-ErF}_3$	3.8
$\text{PbF}_2\text{-ErF}_3$	9.6
$\text{SrF}_2\text{-ErF}_3$	5.4

Above mentioned results bring to a conclusion that all studied crystals with Er concentration less than 5 mol.% allow to absorb effectively the pumping energy at 1.54  $\mu\text{m}$  even for the thickness being less than 5 mm. This result is especially important for the systems with LD pumping.

For calculation of absorption cross-section the following equation can be used:

$$\sigma_{\text{abs}}(\nu) = \ln(I_0 / I(\nu)) / (N d), \quad (1.16),$$

where  $I_0$  is the transmission of the crystal without dopant,  $I(\nu)$  is the intensity transmitted in the doped crystal at the wavenumber  $\nu$  ( $\nu$  in  $\text{cm}^{-1}$ ),  $N$  is erbium concentration, and  $d$  is the thickness of the sample. The results for the  $\text{LaF}_3\text{:Er}^{3+}$  (2.97 mol.%) crystal are presented in Fig. 1.15. The concentration of erbium was determined by the electron microprobe analysis at the Camebax system. The experimental integral absorption cross-section for  $\text{LaF}_3\text{:Er}^{3+}$  ( $3.5 \times 10^{-19} \text{ cm}$ ) was found to be 3.5 times less than the theoretical one ( $12.4 \times 10^{-19} \text{ cm}$ ). This result requires remeasurements of the absorption spectrum of  $\text{LaF}_3\text{:Er}^{3+}$  and correct calculations of the  $\Omega_k$  – intensity parameters using only low-lying electronic states of erbium ion.

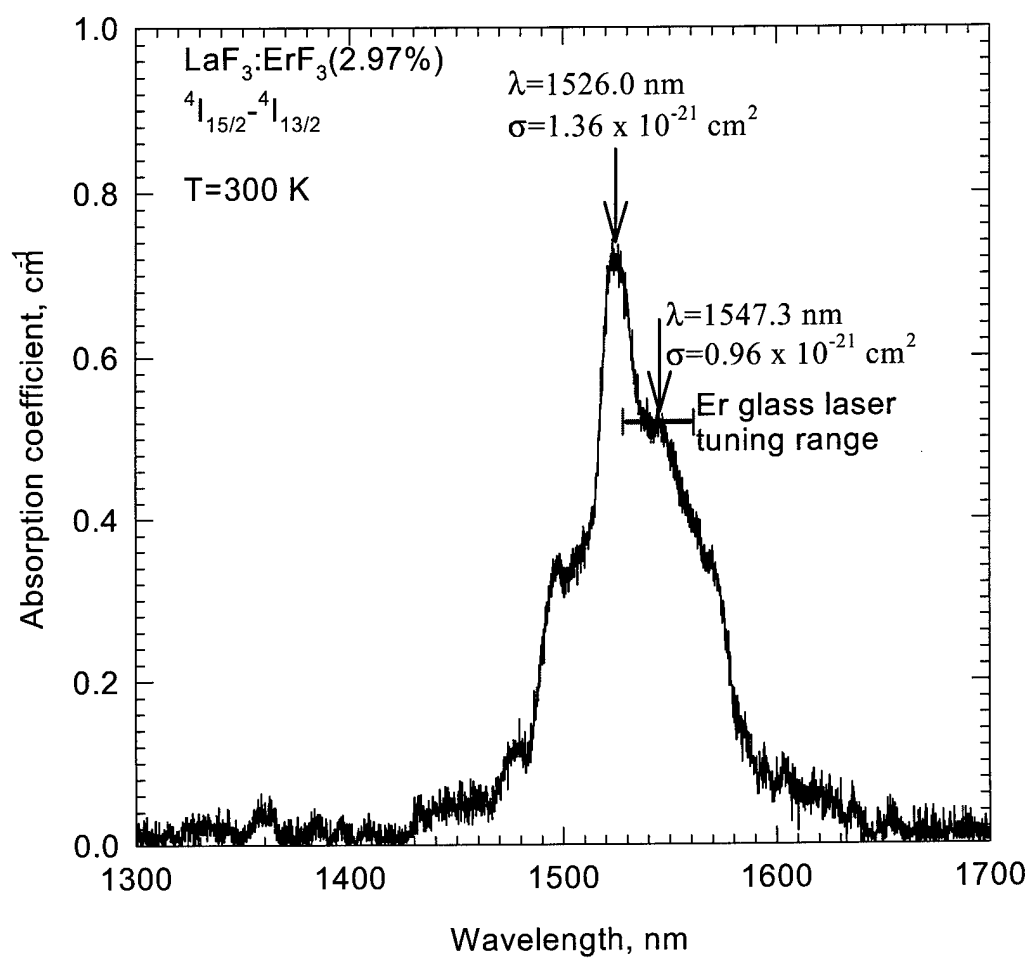


Fig. 1.15 Absorption spectrum

## References

1. B.R. Judd, Phys. Rev. **127**, 750 (1962)
2. G.S. Ofelt, J. Chem. Phys. **37**, 511 (1962)
3. W.T. Carnall, H. Crosswhite, H.M. Crosswhite, Aragon National Laboratory, Internal Report (1977) Baltimore, Maryland
4. M.J.Weber, Phys. Rev., **157**, 262 (1967)
5. Review: T.T.Basiev, Yu.V.Orlovskii, K.K.Pukhov, F.Auzel, Multiphonon relaxation of the energy of electronic excitation in optical crystals doped with rare-earth ions, Laser Physics, **7**, 1139 (1997)
6. Yu.V. Orlovskii, T.T.Basiev, S.A.Abalakin, I.N.Vorob'ev, O.K.Alimov, A.G.Papashvili, K.K.Pukhov, J. Lumin., 768-777, 371 (1998)
7. Yu.V. Orlovskii, T.T.Basiev, V.V.Osiko, H.Gross, J.Heber, J. Lumin., 82, 251 (1999)
8. L.A.Riseberg and H.W.Moos, Phys. Rev., **174**, 429 (1968)
9. M.J.Weber, Phys.Rev, 157, 262 (1967)
10. W.B. Fowler and D.L. Dexter, Phys. Rev. **128**, 2154 (1962)
11. M.J. Weber, J.Chem. Phys. **48**, 4774 (1968)

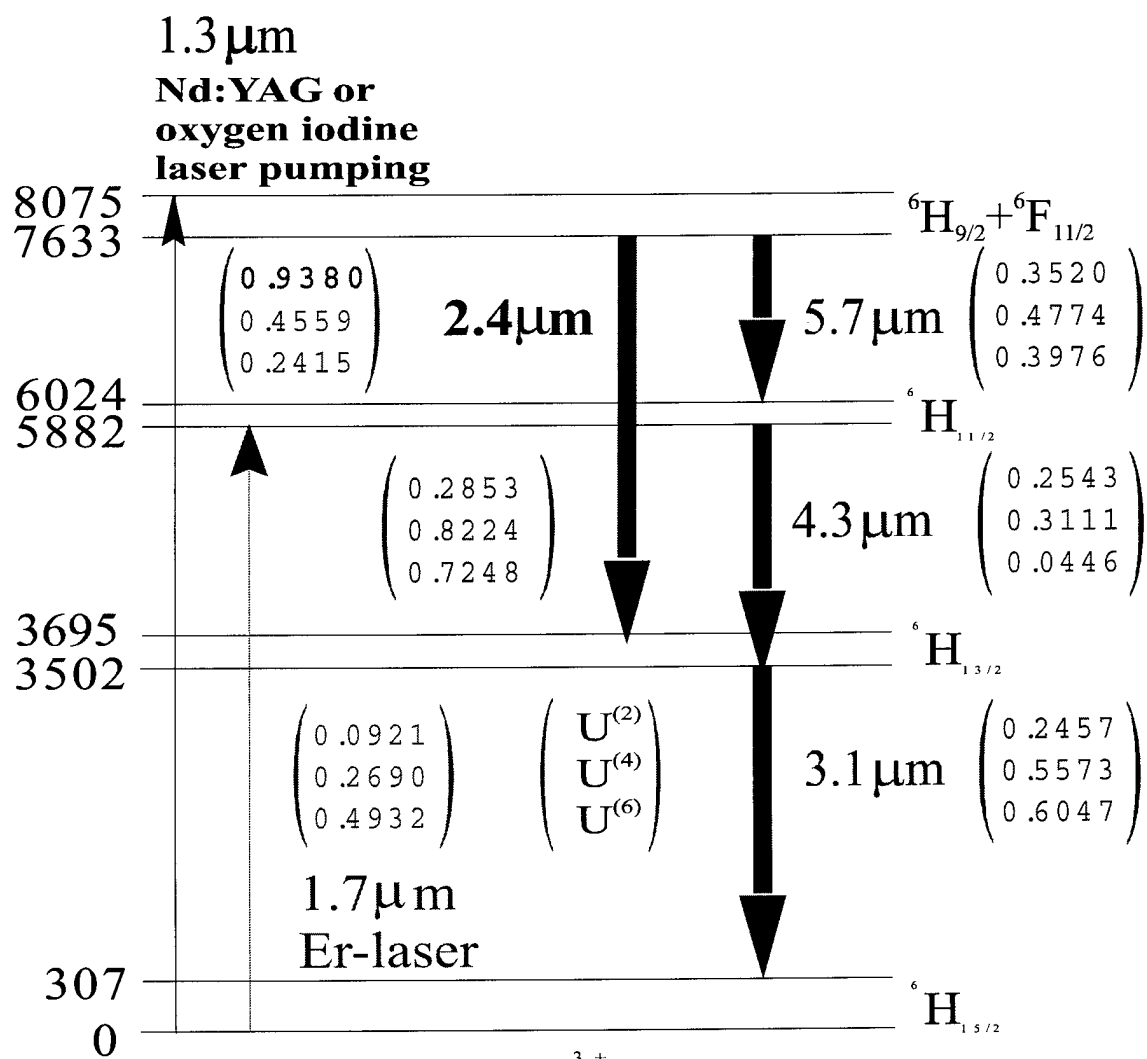
## **Chapter 2**

### **Crystals and glasses doped with dysprosium ion.**

#### **2.1 Analysis of energy level scheme and spectroscopic parameters for Dy<sup>3+</sup> doped crystals and glasses.**

Another perspective candidate for mid- IR lasing is the  $4.3 \mu\text{m}$   ${}^6\text{H}_{11/2} \rightarrow {}^6\text{H}_{13/2}$  transition of Dy<sup>3+</sup> which can be populated by multiphonon relaxation after laser pumping into higher lying levels (Figs. 2.1-2.3) or by direct pumping by  $1.7 \mu\text{m}$  laser at the  ${}^6\text{H}_{15/2} \rightarrow {}^6\text{H}_{11/2}$  transition (Fig. 2.1). Our preliminary calculations show that due to higher reduced matrix elements U(2) and U(4) of the electro- dipole transition the total emission cross- section for Dy<sup>3+</sup>  $4.34 \mu\text{m}$  transition, for example, in the LaF<sub>3</sub> crystal ( $\int \sigma_{em} d\nu = 7.1 \cdot 10^{-19} \text{ cm}$ ) is nearly 5 times larger than for the  $4.95 \mu\text{m}$  transition of Er<sup>3+</sup> ( $\int \sigma_{em} d\nu = 1.5 \cdot 10^{-19} \text{ cm}$ ). This makes it more promising for lasing. The simplest way is to pump the upper laser level with the first harmonics of YAG: Nd  $1.32 \mu\text{m}$  or oxygen iodine laser ( $\lambda_{ex.} = 1.3 \mu\text{m}$ ) into the  ${}^6\text{H}_{9/2}$ ;  ${}^6\text{F}_{11/2}$  state with very large reduced matrix element U(2) = 0.9380 and rather large U(4) = 0.4559 and U(6) = 0.2415 of the  ${}^6\text{H}_{15/2} \rightarrow {}^6\text{H}_{9/2}$ ;  ${}^6\text{F}_{11/2}$  transition (Fig. 2.1). This pumping has the advantage because there exist several crystals and glasses doped with Dy<sup>3+</sup> having large and very large intensity parameter  $\Omega(2)$  and low multiphonon relaxation rate due to low maximum phonon frequency of the matrix. For example, these are KPb<sub>2</sub>Cl<sub>5</sub>:Dy<sup>3+</sup> crystal ( $\hbar\omega_{\text{max}} = 200\text{cm}^{-1}$ ) and La<sub>2</sub>S<sub>3</sub>: Ga<sub>2</sub>S<sub>3</sub>: GeS<sub>2</sub>:Dy<sub>2</sub>S<sub>3</sub> glass ( $\hbar\omega_{\text{max}} = 350\text{cm}^{-1}$ ). The first one was preliminary investigated in [1]. Some spectroscopic parameters obtained for this crystal as well as for several chalcogenide solid state matrixes are presented in Table 2.1.





**Dy**  
( $\Omega_2=23$ )

KPb<sub>2</sub>Cl<sub>5</sub>  
(La<sub>2</sub>Ga<sub>2</sub>)<sub>2</sub>S<sub>3</sub>GeS<sub>2</sub> ( $\Omega_2=17.4$ )  
CaGa<sub>2</sub>S<sub>4</sub>; La<sub>2</sub>O<sub>2</sub>S  
Y<sub>2</sub>O<sub>3</sub>; YVO<sub>4</sub>  
LaBr<sub>3</sub>; LaI<sub>3</sub>

Fig. 2.1 Energy level scheme of 2, 3, 4 and 5 μm Dy<sup>3+</sup> lasers.

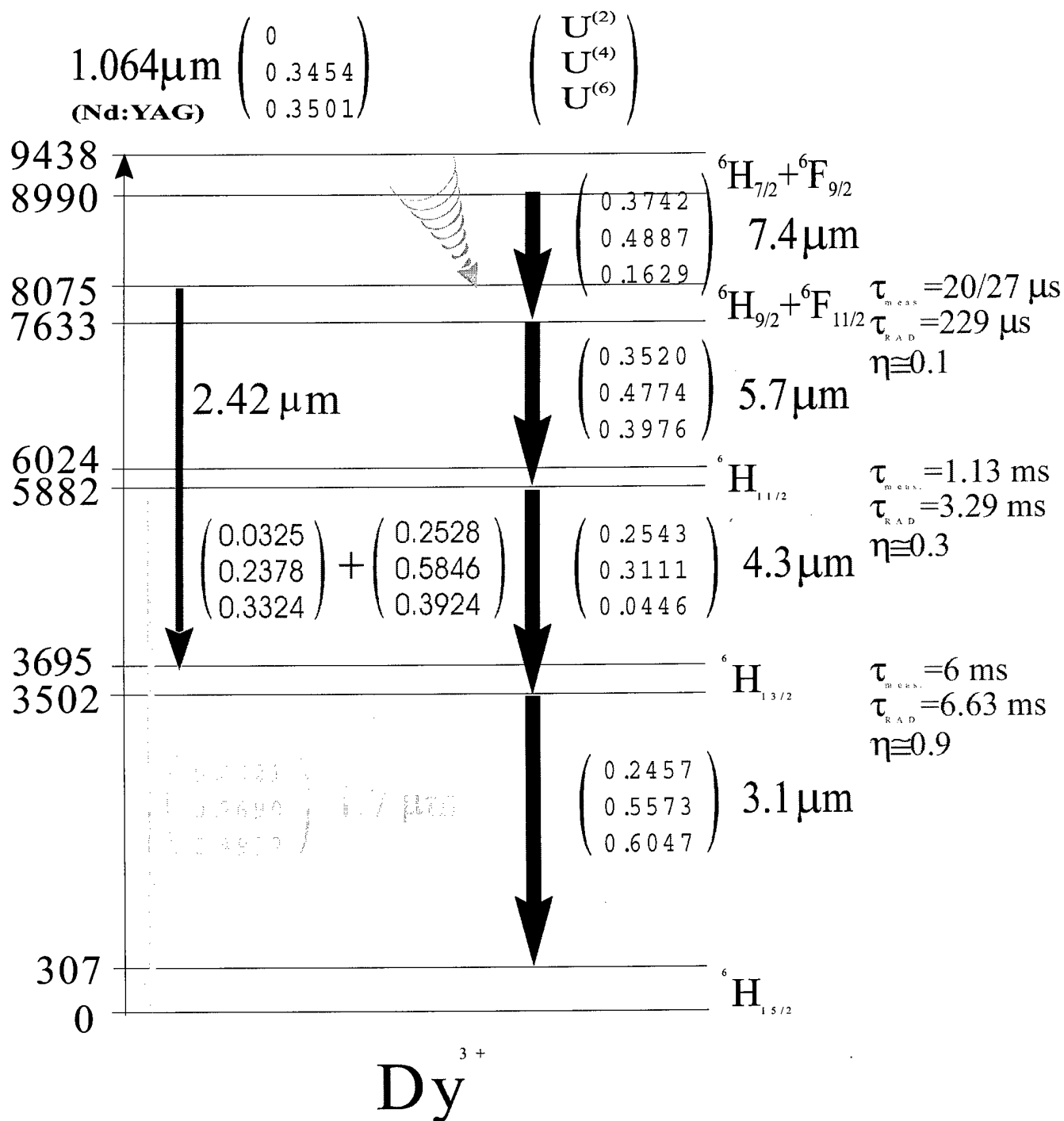


Fig. 2.2 LaGaGe sulfide glass mid-IR laser channels.

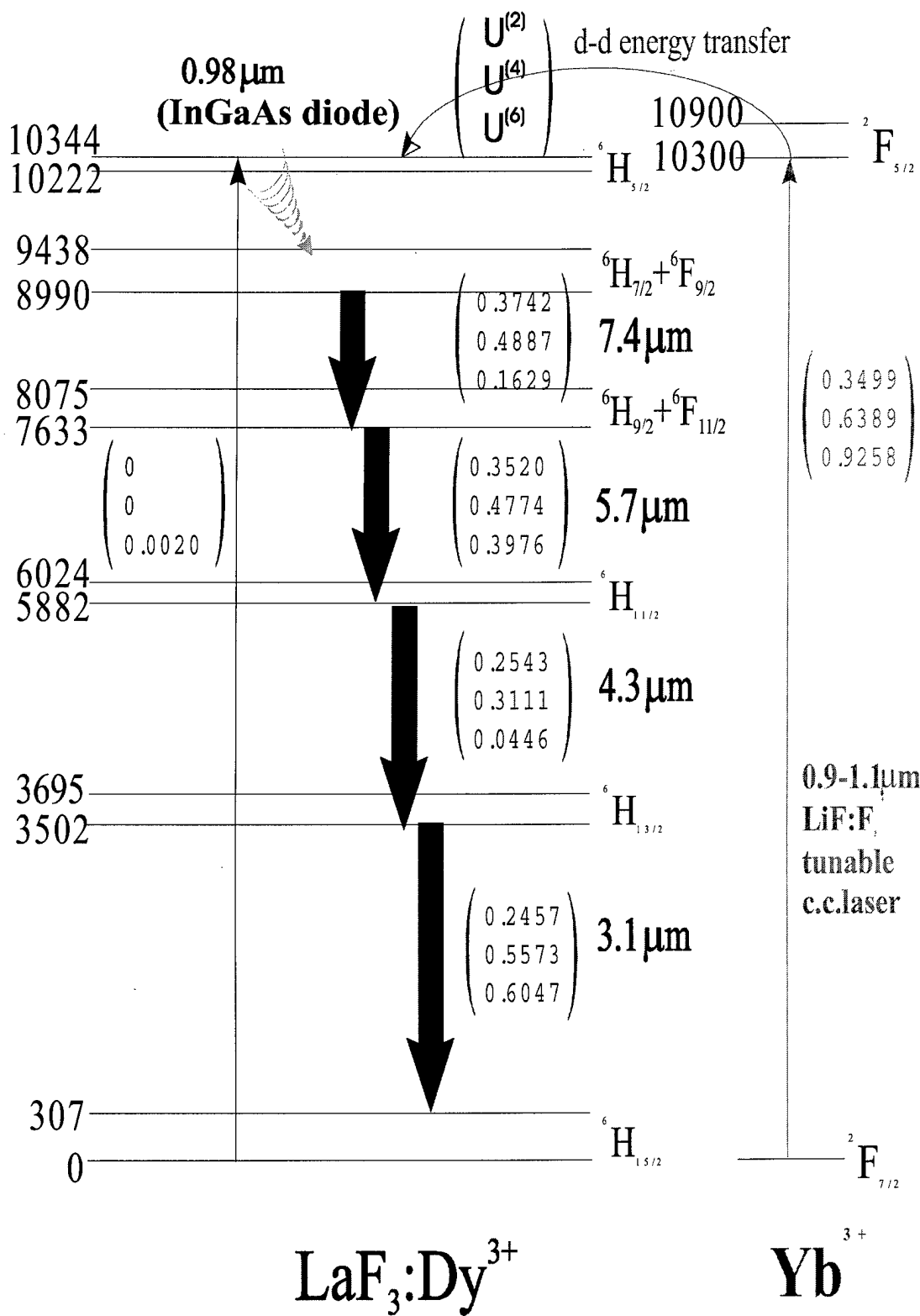


Fig. 2.3  $\text{Yb}^{3+} \rightarrow \text{Dy}^{3+}$  sensitization.

Table 2.1 Some measured at T=300K and calculated spectroscopic parameters of the low lying states of Dy<sup>3+</sup> doped chloride crystal and sulfide crystals and glasses perspective for mid-IR lasing.

Dy <sup>3+</sup>	KPb <sub>2</sub> Cl <sub>5</sub> :DyCl <sub>3</sub> (0.7 mol.%) [1]	CaGa <sub>2</sub> S <sub>4</sub> : Dy <sub>2</sub> S <sub>3</sub> [2]	Ge <sub>25</sub> Ga <sub>5</sub> S <sub>70</sub> : Dy <sub>2</sub> S <sub>3</sub> [3]	La <sub>2</sub> S <sub>3</sub> :Ga <sub>2</sub> S <sub>3</sub> : GeS <sub>2</sub> : Dy <sub>2</sub> S <sub>3</sub> (0.1 mol.%) [this work]
<sup>6</sup> H <sub>9/2</sub> ; <sup>6</sup> F <sub>11/2</sub>				
τ <sub>meas</sub> , μs	605	160	38	21.2
τ <sub>rad</sub> , μs	581	520	229	280
τ <sub>MR</sub> , μs	∞	231	45.5	22.9
η <sub>MR</sub> from the <sup>6</sup> H <sub>9/2</sub> ; <sup>6</sup> F <sub>11/2</sub> state	0	0.7	0.83	0.89
<sup>6</sup> H <sub>15/2</sub> → <sup>6</sup> H <sub>9/2</sub> ; <sup>6</sup> F <sub>11/2</sub> absorption cross- section, x10 <sup>20</sup> cm <sup>2</sup>	5.18	1.6	-	2.45
<sup>6</sup> H <sub>11/2</sub>				
τ <sub>meas</sub> , ms	6.5	2.9	1.13	0.45/1.1
τ <sub>rad</sub> , ms	4	4.16	3.29	2.3
τ <sub>MR</sub> , ms	0	9.57	1.72	0.56/2.51
σ <sub>em</sub> (λ <sub>max</sub> = 4.3 μm) x10 <sup>-20</sup> cm <sup>2</sup> ,	1.3	1.4	-	0.46
<sup>6</sup> H <sub>13/2</sub>				
τ <sub>meas</sub> , ms	11.7	6.9	6	1.9
τ <sub>rad</sub> , ms	11.9	13.2	6.63	4.6
τ <sub>MR</sub> , ms	700	15	0	3.2
hω <sub>max</sub> , cm <sup>-1</sup>	200	~350	~350	~350
(Ω <sub>2</sub> Ω <sub>4</sub> Ω <sub>6</sub> ) x10 <sup>20</sup> cm <sup>2</sup>	(23 3.3 3.9)	(3.78 2.02 1.94)		(17.4 3.6 0)
Notes	The kinetics of fluorescence decay was measured at the 5.4 μm and 4.34 μm registration	Laser generation was obtained at the 4.38 μm under 1.3 μm laser pumping [4]		The kinetics of fluorescence decay was measured at the 4.34 μm registration

Table 2.1 presents the measured and calculated radiative lifetimes of the <sup>6</sup>H<sub>9/2</sub>; <sup>6</sup>F<sub>11/2</sub>, <sup>6</sup>H<sub>11/2</sub> and <sup>6</sup>H<sub>13/2</sub> states participated in the four level scheme of 4.3 μm mid- IR lasing. The values for the CaGa<sub>2</sub>S<sub>4</sub>: Dy<sup>3+</sup> crystal were taken from Ref. [2]. Those for

the  $\text{GeS}_2\text{Ga}_2\text{S}_3\text{Dy}_2\text{S}_3$  glass were taken from Ref.[3]. The  $\text{La}_2\text{S}_3\text{Ga}_2\text{S}_3\text{GeS}_2\text{Dy}_2\text{S}_3$  glass was synthesized and melted in Laser Materials and Technologies Research Center of GPI. The parameters for the  $\text{La}_2\text{S}_3\text{Ga}_2\text{S}_3\text{GeS}_2\text{Dy}_2\text{S}_3$  were measured and calculated in this work. Analysis of Table 2.1 shows a decrease of the measured lifetime for the initial laser  ${}^6\text{H}_{11/2}$  state in the row from the  $\text{KPb}_2\text{Cl}_5:\text{Dy}^{3+}$  (0.7 mol.%) chloride crystal ( $\tau_{\text{meas.}} = 6.5$  ms [1]) to the  $\text{LaGaGeS}:\text{Dy}^{3+}$  (0.1 mol.%) sulfide glass ( $\tau_{\text{meas.}} = 0.45 \pm 1.1$  ms) (see Fig. 2.6a). In the latter case nonexponential decay was registered and two values show the result of curve fitting by two exponential decay. The decrease of the lifetime in sulfide glass is connected both with the decrease of radiative lifetime and the increase of multiphonon relaxation rate. First and only ever demonstrated beyond 4  $\mu\text{m}$  lasing in not moisture sensitive sulfide matrices was achieved in the  $\text{CaGa}_2\text{S}_4:\text{Dy}^{3+}$  crystal ( $\lambda_{\text{gen.}} = 4.38$   $\mu\text{m}$ ) presented in Ref. [4]. The absorption cross-section  $\sigma_{\text{abs.}}(\lambda_{\text{max}})$  at the  ${}^6\text{H}_{15/2} \rightarrow {}^6\text{H}_{9/2}, {}^6\text{F}_{11/2}$  transition for the  $\text{LaGaGeS}:\text{Dy}^{3+}$  glass was found even higher than for the  $\text{CaGa}_2\text{S}_4:\text{Dy}^{3+}$  crystal (Table 2.1) where 4.38  $\mu\text{m}$  lasing at 1.32  $\mu\text{m}$  laser pumping was achieved [4]. These results give the chance to obtain 4.3-4.5  $\mu\text{m}$  lasing in the  $\text{LaGaGeS}:\text{Dy}^{3+}$  sulfide glass in the four-level self terminated laser scheme. The calculated radiative lifetimes, branching ratio, integral absorption and fluorescence emission cross-sections together with line-strengths of electro-dipole and magneto-dipole transitions for the energy states participated in the 4.3  $\mu\text{m}$  lasing in this glass are presented in Table 2.2.

Table 2.2(a). Calculated absorption characteristics of  $Dy^{3+}$  in LaGaGeS glass.

Transition ${}^6\text{H}_{15/2} \rightarrow$	Energy $\text{cm}^{-1}$	$S_{\text{cd}}$ $10^{-20} \text{ cm}^2$	$S_{\text{md}}$ $10^{-20} \text{ cm}^2$	$\int \sigma_{\text{abs}} d\nu, \text{calc.}$ $10^{-18} \text{ cm}$		$\int \sigma_{\text{abs}} d\nu, \text{exp.}$ $10^{-18} \text{ cm}$
${}^6\text{H}_{13/2}$	3600	6.27	0.0103	3.4		3.5
${}^6\text{H}_{11/2}$	5850	2.56	0	1.9		1.8
${}^6\text{H}_{9/2}$	7700	0.08	0	0.1	17.6	16.9
${}^6\text{F}_{11/2}$	7700	17.86	0	17.5		
${}^6\text{H}_{7/2}$	9100	1.23	0	1.4	1.4	3.7
${}^6\text{F}_{9/2}$	9100	0	0	0		
${}^6\text{H}_{5/2}$	10000	0	0	0		
${}^6\text{F}_{7/2}$	11000	0.25	0	0.4		

$$\Omega_2 = 17.4 \cdot 10^{-20} cm^2; \Omega_4 = 3.6 \cdot 10^{-20} cm^2; \Omega_6 = 0$$

$S_{ed}$  is line strength for electric-dipole transition.

$S_{md}$  is line strength for magnetic-dipole transition.

$\int \sigma_{abs} dv$  is integrated absorption cross-section.

Table 2.2(b). Calculated emission characteristics of  ${}^6H_{9/2} + {}^6F_{11/2}$  manifold of  $Dy^{3+}$  ion in LaGaGeS glass.

Transition ${}^6H_{9/2} + {}^6F_{11/2} \rightarrow$	Energy $cm^{-1}$	$S_{ed}$ $10^{-20} cm^2$	$S_{md}$ $10^{-20} cm^2$	$\int \sigma_{em} dv$ $10^{-18} cm$	$A$ $s^{-1}$	$\beta$
${}^6H_{11/2}$	1850	7.83	1.61	1.65	24	0.007
${}^6H_{13/2}$	4100	7.91	0.05	3.02	220	0.062
${}^6H_{15/2}$	7700	17.94	0	12.76	3285	0.931

$\int \sigma_{em} dv$  is integrated stimulated emission cross-section.

$A$  is probability of electric-dipole and magnetic-dipole spontaneous emission

$\beta$  is branching ratio.

Radiative lifetime of  ${}^6H_{9/2} + {}^6F_{11/2}$  manifold  $\tau_0({}^6H_{9/2} + {}^6F_{11/2}) = 0.28 ms$ .

Table 2.2(c). Calculated emission characteristics of  ${}^6H_{11/2}$  multiplet of  $Dy^{3+}$  ion in LaGaGeS glass.

Transition ${}^6H_{11/2} \rightarrow$	Energy $cm^{-1}$	$S_{ed}$ $10^{-20} cm^2$	$S_{md}$ $10^{-20} cm^2$	$\int \sigma_{em} dv$ $10^{-18} cm$	$A$ $s^{-1}$	$\beta$
${}^6H_{13/2}$	2250	5.53	1.48	2.75	60	0.14
${}^6H_{15/2}$	5850	2.56	0	2.54	378	0.86

Radiative lifetime of  ${}^6H_{11/2}$  multiplet  $\tau_0({}^6H_{11/2}) = 2.3 ms$

Table 2.2(d). Calculated emission characteristics of  ${}^6H_{13/2}$  multiplet of  $Dy^{3+}$  ion in LaGaGeS glass

Transition ${}^6H_{13/2} \rightarrow$	Energy $cm^{-1}$	$S_{ed}$ $10^{-20} cm^2$	$S_{md}$ $10^{-20} cm^2$	$\int \sigma_{em} dv$ $10^{-18} cm$	$A$ $s^{-1}$
${}^6H_{15/2}$	3600	6.27	1.03	3.40	219

Radiative lifetime of  ${}^6H_{13/2}$  multiplet  $\tau_0({}^6H_{13/2}) = 4.6 ms$

The measured absorption cross- sections for different pumping transitions at their maximum wavelengths are presented in Table 2.3, (see also Fig. 2.4) which is in consistent with the matrix elements of the respective transitions (Table 2.3). Similar absorption spectra for  $\text{LaF}_3:\text{DyF}_3$  (0.3 mol.%) is presented in Fig. 2.5. For example, 1.064 $\mu\text{m}$  YAG: Nd laser pumping into the  ${}^6\text{H}_{7/2}; {}^6\text{F}_{9/2}$  state (Fig. 2.2) seems not to be very effective because of zero reduced matrix element  $U(2)$ . The efficiency of direct laser pumping into the  ${}^6\text{H}_{5/2}$  state by the 0.98  $\mu\text{m}$  of InGaAs diode laser or by tunable  $\text{LiF: F}_2^+$  color center laser can be increased by  $\text{Yb}^{3+}$  sensitization (Fig. 2.3) which have large reduced matrix elements  $U(k)$  of the  ${}^2\text{F}_{7/2} \rightarrow {}^2\text{F}_{5/2}$  transition ( $U(2)=0.3499$ ,  $U(4)=0.6389$ ,  $U(6)= 0.9258$ ) in comparison with the  ${}^6\text{H}_{15/2} \rightarrow {}^6\text{H}_{5/2}$  one ( $U(2)=0$ ,  $U(4)=0$ ,  $U(6)= 0.0020$ ) and strong phonon-sidebands.

**Table 2.3. The measured absorption cross- sections for different pumping transitions in their maximum wavelength in the  $\text{LaGaGeS:Dy}^{3+}$  sulfide glass at  $T=300\text{K}$ .**

Transition	$\sigma_{\text{abs.}} (\lambda_{\text{max}}), \times 10^{20}$ $\text{cm}^2$	$U(2)$	$U(4)$	$U(6)$
${}^6\text{H}_{15/2} \rightarrow {}^6\text{F}_{7/2}$	0.36	0	0.0712	0.2899
${}^6\text{H}_{15/2} \rightarrow {}^6\text{H}_{7/2}; {}^6\text{F}_{9/2}$	0.52	0	0.3454	0.3501
${}^6\text{H}_{15/2} \rightarrow {}^6\text{H}_{9/2}; {}^6\text{F}_{11/2}$	2.45	0.9380	0.4559	0.2415
${}^6\text{H}_{15/2} \rightarrow {}^6\text{H}_{11/2}$	0.35	0.0921	0.2690	0.4932
${}^6\text{H}_{15/2} \rightarrow {}^6\text{H}_{13/2}$	0.98	0.2457	0.5573	0.6047

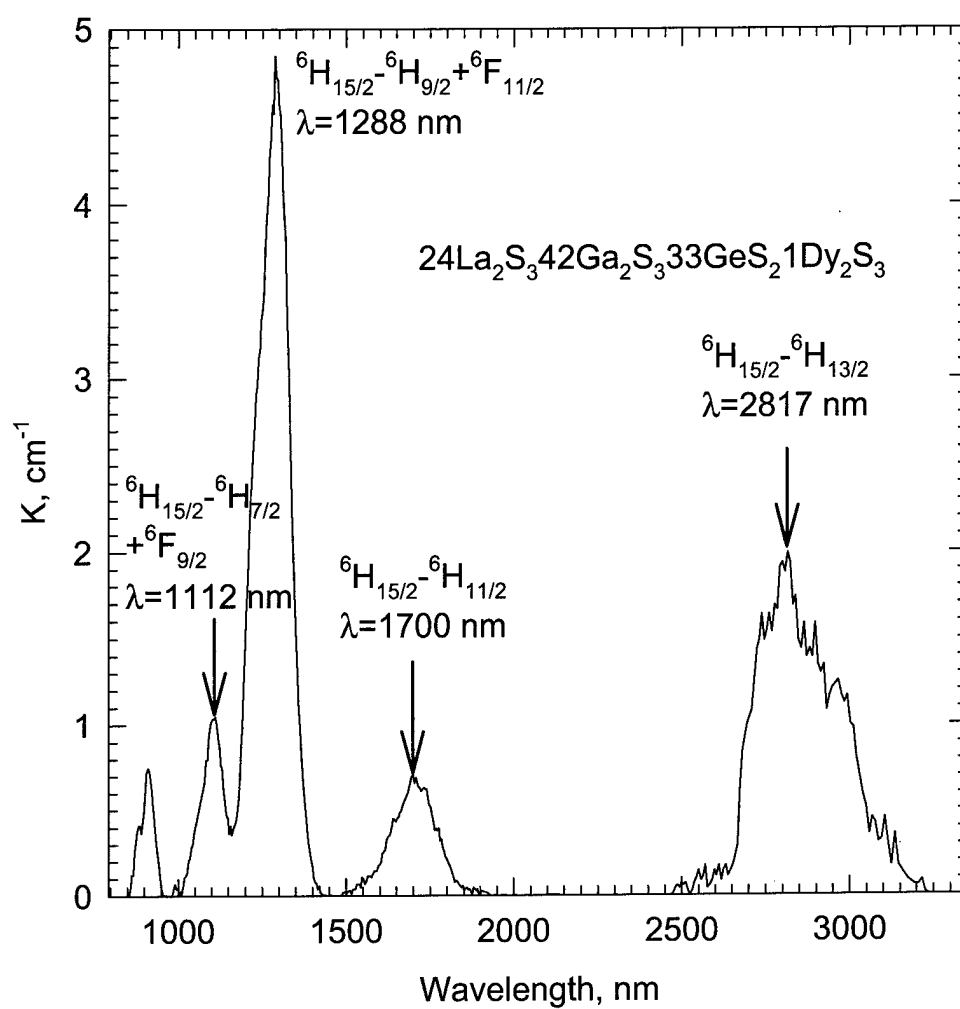


Fig. 2.4 Absorption spectrum of La, Ga, Ge glass: 1  $\text{Dy}_2\text{S}_3$ .



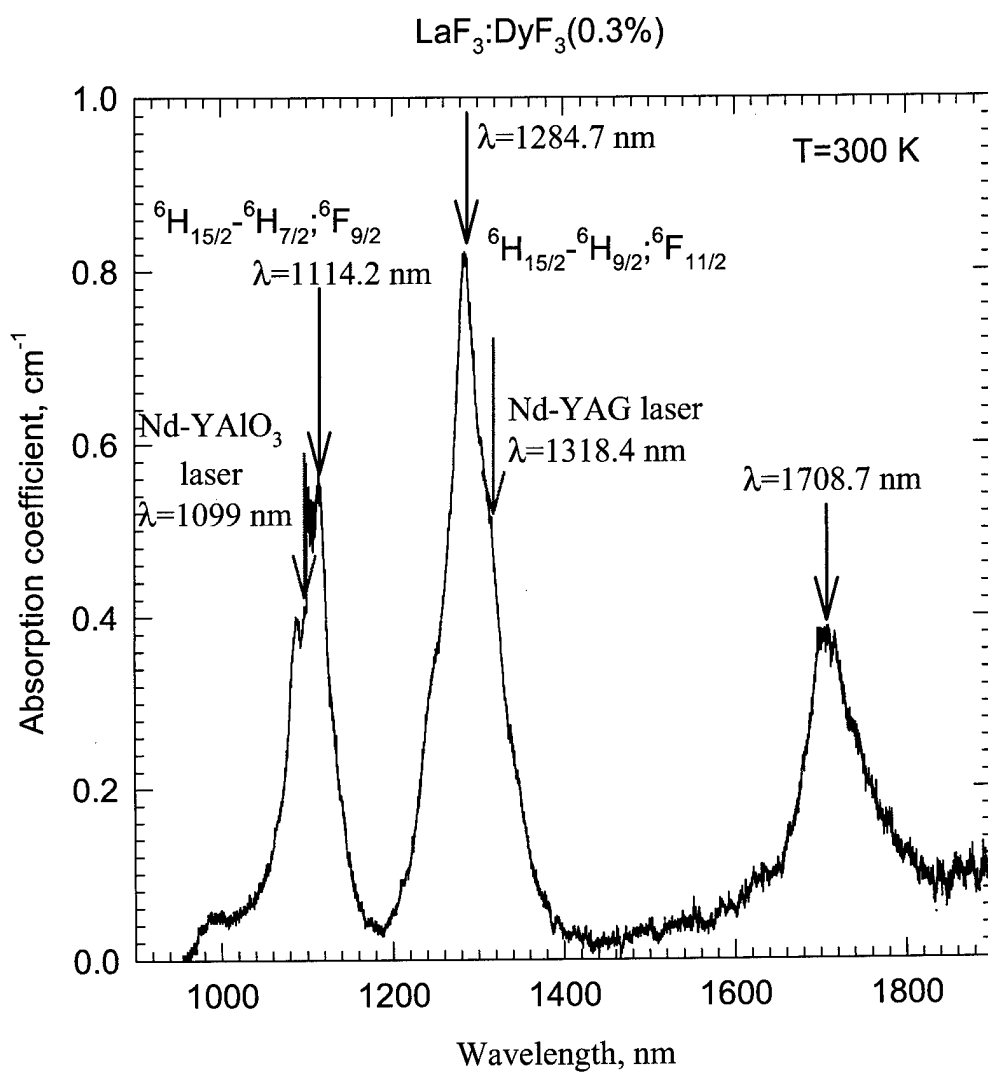


Fig. 2.5 Absorption spectrum of  $\text{LaF}_3:\text{DyF}_3(0.3\%)$  crystal.

## 2.2. Fluorescence kinetics decay measurements of $\text{Dy}^{3+}$ doped crystals and glasses.

We have compared the fluorescence kinetics decay curves of the  ${}^6\text{H}_{11/2}$  state in different solid state matrixes with the YAG:Nd 1.32  $\mu\text{m}$  laser pumping at 300 K. The fluorescence kinetics decay was registered both at the 1.7  $\mu\text{m}$   ${}^6\text{H}_{11/2} \rightarrow {}^6\text{H}_{15/2}$  transition and the 4.3  $\mu\text{m}$   ${}^6\text{H}_{11/2} \rightarrow {}^6\text{H}_{13/2}$  transition using 1.318  $\mu\text{m}$  Q-switched YAG: Nd laser pumping with  $f=1$  Hz and  $t_p=60$  nsec and pulse energy of 75 mJ. In the first case MDR-23U monochromator (LOMO) with 300 grooves/mm grating was used for spectral selection. In the second case special filter from the set of above mentioned monochromator with transmission in the 3.0 –5.3  $\mu\text{m}$  spectral region was used. Ge-photodiode as well as PbS and Ge(Au) photodetectors were used in these measurements.

For the  $\text{KPb}_2\text{Cl}_5:\text{DyF}_3$  (0.7 mol%) crystal the kinetics decay is pure exponential with  $\tau=6.5$  ms [1]. No evidence of cross-relaxation fluorescence quenching was observed. This fact deals with the lack of electronic cross-relaxation resonances for the  ${}^6\text{H}_{11/2}$  state. For the (LaGaGe) sulfide glass the kinetics decay was nonexponential because of the dispersion of the nonradiative relaxation rates (Fig. 2.6). For 0.1 mol.% concentration of  $\text{Dy}^{3+}$  the curve fitting by two exponential curves gives the values of  $\tau_1=0.45$  and  $\tau_2=1.1$  ms (Fig. 2.6a). For 1 mol.% of  $\text{Dy}^{3+}$  the initial as well as the final stages were found a little bit shorter ( $\tau_1=0.32$  ms;  $\tau_2=0.8$  ms) (Fig. 2.6b). The shorter lifetimes for the initial and the final stages might deal with the different variations of local crystal field parameters for different concentration of  $\text{Dy}^{3+}$ .

The intensity of the fluorescence signal registered at the 4.3  $\mu\text{m}$  was stronger in the chloride crystal than in sulfide glass. As no concentration quenching was observed for the  ${}^6\text{H}_{9/2}$ ;  ${}^6\text{F}_{11/2}$  state in the  $\text{KPb}_2\text{Cl}_5:\text{DyCl}_3$  (0.7 mol.%) crystal (Fig. 2.7) and in the (LaGaGe): $\text{DyF}_3$  (1 mol.%) glass (Fig. 2.8) we may conclude that the probability of population of the  ${}^6\text{H}_{11/2}$  (initial laser level for the 4.3  $\mu\text{m}$  lasing) in the  $\text{KPb}_2\text{Cl}_5:\text{Dy}^{3+}$

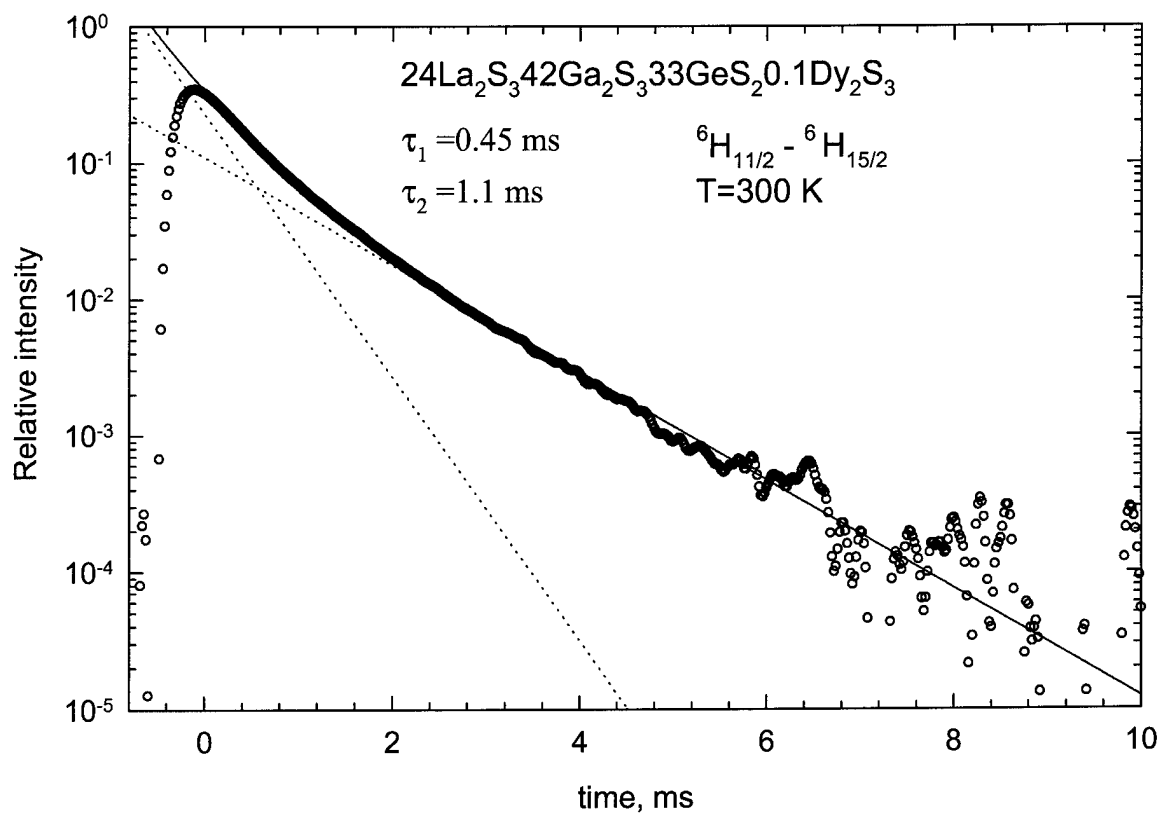


Fig. 2.6(a) Kinetics of fluorescence decay of the  ${}^6\text{H}_{11/2}$  state in the  $24\text{La}_2\text{S}_3 42\text{Ga}_2\text{S}_3 33\text{GeS}_2 0.1\text{Dy}_2\text{S}_3$  glass under  $1.32 \mu\text{m}$  YAG:Nd laser pumping at 300 K.

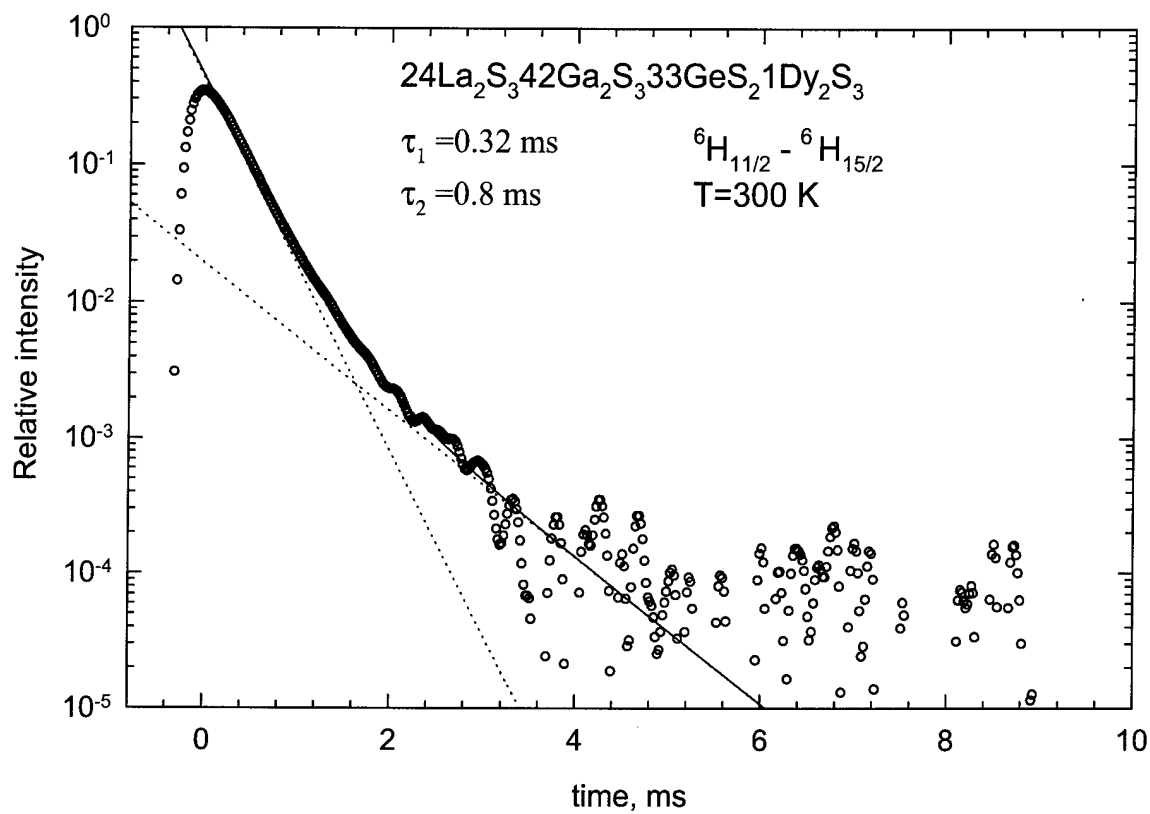


Fig. 2.6 (b) Kinetics of fluorescence decay of the  ${}^6\text{H}_{11/2}$  state in the  $24\text{La}_2\text{S}_3.42\text{Ga}_2\text{S}_3.33\text{GeS}_2.1\text{Dy}_2\text{S}_3$  glass under  $1.32 \mu\text{m}$  YAG:Nd laser pumping at 300 K.

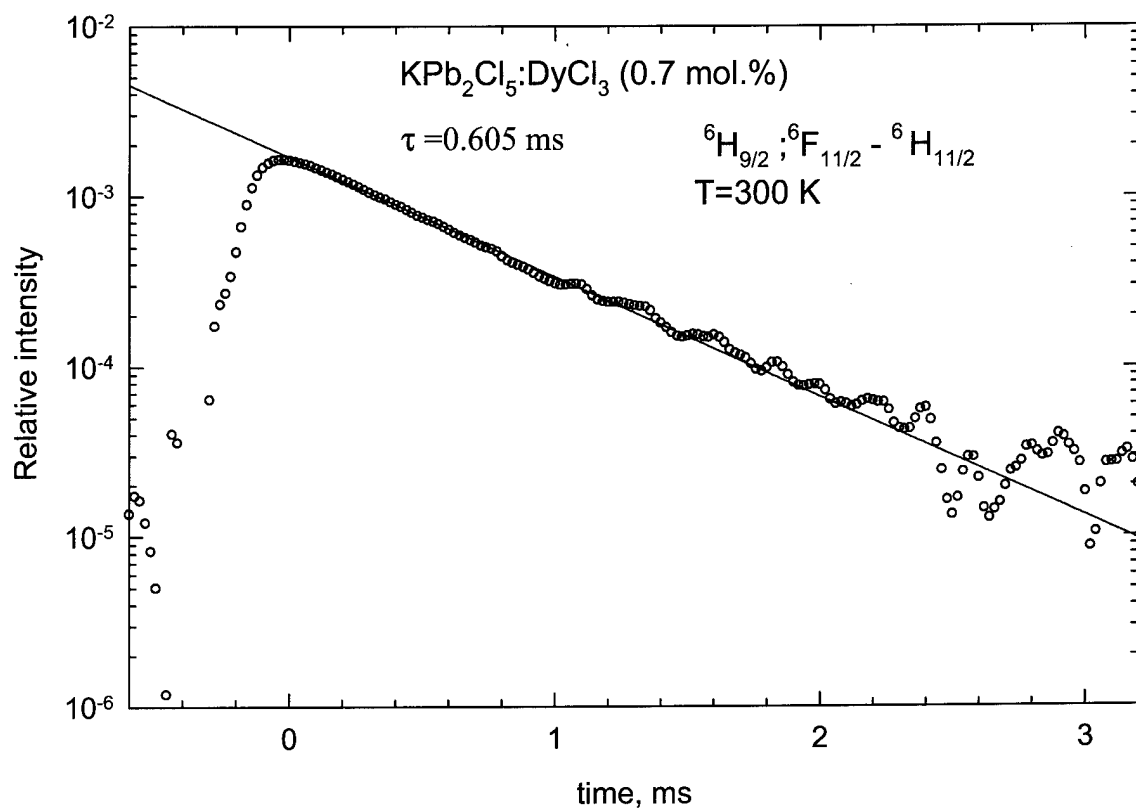


Fig. 2.7 Kinetics of fluorescence decay of the  ${}^6\text{H}_{9/2}; {}^6\text{F}_{11/2}$  state in the  $\text{KPb}_2\text{Cl}_5:\text{DyCl}_3$  (0.7 mol.%) crystal under  $1.32 \mu\text{m}$  YAG:Nd laser pumping at 300 K.

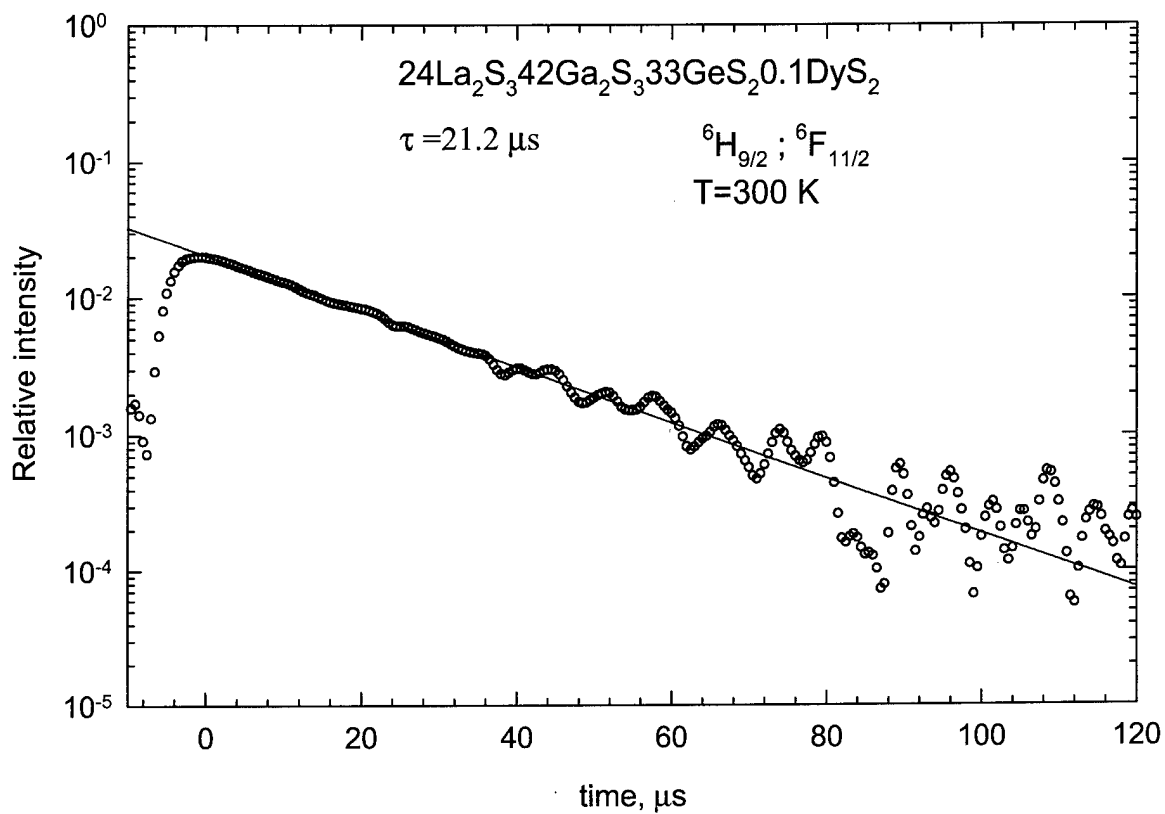


Fig. 2.8 Kinetics of 5.7 $\mu\text{m}$  fluorescence decay of the  ${}^6\text{H}_{9/2}; {}^6\text{F}_{11/2}$  state in the  $24\text{La}_2\text{S}_3.42\text{Ga}_2\text{S}_3.33\text{GeS}_2.0.1\text{Dy}_2\text{S}_3$  glass under 1.32  $\mu\text{m}$  YAG:Nd laser pumping at 300 K.

(0.7 mol.%) chloride crystal with 1.32  $\mu\text{m}$  laser pumping into the  ${}^6\text{H}_{9/2}$ ;  ${}^6\text{F}_{11/2}$  state due to intra-center relaxation is high enough in spite of the low multiphonon relaxation rate and small ( $\beta_{ij}= 0.011$  [1]) radiative probability branching ratio for the  ${}^6\text{H}_{9/2}$ ;  ${}^6\text{F}_{11/2} \rightarrow {}^6\text{H}_{11/2}$  transition. The nature of this fact will be investigated in the future studies. One of the possible reason might be the fast exciton mediated energy transfer from the  ${}^6\text{H}_{9/2}$ ;  ${}^6\text{F}_{11/2}$  to the  ${}^6\text{H}_{11/2}$  state registered for the first time in the  $\text{CsCdBr}_3$  rare- earth doped crystals by the group of Prof. J.Heber from Darmstadt Technological University.

Table 2.4 presents the values of the fluorescence kinetics lifetimes measured at the 1.7  $\mu\text{m}$  of the  ${}^6\text{H}_{11/2} \rightarrow {}^6\text{H}_{15/2}$  transition under the YAG: Nd 1.32  $\mu\text{m}$  laser pumping in solid state hosts with different anions. MDR-24U monochromator was used for spectral selection and PbS or Ge-diode photodetector was used for the fluorescence registration. The kinetics of fluorescence decay measured in the  $\text{BaF}_2\text{:Dy}^{3+}$  (10 mol.%) crystal was exponential (Fig. 2.9). No evidence of quenching energy transfer was observed. The fluorescence intensity for the  $\text{BaF}_2\text{:Dy}^{3+}$  (10 mol.%) crystal was found two orders of magnitude lower than for the  $\text{KPb}_2\text{Cl}_5\text{:Dy}^{3+}$  chloride crystal and the  $\text{LaGaGeS:Dy}^{3+}$  sulfide glass. For the  $\text{BaF}_2\text{:Dy}^{3+}$  (1 mol.%) crystal we did not manage to register the kinetics decay because the signal intensity was compared with the noise. The reason for this may be the faster multiphonon relaxation in the  $\text{BaF}_2$  matrix due to larger effective phonon frequency ( $\hbar\omega_{\text{max}}=350\text{ cm}^{-1}$ ) comparing to chloride ( $\hbar\omega_{\text{max}}=200\text{ cm}^{-1}$ ) and sulfide ( $\hbar\omega_{\text{max}}=350\text{ cm}^{-1}$ ). Also, absorption coefficient at the pumping wavelength was one order of magnitude smaller than those in chloride and sulfide. For the fluorohafnate and fluoride- chloride glasses doped with 0.1 and 1 mol.% of dysprosium the measured lifetime of the 1.7 $\mu\text{m}$  fluorescence kinetics decay at the  ${}^6\text{H}_{11/2} \rightarrow {}^6\text{H}_{15/2}$  transition was found even shorter than the response time of Ge-photodiode. In our case it was near 4  $\mu\text{s}$ . The fluorescence intensity was also found two orders of magnitude lower than for the  $\text{KPb}_2\text{Cl}_5\text{:Dy}^{3+}$  chloride crystal and the

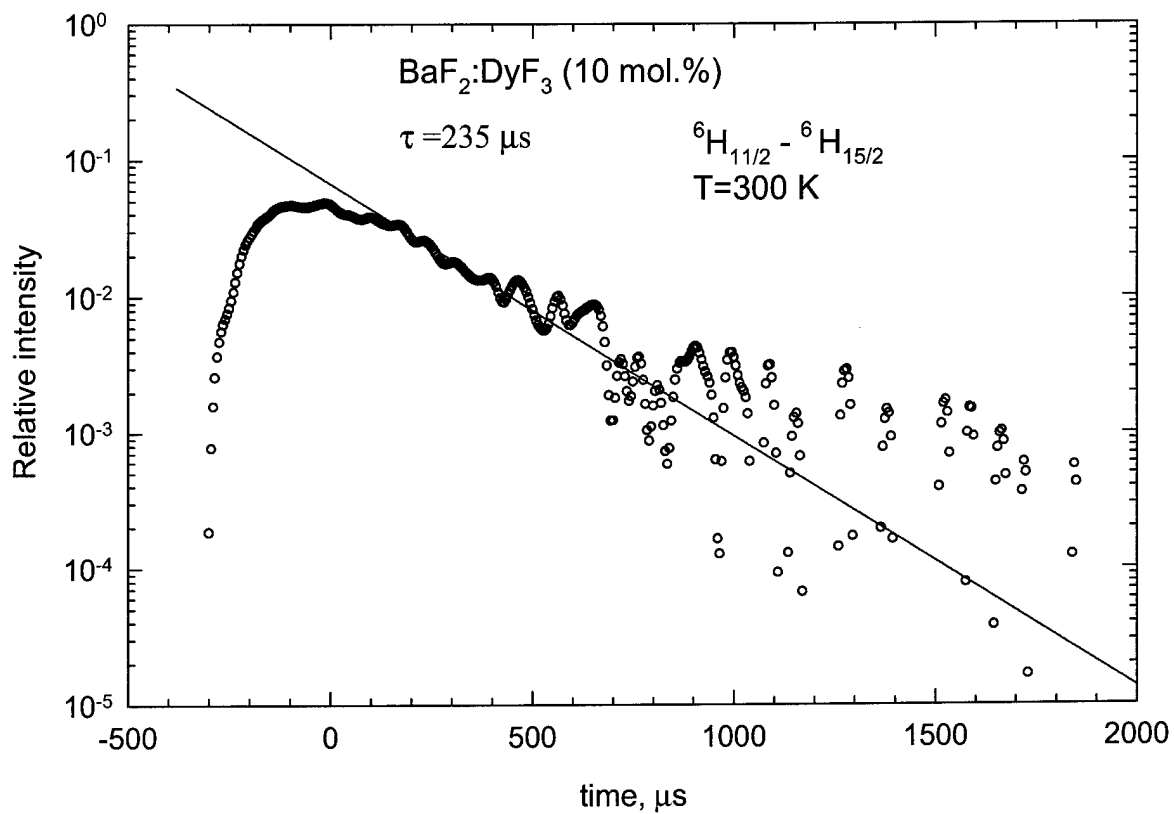


Fig. 2.9 Kinetics of fluorescence decay of the  ${}^6H_{11/2}$  state in the BaF<sub>2</sub>:DyF<sub>3</sub> (10 mol.%) crystal under 1.32  $\mu m$  YAG:Nd laser pumping at 300 K.



LaGaGeS:Dy<sup>3+</sup> sulfide glass. For the BaY<sub>2</sub>F<sub>8</sub> polycrystal strong scattering light comparable with the duration of the fluorescence kinetics decay did not allow us to measure the <sup>6</sup>H<sub>11/2</sub> state fluorescence kinetics decay.

Table 2.4. The fluorescence kinetics decay times measured at the 1.7  $\mu\text{m}$  <sup>6</sup>H<sub>11/2</sub> → <sup>6</sup>H<sub>13/2</sub> transition with the YAG: Nd 1.32  $\mu\text{m}$  laser pumping at T=300K.

Solid state matrix	Concentration of Dy <sup>3+</sup> , mol. %	$\tau_{\text{meas.}}$ , ms
KPb <sub>2</sub> Cl <sub>5</sub>	0.7	6.5
BaF <sub>2</sub>	1	Signal was not detected
	10	0.373
CdF <sub>2</sub>	0.3	$\tau_{\text{meas}} = \tau_{\text{resol}}$
25La <sub>2</sub> S <sub>3</sub> 42Ga <sub>2</sub> S <sub>3</sub> 33GeS <sub>2</sub> glass	0.1	0.45/1.1
	1	0.32/0.8
57HfF <sub>4</sub> 20BaF <sub>2</sub> 3LaF <sub>3</sub> 17NaF2.5AlF <sub>3</sub> 0.5InF <sub>3</sub> glass	1	$\tau_{\text{meas}} = \tau_{\text{resol}}$
57HfF <sub>4</sub> 20BaCl <sub>2</sub> 3LaF <sub>3</sub> 17NaF3InF <sub>3</sub> glass	1	$\tau_{\text{meas}} = \tau_{\text{resol}} / 14.9 \mu\text{s}$

For the <sup>6</sup>H<sub>9/2</sub>; <sup>6</sup>F<sub>11/2</sub> state the measured lifetimes are 605  $\mu\text{s}$  (Fig. 2.7) and 20±27  $\mu\text{s}$  (Fig.2.8) in the chloride crystal and the sulfide glass, respectively (see, also, Table 2.1). This fact deals either with the larger radiative lifetime in KPb<sub>2</sub>Cl<sub>5</sub>: Dy<sup>3+</sup> ( $\tau_{\text{rad.}} = 581\mu\text{s}$ ) than in the LaGaGe sulfide glass ( $\tau_{\text{rad.}} = 280\mu\text{s}$ ) and large multiphonon relaxation rate in the sulfide glass ( $W_{\text{MR}} = 4.37 \cdot 10^4 \text{ s}^{-1}$ ) (in the chloride crystal  $W_{\text{MR}}$  is practically zero). For the KPb<sub>2</sub>Cl<sub>5</sub>: Dy<sup>3+</sup> crystal due to practically zero rate of 8-phonon transition we have managed to measure the kinetics decay ( $\tau_{\text{meas.}} = 605 \mu\text{s}$ ) at the 5.41  $\mu\text{m}$  of the <sup>6</sup>H<sub>9/2</sub>; <sup>6</sup>F<sub>11/2</sub> → <sup>6</sup>H<sub>11/2</sub> transition using cooled (77K) Ge(Au) photodetector for fluorescence registration and special filter with transmission in the 5.3 – 9.3  $\mu\text{m}$  spectral region taken from the set of the MDR-23U monochromator (LOMO) for spectral selection. In the LaGaGeS:Dy<sup>3+</sup> glass we did not manage to register fluorescence kinetics decay at the 5.34  $\mu\text{m}$  of the <sup>6</sup>H<sub>9/2</sub>; <sup>6</sup>F<sub>11/2</sub> → <sup>6</sup>H<sub>11/2</sub> transition because of nonradiative bypass by 4- phonon transition. For the same reason we did not manage to measure the fluorescence signal at the <sup>6</sup>H<sub>9/2</sub>; <sup>6</sup>F<sub>11/2</sub> → <sup>6</sup>H<sub>11/2</sub> 5.4

$\mu\text{m}$  transition under 1.32  $\mu\text{m}$  pumping in both the  $\text{BaF}_2$  crystals with 1 and 10 mol.% of dysprosium and in substituted fluorohafnate and fluoride- chloride glasses doped with 0.1 and 1 mol.% of dysprosium.

Table 2.5 presents the values of the fluorescence kinetics decay times of the  ${}^6\text{H}_{13/2}$  terminated laser level of  $\text{Dy}^{3+}$  measured at 2.9  $\mu\text{m}$  under 1.32  $\mu\text{m}$  YAG: Nd laser pumping. The longest lifetime at small concentration of  $\text{Dy}^{3+}$  was found in the  $\text{KPb}_2\text{Cl}_5:\text{DyCl}_3$  (0.7 mol.% ) crystal. The curve fitting by two exponential curves gives the values of  $\tau_1=4.1$  ms and  $\tau_2=8.0$  ms (Fig. 2.10). The shortest lifetime at small concentrations of  $\text{Dy}^{3+}$  was found in the  $\text{HfBaFLaNaAlIn Dy}^{3+}$  glass ( $\tau=0.72$  ms at 0.1 mol. %  $\text{Dy}^{3+}$  (Fig. 2.11)).

We may conclude that the developing of  $\text{Dy}^{3+}$  doped solid state laser materials with large intensity parameters  $\Omega(2)$  and  $\Omega(4)$  and short phonon spectra like in chloride and sulfide crystals and glasses gives a good chance to obtain 5.7 and 4.3  $\mu\text{m}$  lasing at the  ${}^6\text{H}_{9/2}$ ;  ${}^6\text{F}_{11/2} \rightarrow {}^6\text{H}_{11/2}$  and the  ${}^6\text{H}_{11/2} \rightarrow {}^6\text{H}_{13/2}$  transitions of  $\text{Dy}^{3+}$ , respectively, with 1.32  $\mu\text{m}$  YAG: Nd laser pumping.

Several other dysprosium doped crystal matrices with short phonon spectra and probably with large intensity parameters  $\Omega(k)$  like  $\text{LaBr}_3$ ,  $\text{LaI}_3$ ,  $\text{La}_2\text{O}_2\text{S}$ ,  $\text{Y}_2\text{O}_3$  and  $\text{YVO}_4$  should be tested for 4.3  $\mu\text{m}$  generation, too.

Table 2.5. The fluorescence kinetics decay lifetimes measured at the 2.9  $\mu\text{m}$   ${}^6\text{H}_{13/2} \rightarrow {}^6\text{H}_{15/2}$  transition with the YAG: Nd 1.32  $\mu\text{m}$  laser pumping at  $T=300\text{K}$ .

Solid state matrix	Concentration of $\text{Dy}^{3+}$ , mol.%	$\tau_{\text{meas.}}$ , ms
$\text{KPb}_2\text{Cl}_5$	2	4.1/8.0
$\text{BaF}_2$	1	2.16
	10	0.37/0.55
$\text{BaY}_2\text{F}_8$	0.1	1.19
	0.5	1.13
	1.5	1.25
$\text{CdF}_2$	0.3	0.637
	1	0.269
	10	0.230
	30	0.206
$25\text{La}_2\text{S}_3:42\text{Ga}_2\text{S}_3:33\text{GeS}_2$ glass	0.1	1.9
	1	0.23
$57\text{HfF}_4:20\text{BaF}_2:3\text{LaF}_3:17\text{NaF}:2.5\text{AlF}_3:0.5\text{InF}_3$ glass	0.1	0.72
	1	0.56
$57\text{HfF}_4:20\text{BaCl}_2:3\text{LaF}_3:17\text{NaF}:3\text{InF}_3$ glass	1	0.58

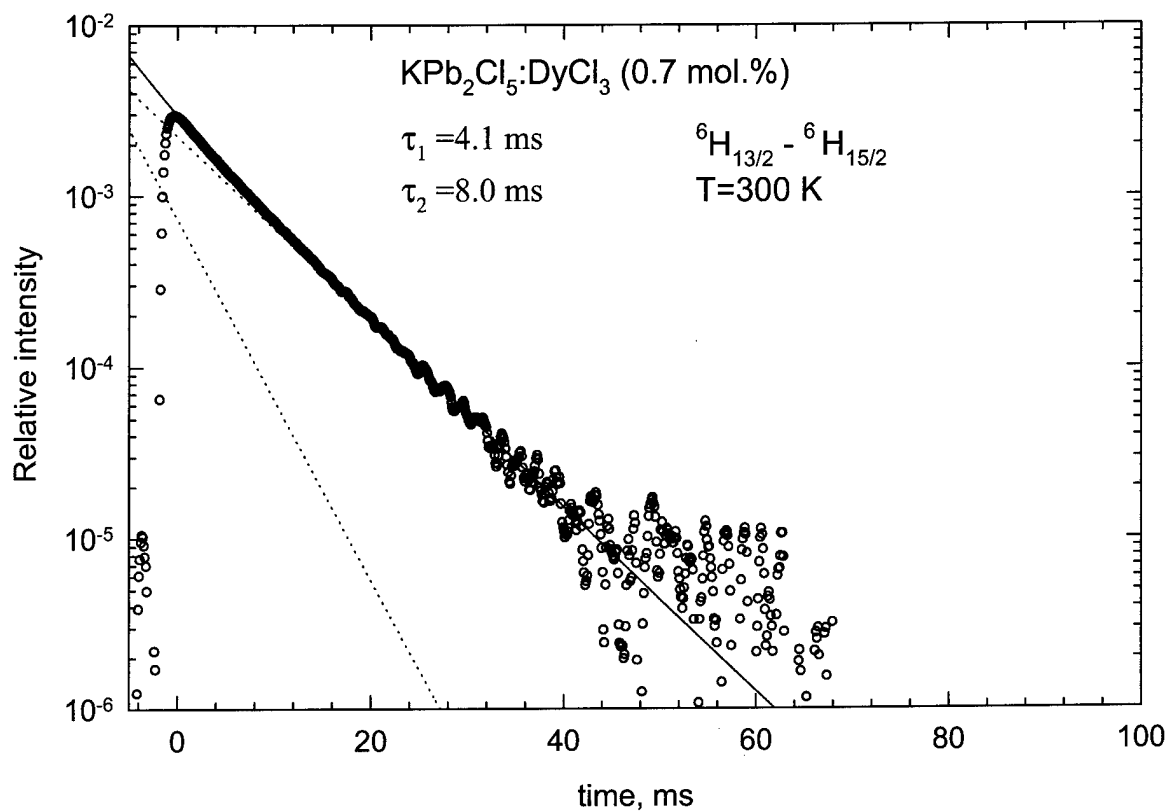


Fig. 2.10 Kinetics of fluorescence decay of the  ${}^6\text{H}_{13/2}$  state in the  $\text{KPb}_2\text{Cl}_5:\text{DyCl}_3$  (0.7 mol.%) crystal under  $1.32\text{ }\mu\text{m}$  YAG:Nd laser pumping at 300 K.

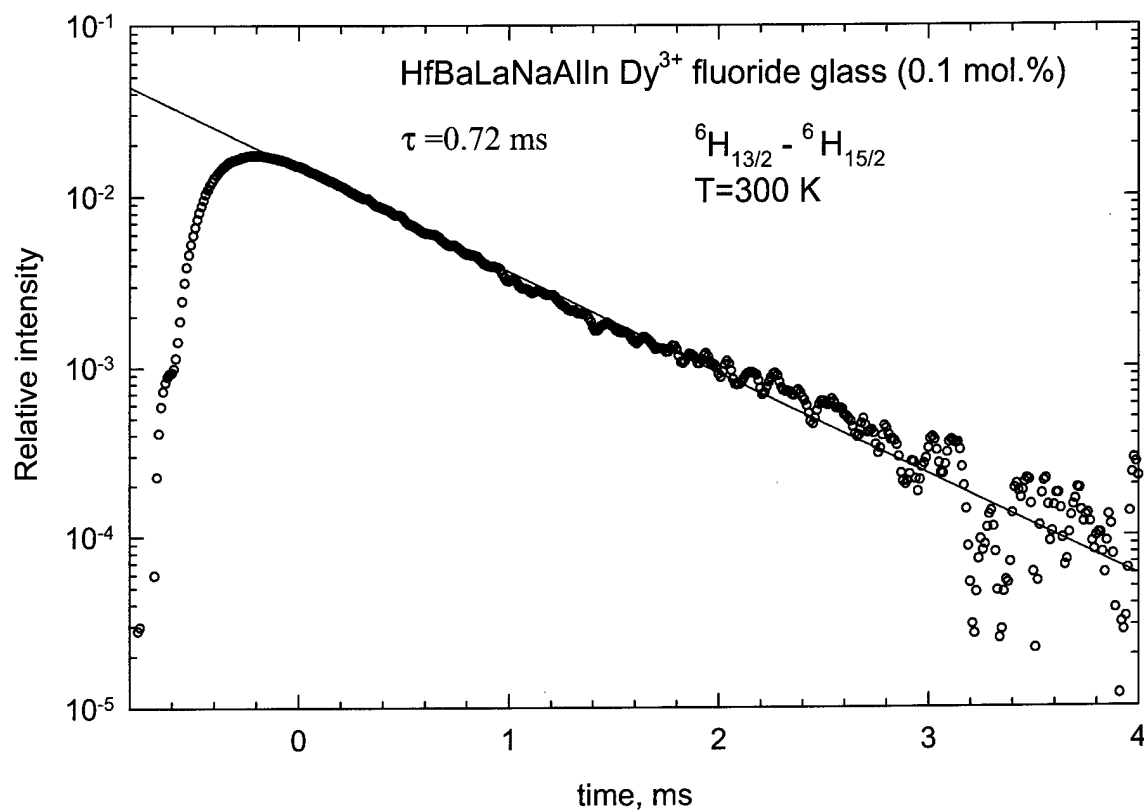


Fig. 2.11 Kinetics of fluorescence decay of the  ${}^6\text{H}_{13/2}$  state in the HfBaLaNaAlIn Dy<sup>3+</sup> (0.1 mol.%) fluoride glass under 1.32  $\mu\text{m}$  YAG:Nd laser pumping at 300 K.

### 4.3 $\mu\text{m}$ fluorescence spectra of $\text{Dy}^{3+}$ .

InSb photo-detector with 4-5  $\mu\text{m}$  top sensitivity was developed on special order and purchased by us for the measurements of the fluorescence spectra in the 4-5  $\mu\text{m}$  spectral region (Fig. 2.12). Fluorescence spectra of  $\text{Dy}^{3+}$  in 4-5  $\mu\text{m}$  spectral range (besides  $\text{KPb}_2\text{Cl}_5:\text{Dy}^{3+}$  (0.7 mol.%) crystal ) was measured using MDR-23 monochromator with 200 grooves/mm grating and with  $f/6$  effective aperture. The slit width was 1 mm at 7.8 nm reciprocal linear dispersion. The excitation was carried out at room temperature by laser diode emitting 802 nm radiation of 250 mW power modulated by mechanical chopper. The fluorescence was recorded using selective nanovoltmeter.

Fluorescence spectra of  $\text{Dy}^{3+}$  in the  $\text{KPb}_2\text{Cl}_5:\text{Dy}^{3+}$  (0.7 mol.%) crystal in 4-5  $\mu\text{m}$  spectral range was measured using double grating SDL-1 monochromator with 100 grooves/mm gratings and  $f/3$  effective aperture which is 2 times better than for MDR-23. The slit width was 0.7 mm at 9.6 nm reciprocal linear dispersion. Hence, the spectral resolution was better in the latter case. The 4-5  $\mu\text{m}$  fluorescence of  $\text{Dy}^{3+}$  ions was excited by the CW ADLAS 1W laser diode ( $\lambda=802$  nm). To separate the 4-5  $\mu\text{m}$  fluorescence from intensive 1.5-3.0  $\mu\text{m}$  fluorescence observed in higher diffraction orders the special filter transparent in 3.5-6  $\mu\text{m}$  region was used. The fluorescent signal was detected by the Ge(Au) liquid nitrogen cooled photodetector. To increase the signal to noise ratio the method of synchronous signal detection was applied. The detected signal was then recorded using an analog-digital converter and a PC. Below we present the data on 4.3  $\mu\text{m}$  luminescence of  $\text{Dy}^{3+}$  ion in different hosts (Fig. 2.13). On the left part of the figures the absorption spectra sections near 0.8 mm and the position of LD radiation are given in order to demonstrate the matching of the absorption band and excitation.

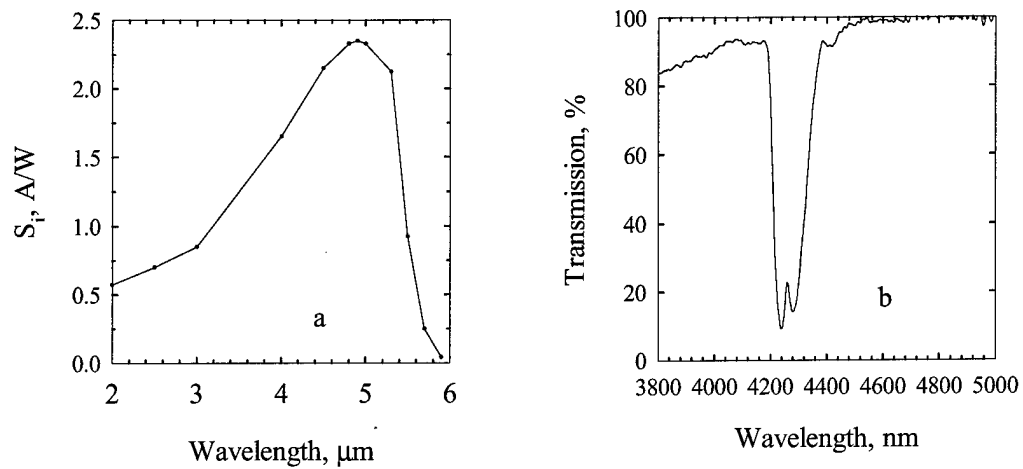
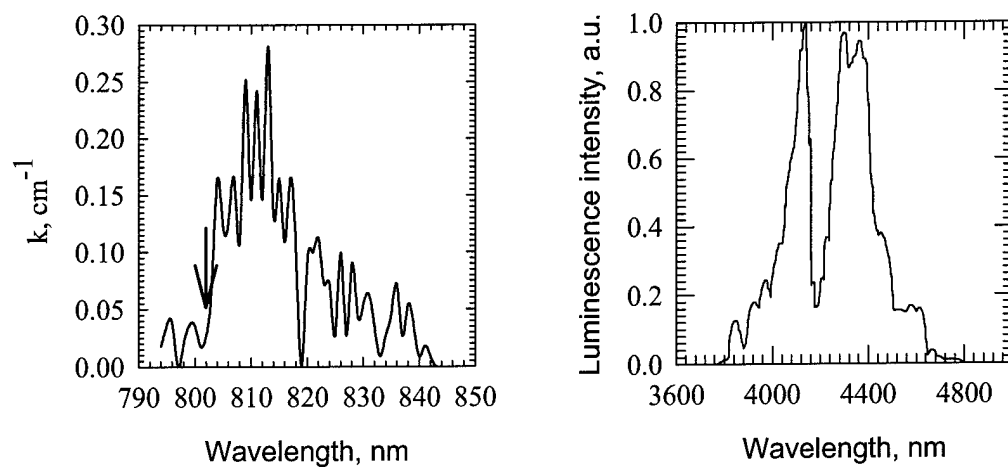


Fig. 2.12 Spectral sensitivity ( $S_i$ ) of InSb-photodiode (a) and atmosphere transmittance (optical length  $\sim 2$  m) (b); the strong absorption band is attributed to vibrational transition of  $\text{CO}_2$ .

$\text{KPb}_2\text{Cl}_5:\text{Dy}^{3+}$  (1%) - single crystal



$\text{KPb}_2\text{Cl}_5:\text{Dy}^{3+}$  (5%) - polycrystal

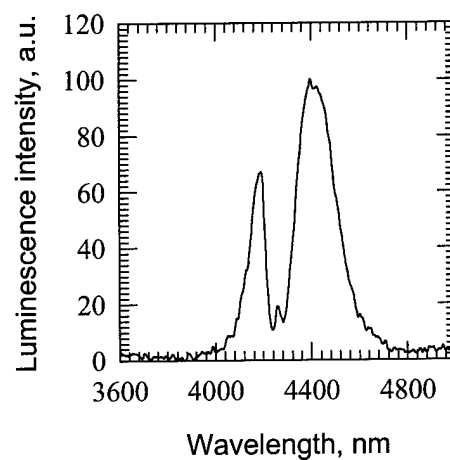


Fig. 2.13 Absorption and emission spectra of  $\text{Dy}^{3+}$ -doped materials.

Sulfide glass-  $\text{Dy}^{3+}$  (1%)

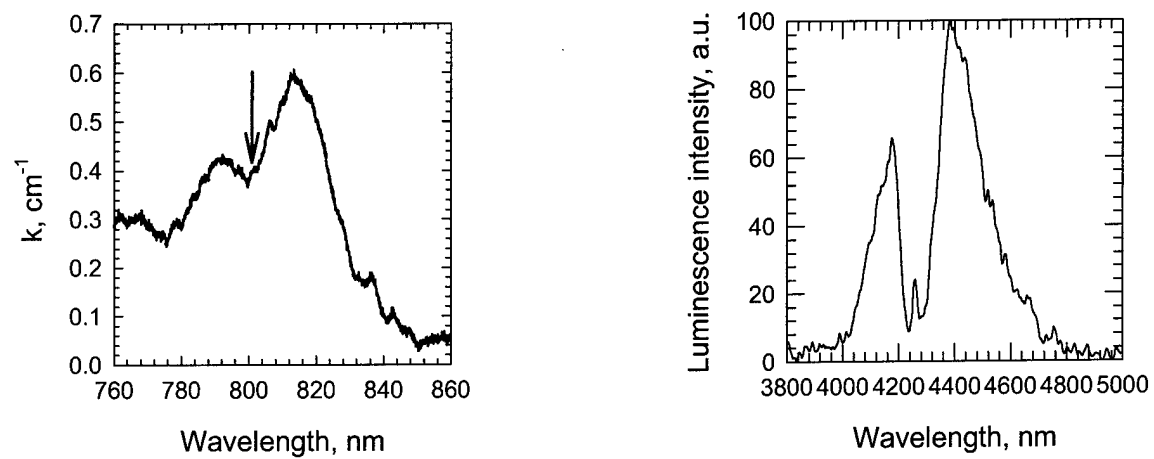


Fig. 2.13 (continued)



## References

- 1 A.Tkachuk, S.Ivanova, L.Isaenko, A.Yeliseyev, Steve Payne, R.Solarz, M.Nostrand, R.Page and Stephen Payne, Acta Physica Polonica A, 95, 381-394 (1999)
- 2 M.C.Nostrand, R.H.Page, S.A.Payne, and W.F.Krupke, OSA TOPS, v.19, Advanced Solid State Lasers, OSA (1998), p.524-528
- 3 J.Heo, OSA TOPS, v.10. Advanced Solid State Lasers, OSA (1997), p.226-231
- 4 Nostrand, R.H.Page, S.A.Payne, W.F.Krupke, P.G.Schunemann, Technical abstracts, CLEO'99 (1999) p.390

### **Chapter 3**

#### **Energy levels scheme analysis of holmium ion.**

One of the schemes of population inversion creation in holmium is the direct laser excitation by the 0.64  $\mu\text{m}$  of dye laser into the  $^5\text{F}_5$  initial laser level of the 4.3 $\mu\text{m}$   $^5\text{F}_5 \rightarrow ^5\text{I}_4$  transition (Fig. 3.1). According to the reduced matrix elements  $U(k)$  of the pumping  $^5\text{I}_8 \rightarrow ^5\text{F}_5$  transition ( $U(2)= 0$ ,  $U(4)= 0.4238$ ,  $U(6)= 0.5687$ ) this laser pumping scheme requires holmium doped crystal matrix with large intensity parameters  $\Omega(4)$  and  $\Omega(6)$  to be effective. Contrary, direct pumping of the  $^5\text{I}_5$  initial laser level of the 4.1 $\mu\text{m}$   $^5\text{I}_5 \rightarrow ^5\text{I}_6$  transition by 0.91  $\mu\text{m}$  radiation of tunable  $\text{LiF:F}_2^+$  color center laser as well as into the upper  $^5\text{I}_4$  state by 0.75  $\mu\text{m}$  of alexandrite or Ti-sapphire laser will not be effective because of small reduced matrix elements  $U(k)$  of the  $^5\text{I}_8 \rightarrow ^5\text{I}_5$  and  $^5\text{I}_8 \rightarrow ^5\text{I}_4$  transitions. The 4.3 $\mu\text{m}$   $^5\text{F}_5 \rightarrow ^5\text{I}_4$  laser transition itself has rather small reduced matrix elements  $U(k)$  ( $U(2)= 0.0001$ ,  $U(4)= 0.0060$ ,  $U(6)= 0.0038$ ) while the lower lying 5.1  $\mu\text{m}$   $^5\text{I}_4 \rightarrow ^5\text{I}_5$  transition has very large matrix element  $U(6)= 0.9080$  and large  $U(4)= 0.1237$  which fit with the large matrix element  $U(6)= 0.5687$  and  $U(4)= 0.4238$  of the dye laser pumping  $^5\text{I}_8 \rightarrow ^5\text{F}_5$  transition. The  $^5\text{I}_4$  state can be populated by the multiphonon relaxation from the  $^5\text{F}_5$  one, though this process will not be very effective because of rather large energy gap  $\Delta E= 2000 \text{ cm}^{-1}$  between the  $^5\text{F}_5$  and the  $^5\text{I}_4$  states and small matrix elements of the respective transition. Hereafter, large  $U(6)= 0.5727$  of the 4.1 $\mu\text{m}$   $^5\text{I}_5 \rightarrow ^5\text{I}_6$  transition intensified by magnetic- dipole transition gives chance to obtain 4.1 $\mu\text{m}$  lasing here. The measured excited states lifetimes  $\tau$  in the  $\text{LiYF}_4:\text{Ho}^{3+}$  crystal at 300K are also presented in Fig. 3.1. Fig. 3.2 presents the absorption spectra of the  $\text{CaF}_2:\text{HoF}_3$  (4 mol.%) crystal. The relative intensities of absorption peaks are in agreement with the values of the reduced matrix elements  $U^{(k)}$ . The maximum absorption coefficient in the peak of absorption line was found for the  $^5\text{I}_8 \rightarrow ^5\text{F}_5$  transition ( $k_{\text{max}}=2.3 \text{ cm}^{-1}$ ). The

$^5I_8 \rightarrow ^5I_7$  and  $^5I_8 \rightarrow ^5I_6$  transitions also have large  $k_{\max}$  (1.31 and 0.95  $\text{cm}^{-1}$ , respectively). While the absorption spectral lines for the  $^5I_8 \rightarrow ^5I_4$  and  $^5I_8 \rightarrow ^5I_5$  transitions are practically absent because of zero and very small matrix elements  $U^{(k)}$ . The advantage of using of the  $^5I_8 \rightarrow ^5F_5$  and the  $^5I_8 \rightarrow ^5I_6$  transitions is the possibility of tuning of the pumping laser into the maximum of absorption peaks.

For the pumping of the  $^5I_5$  initial laser level two step excitation of single  $\text{Ho}^{3+}$  ions by 2  $\mu\text{m}$  holmium laser can be used. The two step process is going through  $^5I_8 \rightarrow ^5I_7$  and  $^5I_7 \rightarrow ^5I_5$  transitions with very large matrix elements  $U(6)$  equal to 1.5218 and 0.8887, respectively, (Fig. 3.3). Another way to make excitation of the  $^5I_5$  initial laser level more effective is sensitization by ytterbium. In this case 0.98  $\mu\text{m}$  of tunable  $\text{LiF:F}_2^+$  color center laser can be used for the  $^2F_{5/2}$  state pumping (see Fig. 4.4) with the following dipole- dipole energy transfer to the  $^5I_5$  initial 4.1  $\mu\text{m}$  laser level of  $\text{Ho}^{3+}$ .  $\text{Yb}^{3+}$  transition has very large matrix element  $U(6)= 0.9258$  and large matrix elements  $U(2)= 0.3499$  and  $U(4)= 0.6389$  as well. Also, ytterbium transition is intensified by magnetic- dipole one and has strong phonon side-bands. The latter scheme of the  $^5I_5$  initial laser level pumping seems more effective than those of the direct pumping.

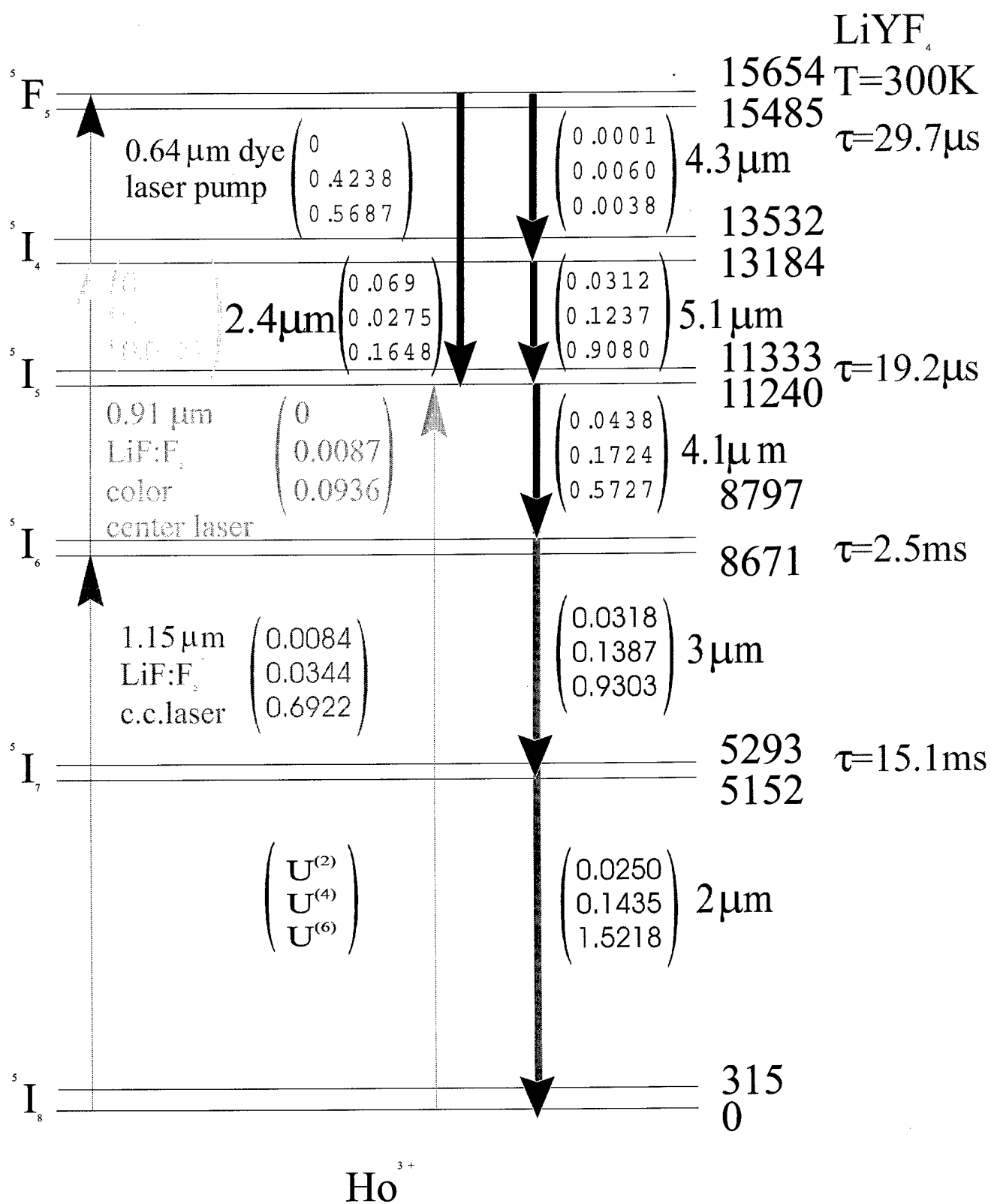


Fig. 3.1 Direct pumping of  $\text{Ho}^{3+}$  mid-IR transitions

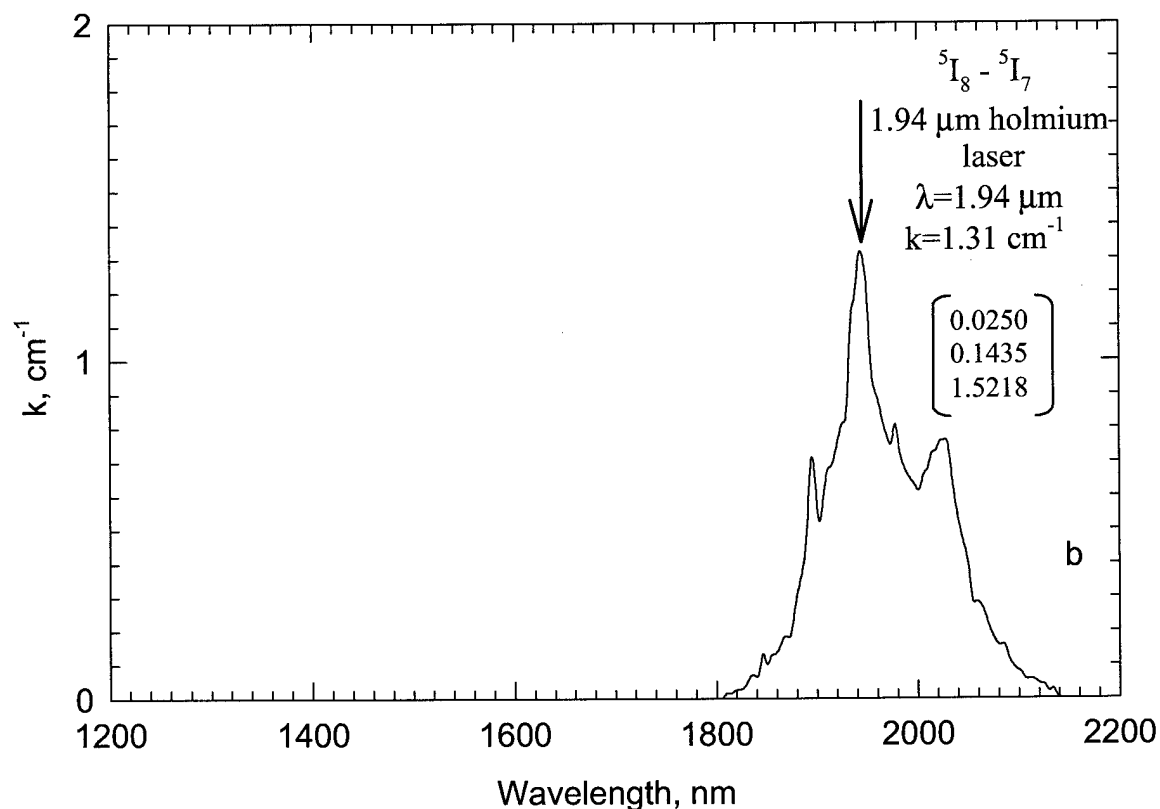
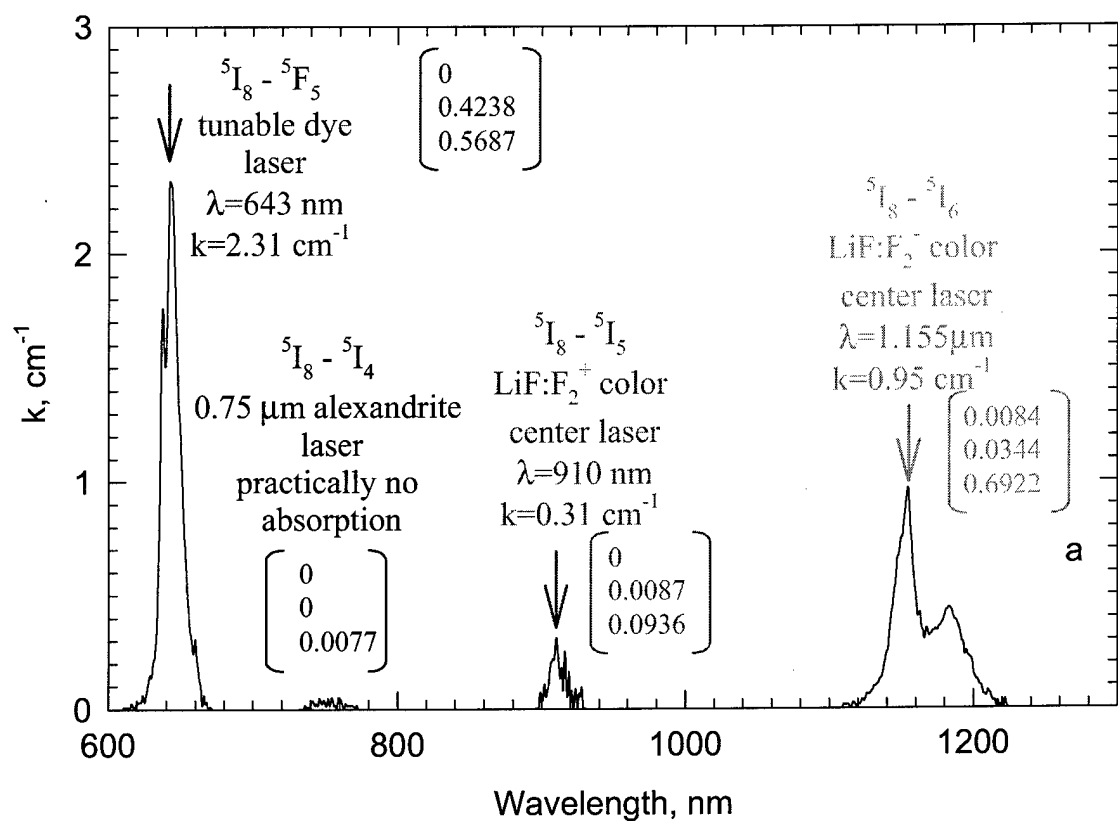


Fig. 3.2 The absorption spectra of the  $\text{CaF}_2:\text{HoF}_3$  (4 mol.%) crystal

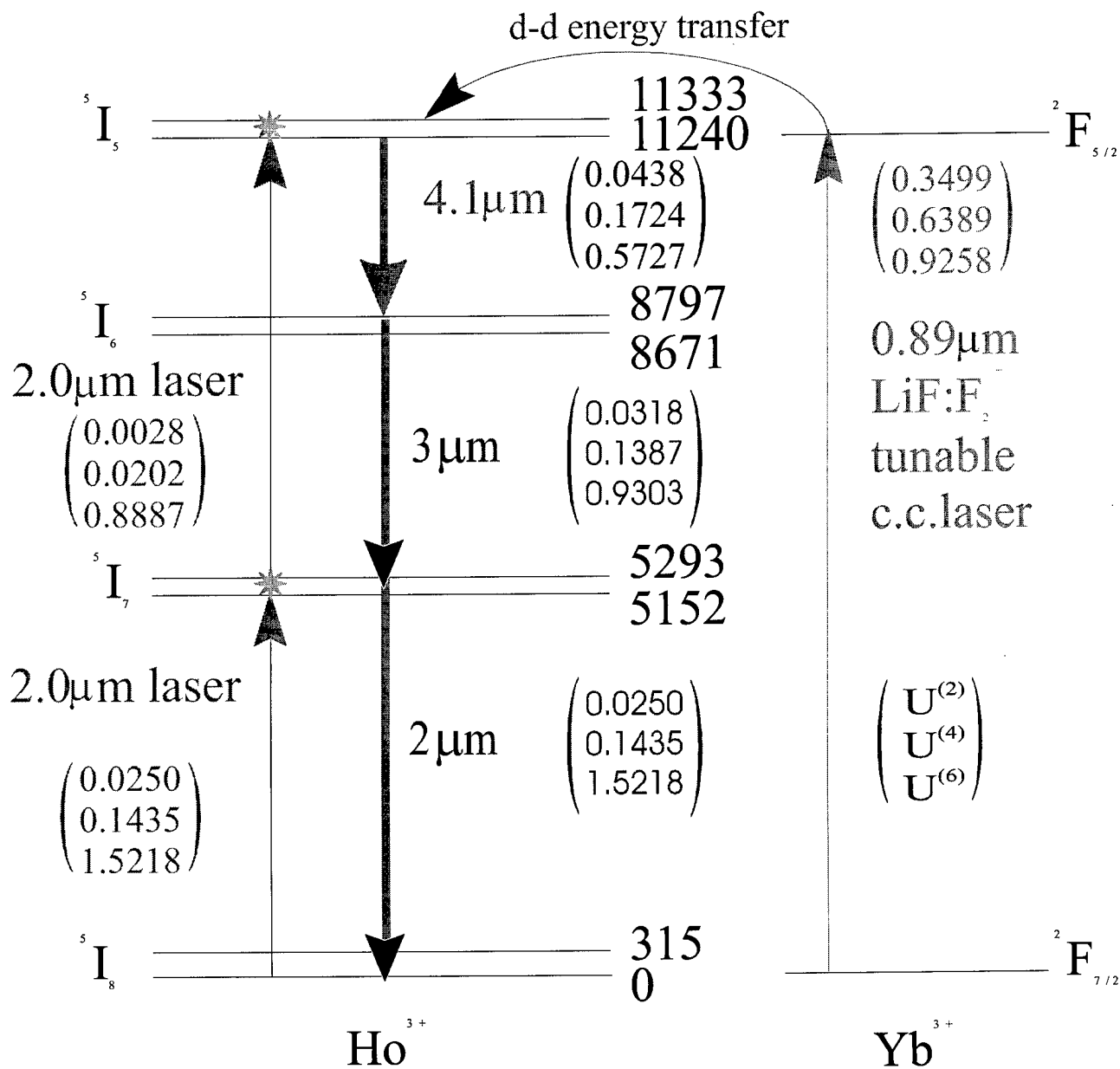


Fig. 3.3 Two step excitation and sensitization of holmium mid-IR transitions

## **Chapter 4**

### **Energy levels scheme of thulium ion.**

Several mid-IR laser schemes could be realized on the base of  $\text{Tm}^{3+}$  ion. One of them is the 5.2  $\mu\text{m}$  lasing at the  ${}^3\text{F}_2; {}^3\text{F}_3 \rightarrow {}^3\text{H}_4$  transition under direct 0.69  $\mu\text{m}$  ruby laser pumping (Fig. 4.1). The line strength of the  ${}^3\text{H}_6 \rightarrow {}^3\text{F}_3; {}^3\text{F}_2$  absorption transition due to large  $U(4)=0.3163$  and very large  $U(6)=0.8411$  is expected to be rather high. And the 5.2  $\mu\text{m}$  transition itself has rather large matrix elements  $U(4)=0.3535$  and  $U(6)=0.2850$ . Similar situation holds for the 2.3  $\mu\text{m}$   ${}^3\text{H}_4 \rightarrow {}^3\text{H}_5$  transition under tunable 0.77  $\mu\text{m}$  Ti- sapphire direct laser pumping and for the 4.3  $\mu\text{m}$   ${}^3\text{H}_5 \rightarrow {}^3\text{F}_4$  transition under 1.21  $\mu\text{m}$  direct pumping by tunable  $\text{LiF}: \text{F}_2^-$  color center laser. The measured excited states lifetimes  $\tau$  in the  $\text{LiYF}_4:\text{Tm}^{3+}$  crystal at 300K are presented in Fig. 4.1. Fig. 4.2 presents the absorption spectrum in the spectral range of above mentioned transitions. The largest absorption coefficient ( $k_{\text{max}}=2 \text{ cm}^{-1}$ ) was found at 676 nm of the  ${}^3\text{H}_6 \rightarrow {}^3\text{F}_3; {}^3\text{F}_2$  transition. Here tunable dye laser can be used for laser pumping. For 0.69  $\mu\text{m}$  of ruby laser  $k=0.47 \text{ cm}^{-1}$  is 4 times lower than for dye laser. Also, rather small value of  $k=1.13 \text{ cm}^{-1}$  was found at 0.77  $\mu\text{m}$  of Ti-Sapphire laser pumping at the  ${}^3\text{H}_6 \rightarrow {}^3\text{H}_4$  and at 1.21  $\mu\text{m}$  ( $k=1.01 \text{ cm}^{-1}$ ) of  $\text{LiF}_2:\text{F}_2^-$  tunable color center (c.c) laser pumping at the  ${}^3\text{H}_6 \rightarrow {}^3\text{H}_5$  transition in spite of large matrix elements  $U(4)$  and  $U(6)$ . The possible reason is small  $\Omega_4$  and  $\Omega_6$  in  $\text{CaF}_2$ . Hence, the solid state hosts with large  $\Omega(4)$  and  $\Omega(6)$  are preferred to realize these laser schemes of  $\text{Tm}^{3+}$ . The efficiency of the thulium 4.3  $\mu\text{m}$  laser scheme can be increased by two step sensitization with the  $\text{Yb}^{3+}$  and  $\text{Ho}^{3+}$  ion due to larger matrix elements  $U(k)$  for the  ${}^2\text{F}_{7/2} \rightarrow {}^2\text{F}_{5/2}$  transition of  $\text{Yb}^{3+}$  (Fig. 4.3) in comparison with the  ${}^3\text{H}_6 \rightarrow {}^3\text{H}_5$  transition of  $\text{Tm}^{3+}$  (Fig. 4.1). The  ${}^2\text{F}_{5/2}$  state can be excited by tunable  $\text{LiF}: \text{F}_2^+$  color center laser with consequent dipole – dipole energy transfer to the  ${}^5\text{I}_6$  state of  $\text{Ho}^{3+}$  and then to the  ${}^3\text{H}_5$  state of  $\text{Tm}^{3+}$ . The absorption spectrum of  $\text{Yb}^{3+}$  in  $\text{CaF}_2:\text{YbF}_3$  (4.5 mol.%) is

presented in Fig. 4.4. The largest absorption coefficient ( $k_{\max}=4.9 \text{ cm}^{-1}$ ) was found at the 978 nm of the  $^2F_{7/2} \rightarrow ^2F_{5/2}$  transition. It is 4.7 times larger than for the  $^3H_6 \rightarrow ^3H_5$  1.21  $\mu\text{m}$  transition of  $\text{Tm}^{3+}$  ion in the  $\text{CaF}_2:\text{TmF}_3$  (4 mol.%) crystal ( $k= 1.04 \text{ cm}^{-1}$ ). Also, 1.15  $\mu\text{m}$  of  $\text{LiF}:\text{F}_2^-$  color center laser pumping directly into the  $^5I_6$  state of  $\text{Ho}^{3+}$  can be used. But the line strength of respective electro- dipole absorption transition is less than in  $\text{Yb}^{3+}$ . Holmium ion will help to increase the rate of the depletion of the  $^3F_4$  low laser level of thulium due to energy transfer to the  $^5I_7$  state of  $\text{Ho}^{3+}$ . All the transitions participated in the nonradiative energy transfer processes have very large matrix elements  $U(6)$  and large matrix elements  $U(4)$ . Again we should select solid state hosts with the intensity parameters  $\Omega(4)$  and  $\Omega(6)$  being as large as possible.



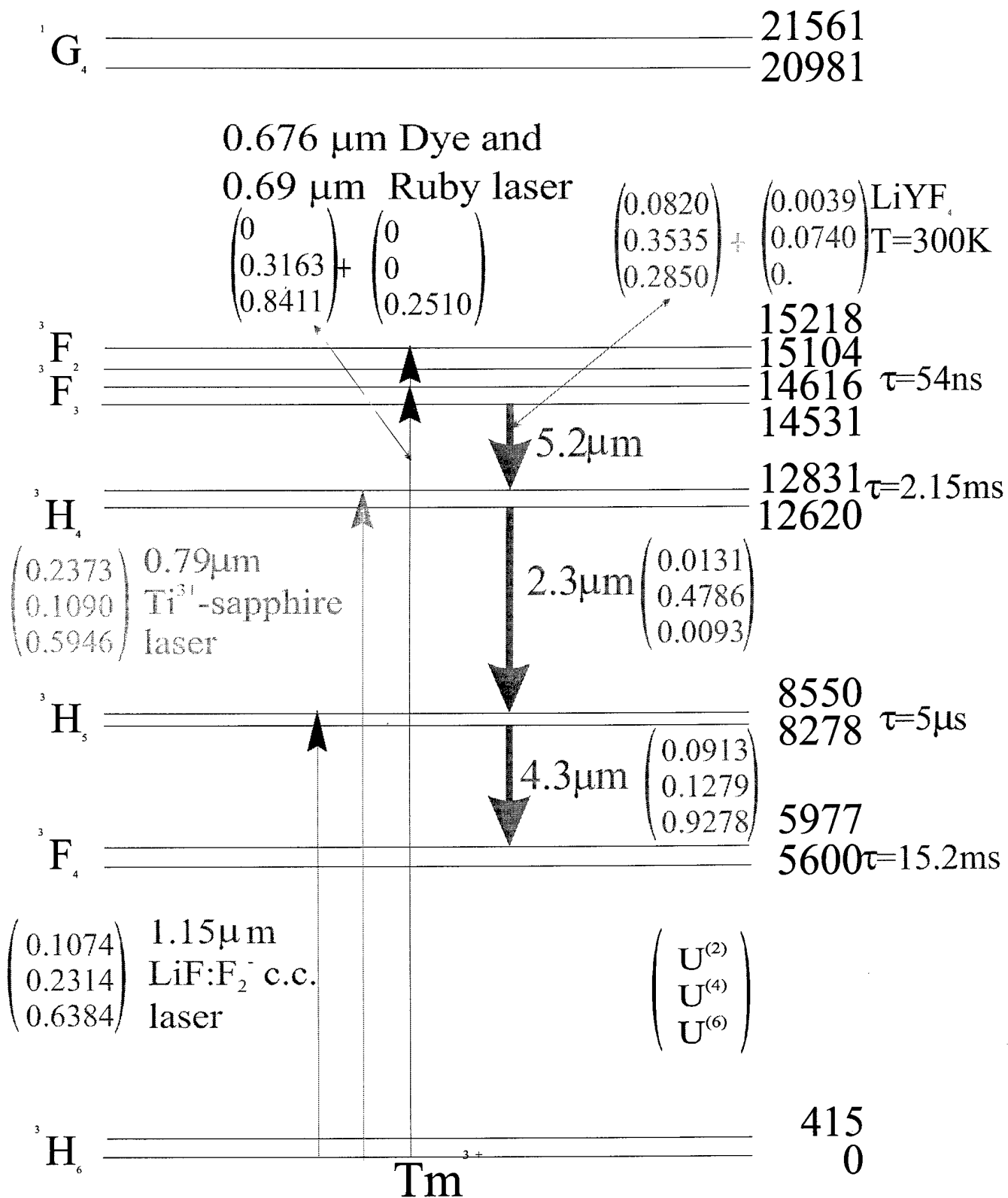


Fig. 4.1 Direct excitation of thulium mid-IR transitions

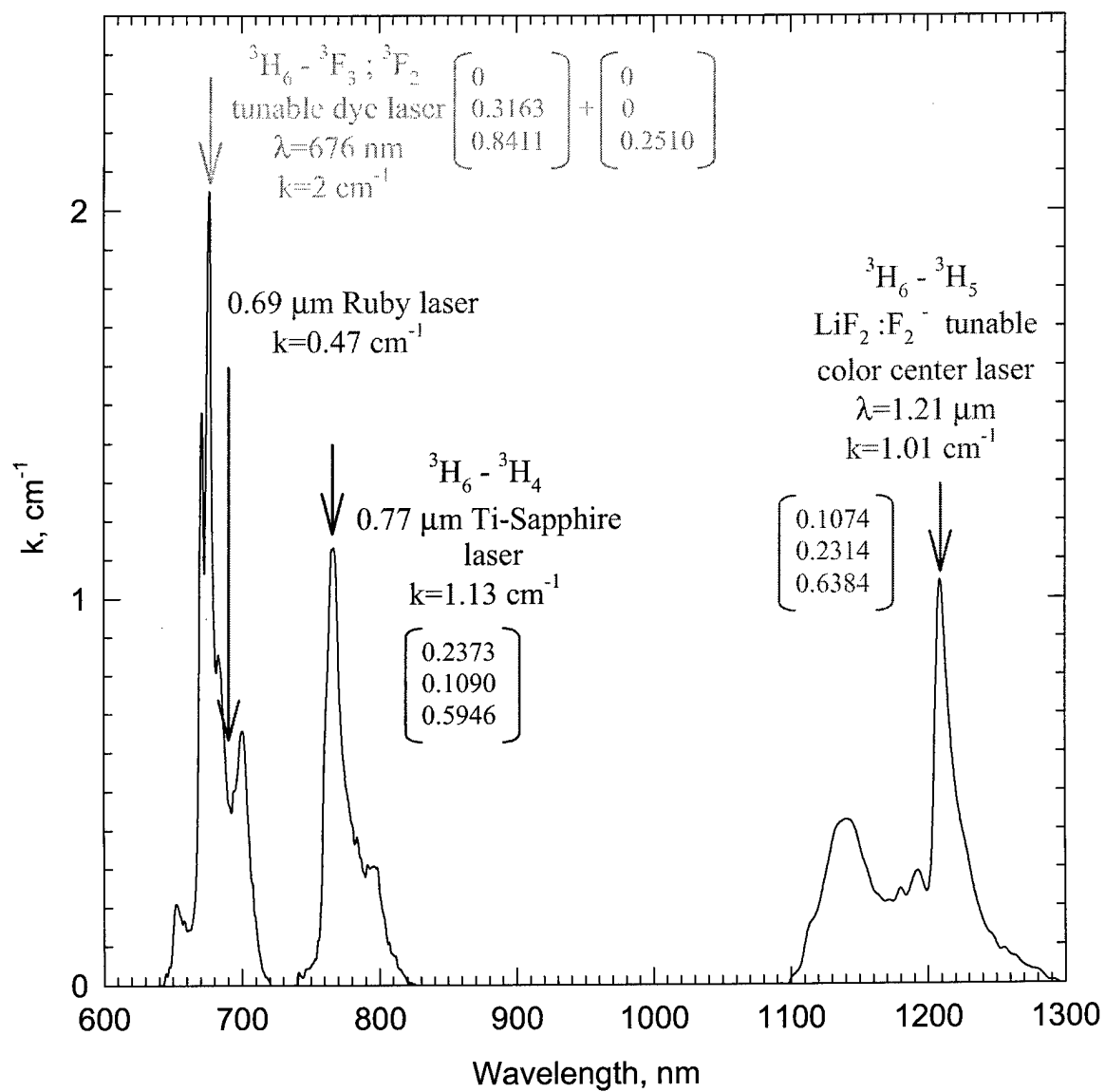


Fig. 4.2 The absorption spectra of the  $\text{CaF}_2:\text{TmF}_3$  (4 mol.%) crystal.

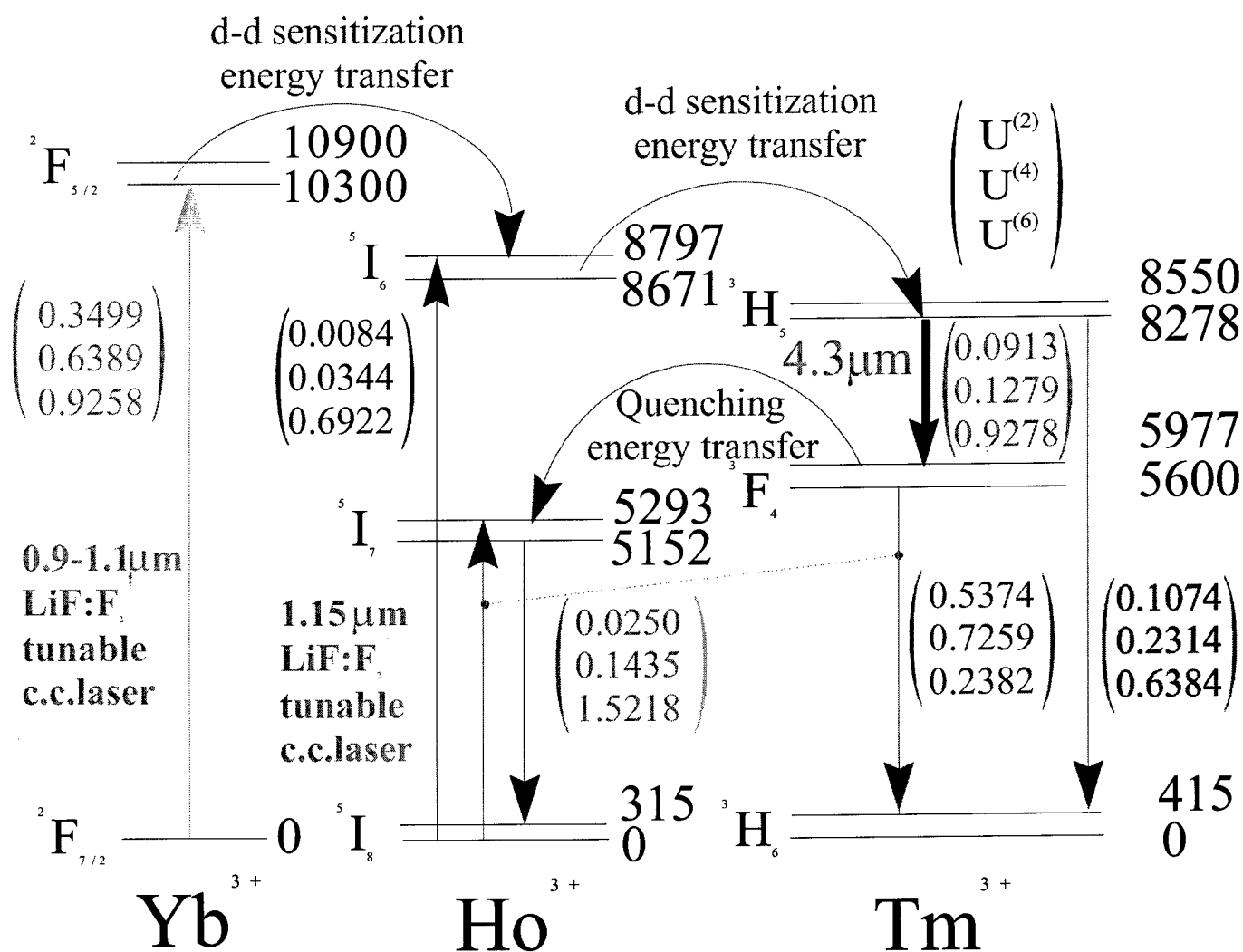


Fig. 4.3 Sensitization of thulium 4.3 μm transition.

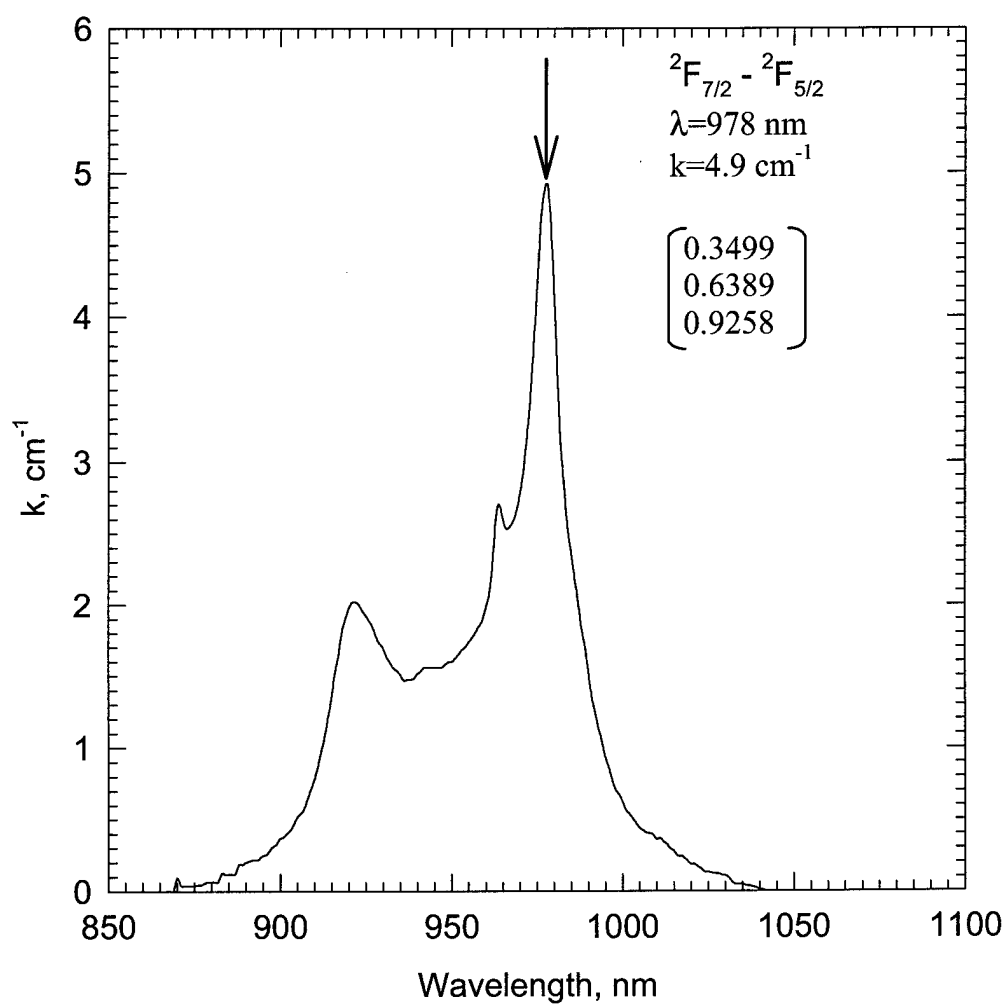


Fig. 4.4 The absorption spectra of the  $\text{CaF}_2:\text{YbF}_3$  (4.5 mol.%) crystal.

## **Chapter 5**

### **Energy levels scheme analysis of $\text{Pr}^{3+}$ ion.**

Praseodimium energy level scheme for population inversion creation at the  $^3\text{F}_4$ ;  $^3\text{F}_3$  initial level with the following 5.2 or 7.2  $\mu\text{m}$  laser radiation after cooperative excitation ( $^3\text{H}_6 \rightarrow ^3\text{H}_5$ ;  $^3\text{H}_6 \rightarrow ^3\text{F}_3$ ;  $^3\text{F}_4$ ) in concentrated samples under 2  $\mu\text{m}$  thulium or holmium laser pumping is presented in Fig. 5.1. Sequential excitation of two  $\text{Pr}^{3+}$  ions into the  $^3\text{H}_6$  state is followed by up-conversion due to sequential sensitization from one excited ion to another excited ion with the increasing of excitation energy. As the result of up-conversion one of the excited praseodimium ions decreases its excitation energy while the another increases its excitation energy and goes into the  $^3\text{F}_3$ ;  $^3\text{F}_4$  mixed excited state which can be used as initial laser level for mid IR oscillation. Here 5.2  $\mu\text{m}$  lasing at the  $^3\text{F}_4$ ;  $^3\text{F}_3 \rightarrow ^3\text{H}_6$  or 7.2  $\mu\text{m}$  at the  $^3\text{F}_4$ ;  $^3\text{F}_3 \rightarrow ^3\text{F}_2$  transition is expected. Analysis of 5.2  $\mu\text{m}$  generation scheme shows that the  $^3\text{H}_4 \rightarrow ^3\text{F}_2$  pumping transition has the largest matrix elements  $U^{(2)}$ . For the transitions participated in the up-conversion as well as for 5.2  $\mu\text{m}$  mid-IR laser transition and for the  $^3\text{H}_6 \rightarrow ^3\text{H}_5$  and  $^3\text{H}_5 \rightarrow ^3\text{H}_4$  5  $\mu\text{m}$  cascade laser transitions the situation is opposite. All these transitions have rather large  $U^{(6)}$  and  $U^{(4)}$  parameters and smaller  $U^{(2)}$ . Therefore, all three intensity parameters  $\Omega_k$  of the solid state matrix doped with praseodimium have to be large. Fortunately for the rare-earth ions with large ionic radius (the left side of the  $\text{Ln}^{3+}$  row) this condition can be fulfilled very easily. As example, possible candidates are presented in Table 5.1.

Table 5.1

Nd <sup>3+</sup> doped crystal matrix	$\Omega_2, 10^{-20} \text{ cm}^2$	$\Omega_4, 10^{-20} \text{ cm}^2$	$\Omega_6, 10^{-20} \text{ cm}^2$
Y <sub>2</sub> O <sub>3</sub>	46	28	20
LaF <sub>3</sub>	0.13	0.7	10
LaCl <sub>3</sub>	11.4	4.8	10.6

According to our previous study [1] the rare-earth ions with large ionic radius (Pr<sup>3+</sup>, Nd<sup>3+</sup>) possess increasing rate of multiphonon relaxation in comparison with the Er<sup>3+</sup>, Ho<sup>3+</sup> and Tm<sup>3+</sup> ions with small ionic radii. This requires the solid matrixes with short cut-off phonon frequencies such as sulfides, chlorides and bromides to bridge the energy gap of mid-IR laser transition by the larger number of phonons to decrease multiphonon relaxation rate. Because of this non-hydroscopic La<sub>2</sub>S<sub>3</sub> crystals doped with Nd<sup>3+</sup> ions can be promising for mid-IR lasing.

Fig. 5.2 presents absorption spectra of the LaF<sub>3</sub>:PrF<sub>3</sub> (1 mol.%) crystal in the near-IR spectral region. It is seen that absorption coefficient at the peak (1.95  $\mu\text{m}$ ) of the <sup>3</sup>H<sub>4</sub>→<sup>3</sup>F<sub>2</sub> transition spectral line is approximately 3 times smaller ( $k=0.72 \text{ cm}^{-1}$ ) than that for the <sup>3</sup>H<sub>4</sub>→<sup>3</sup>F<sub>3</sub>; <sup>3</sup>F<sub>4</sub> 1.54  $\mu\text{m}$  absorption transition ( $k_{\text{max}}=2.03 \text{ cm}^{-1}$ ). Moreover, the wavelengths of 1.54  $\mu\text{m}$  erbium glass laser practically fits the peak of the spectral line. Hence, this laser can be used for direct pumping of the <sup>3</sup>H<sub>3</sub>; <sup>3</sup>F<sub>4</sub> initial laser level. As well as it can be used for pumping of erbium in codoped Er-Pr LaF<sub>3</sub> crystal where sensitization of praseodimium fluorescence by energy transfer from erbium can be used (Fig. 5.3). The pumping <sup>4</sup>I<sub>15/2</sub>→<sup>4</sup>I<sub>13/2</sub> erbium transition has large matrix element  $U^{(6)}$  but smaller  $U^{(2)}$  and  $U^{(4)}$  than the <sup>3</sup>H<sub>4</sub>→<sup>3</sup>F<sub>3</sub>; <sup>3</sup>F<sub>4</sub> praseodimium pumping transition. So, these two ways of pumping can be competitive.

All three schemes of pumping presented in Figs. 5.1 and 5.3 will be tested by us in different doped solid state matrixes. As far as we know the only successful result of praseodimium lasing in the mid-IR spectral range is 5.2  $\mu\text{m}$  and 7.2  $\mu\text{m}$  generation at the  $^3\text{F}_3 \rightarrow ^3\text{H}_6$  and the  $^3\text{F}_3 \rightarrow ^3\text{F}_2$  transitions, respectively, obtained in the  $\text{LaCl}_3:\text{Pr}^{3+}$  using an up-conversion pumping mechanism [2,3]. For 7.2  $\mu\text{m}$  lasing this was done in spite of very small matrix elements of laser transition ( $U^{(2)}=0.0210$ ;  $U^{(4)}=0.0509$ ;  $U^{(6)}=0$ ). The admixture of the  $^3\text{F}_4$  state to the  $^3\text{F}_3$  state does not improve situation significantly, because for the  $^3\text{F}_4 \rightarrow ^3\text{F}_2$  transition  $U^{(k)}$  parameters are also very small ( $U^{(2)}=0.0015$ ;  $U^{(4)}=0.0012$ ; and  $U^{(6)}=0.0897$ ). The possible reason of success is very large intensity parameters  $\Omega_k$  in this crystal (see Table 5.1) which determine the line strength  $S_{\text{ed}}$  of the  $^3\text{F}_4$ ;  $^3\text{F}_3 \rightarrow ^3\text{F}_2$  electro-dipole transition. In its turn small matrix elements  $U^{(k)}$  reduce significantly the by-pass by multiphonon transition and thus give the lasing to be occurred. For 5.2  $\mu\text{m}$  transition the situation is much better. The  $U^{(4)}=0.3182$  and  $U^{(6)}=0.8460$  parameters of the  $^3\text{F}_3 \rightarrow ^3\text{H}_6$  laser transition are very large and admixture of the  $^3\text{F}_4$  state to the  $^3\text{F}_3$  state may increase the  $U^{(2)}$  parameter (see Fig. 5.3).

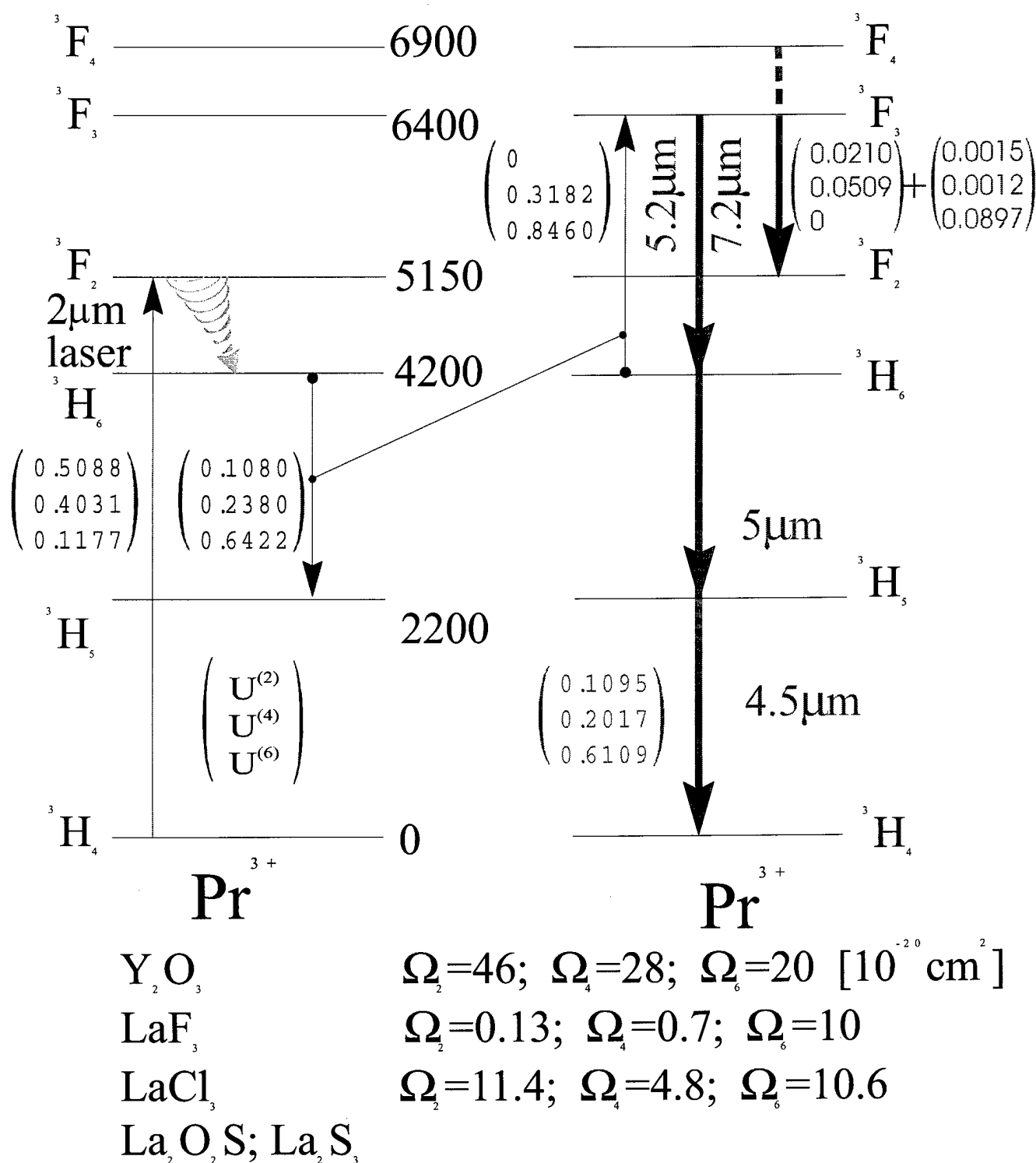


Fig. 5.1 Up-conversion pumping of praseodimium mid-IR transitions.



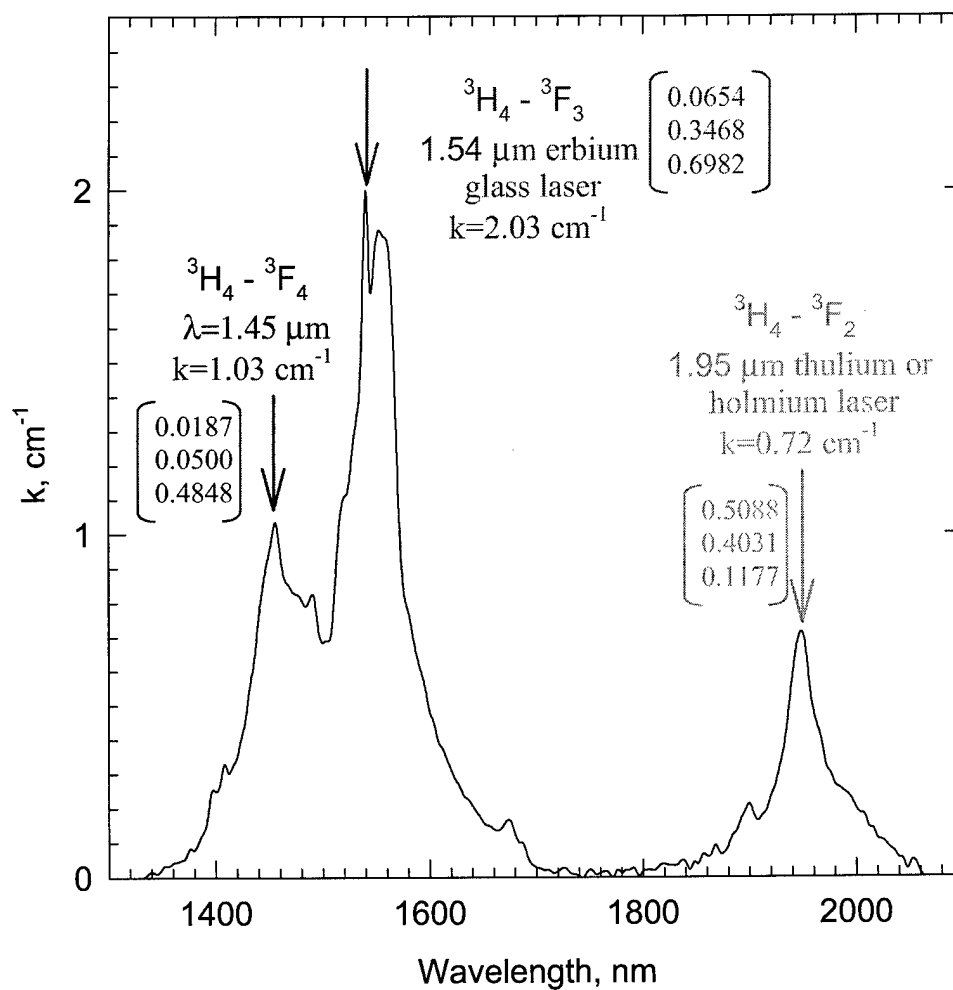


Fig. 5.2 The absorption spectra of the  $\text{LaF}_3:\text{PrF}_3$  (1 mol.%) crystal.

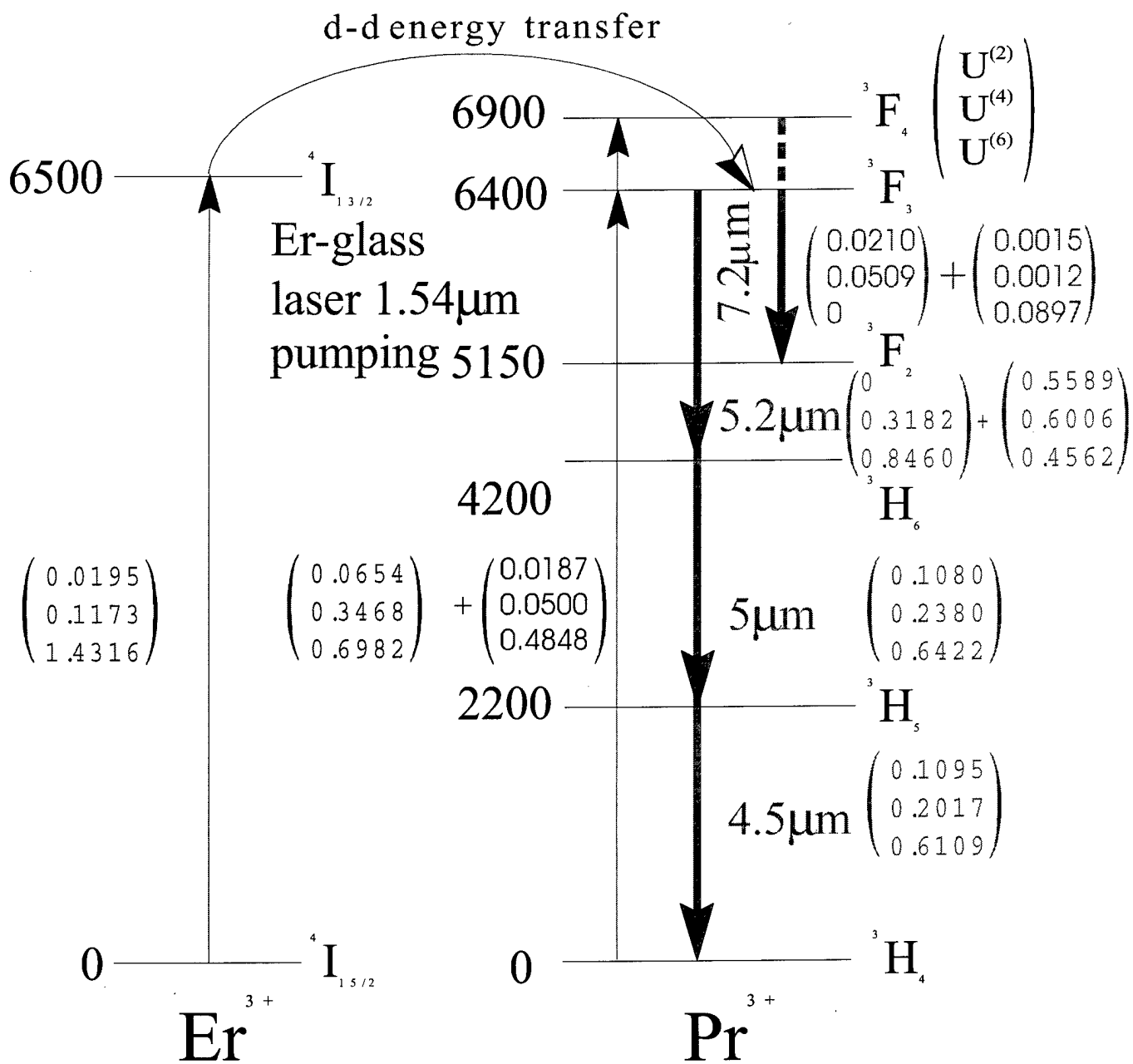


Fig. 5.3 Direct pumping and sensitization of praseodymium mid-IR transitions.

References:

1. Review: T.T.Basiev, Yu.V.Orlovskii, K.K.Pukhov, F.Auzel, Multiphonon relaxation of the energy of electronic excitation in optical crystals doped with rare-earth ions, *Laser Physics*, **7**, 1139 (1997)
2. S.R.Bowman, J.Ganem, B.S.Feldman, and A.W.Kueny, *IEEE J. Quantum Electron.*, **30**, 2925 (1994)
3. S.R.Bowman, L.B.Shaw, B.S.Feldman, and J.Ganem, *IEEE J. Quantum Electron.*, **32**, 646 (1996)

## Chapter 6

### Energy levels scheme of the neodymium ions.

Several electronic transitions of the  $\text{Nd}^{3+}$  ion can be tested for the 4-5  $\mu\text{m}$  lasing. These are  ${}^4\text{I}_{15/2} \rightarrow {}^4\text{I}_{13/2}$ ;  ${}^4\text{I}_{13/2} \rightarrow {}^4\text{I}_{11/2}$  and  ${}^4\text{I}_{11/2} \rightarrow {}^4\text{I}_{9/2}$  (Fig. 6.1). As 1.54  $\mu\text{m}$  erbium glass laser does not match well the energy of the  ${}^4\text{I}_{15/2}$  state (see, for example, Fig. 6.2 for the absorption spectrum in  $\text{BaF}_2:\text{NdF}_3$  (2.5 mol.%)) codoping by erbium can be performed. Moreover, the matrix elements  $U^{(k)}$  for the  ${}^4\text{I}_{9/2} \rightarrow {}^4\text{I}_{15/2}$  transition of  $\text{Nd}^{3+}$  are very small ( $U^{(2)}=0$ ;  $U^{(4)}=0.0001$ ;  $U^{(6)}=0.0453$ ). This is reflected in the absorption spectrum. Even at 2.5 mol.% of  $\text{NdF}_3$  in the  $\text{BaF}_2$  crystal the absorption coefficient at the maximum of spectral line is very small ( $k_{\text{max}}=0.08 \text{ cm}^{-1}$ ). However, for the  ${}^4\text{I}_{9/2} \rightarrow {}^4\text{I}_{15/2}$  1.54  $\mu\text{m}$  transition of  $\text{Nd}^{3+}$  ion in the  $\text{LaF}_3:\text{NdF}_3$  (4 mol.%) crystal the absorption coefficient ( $k=0.2 \text{ cm}^{-1}$ ) (Fig. 6.3) is 10 times larger than that in the  $\text{BaF}_2:\text{NdF}_3$  (2.5 mol.%) crystal ( $k=0.02 \text{ cm}^{-1}$ ). Sensitization of the excitation due to energy transfer from the  ${}^4\text{I}_{13/2}$  state of erbium to the  ${}^4\text{I}_{15/2}$  state of neodymium considerably increases the efficiency of pumping. For the erbium  ${}^4\text{I}_{15/2} \rightarrow {}^4\text{I}_{13/2}$  pumping transition the  $U^{(k)}$  parameters are much larger ( $U^{(2)}=0.0195$ ;  $U^{(4)}=0.1173$  and  $U^{(6)}=1.4316$ ) than for the  ${}^4\text{I}_{9/2} \rightarrow {}^4\text{I}_{15/2}$  one of  $\text{Nd}^{3+}$ . This is reflected in the absorption spectrum of the  $\text{BaF}_2:\text{ErF}_3$  (5 mol.%) crystal ( $k(1.54\mu\text{m}) = 4 \text{ cm}^{-1}$ ) (Fig. 6.4). Large  $U^{(6)}$  parameter for erbium pumping transition fits well with large  $U^{(6)}$  for all cascade self-terminated laser transitions (Fig. 6.1). This requires neodymium doped crystals and glasses with large intensity parameters  $\Omega_6$ . Possible candidates are  $\text{CdF}_2$ ;  $\text{BaF}_2:\text{LuF}_3$  and  $\text{PbF}_2$  with  $\Omega_6 > 4 \times 10^{-20} \text{ cm}^2$ . Because of the increasing rate of multiphonon relaxation for the  $\text{Nd}^{3+}$  ion crystal hosts with short phonon spectra like sulfides and chlorides are preferred.

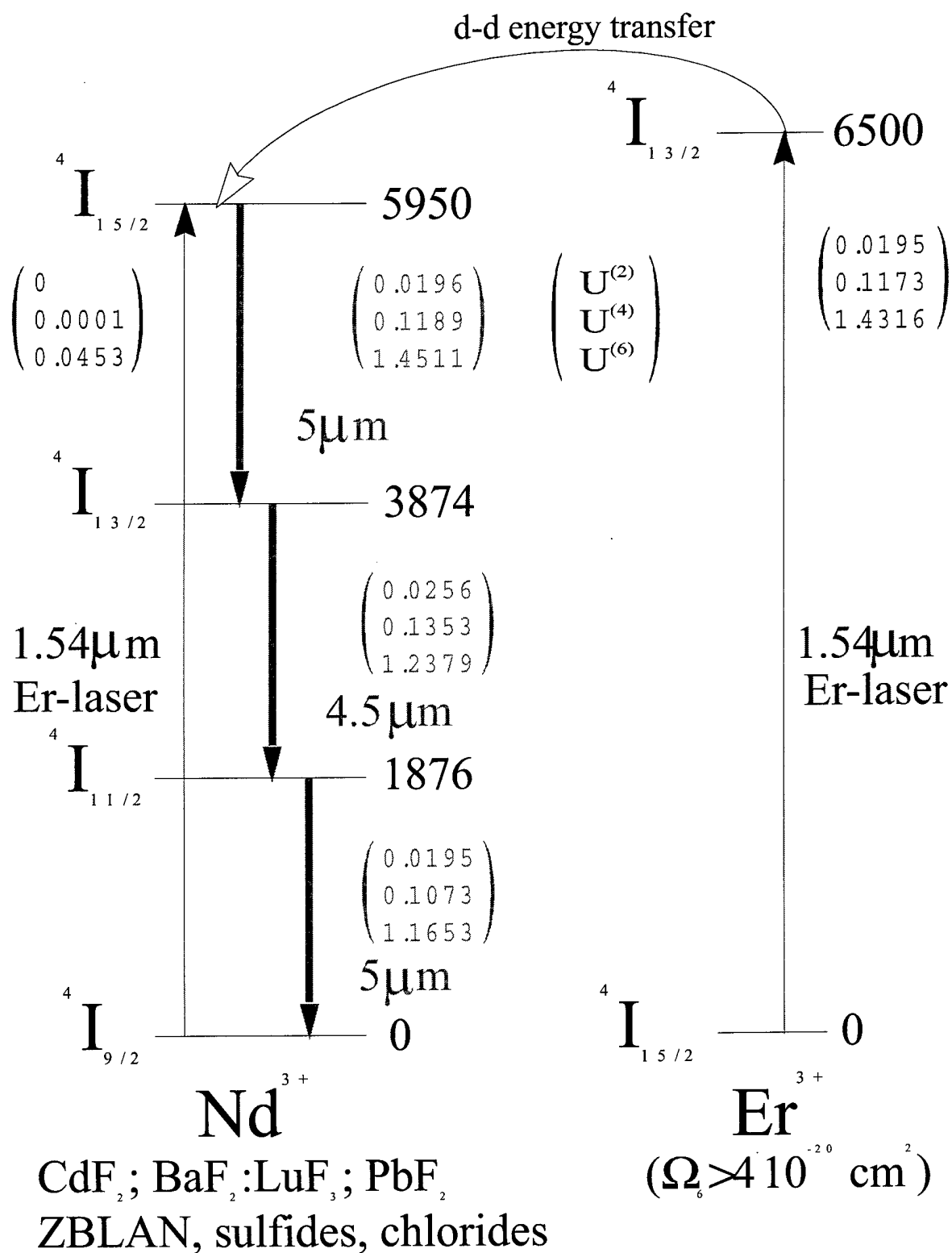


Fig. 6.1 Direct excitation and sensitization of neodymium mid-IR laser transitions.

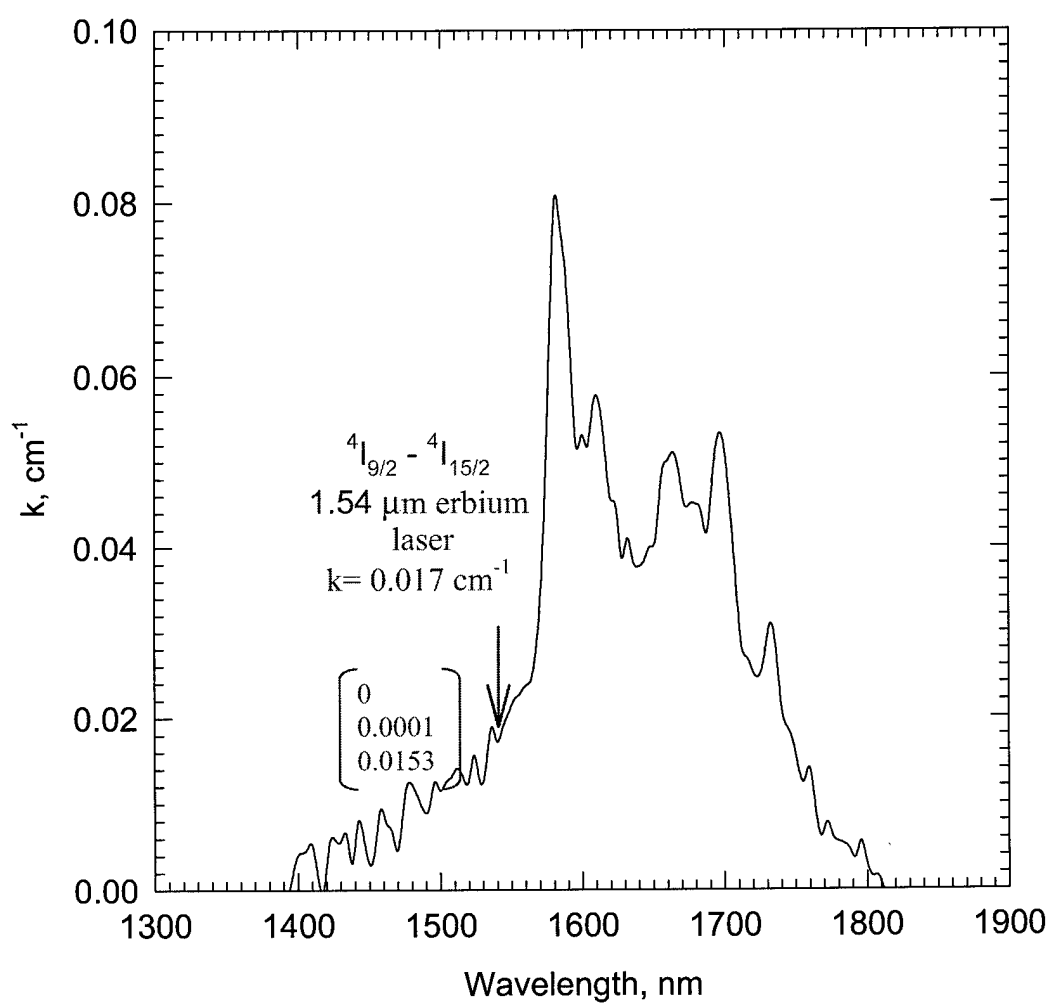


Fig. 6.2 The absorption spectra of the  $\text{BaF}_2:\text{NdF}_3$  (2.5 mol.%) crystal.

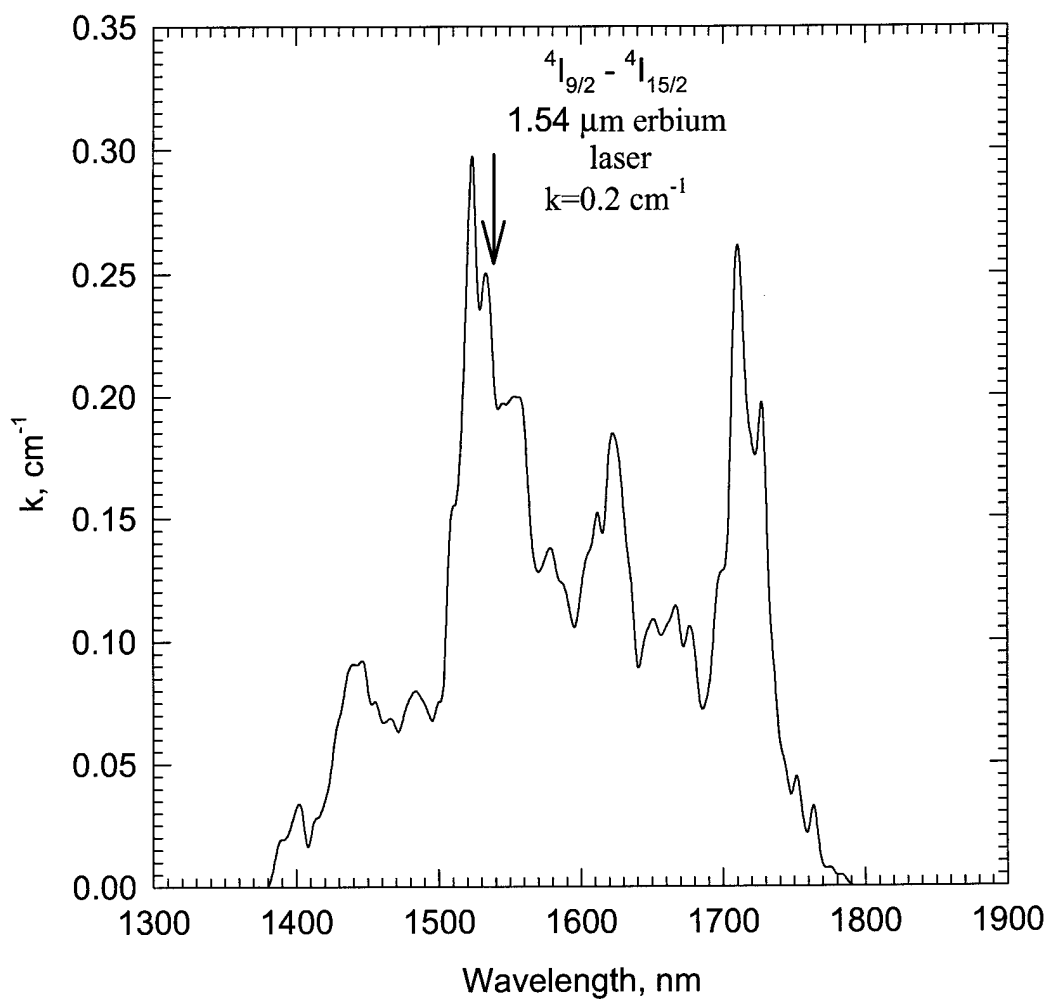


Fig. 6.3 The absorption spectra of the  $\text{LaF}_3:\text{NdF}_3$  (4 mol.%) crystal.

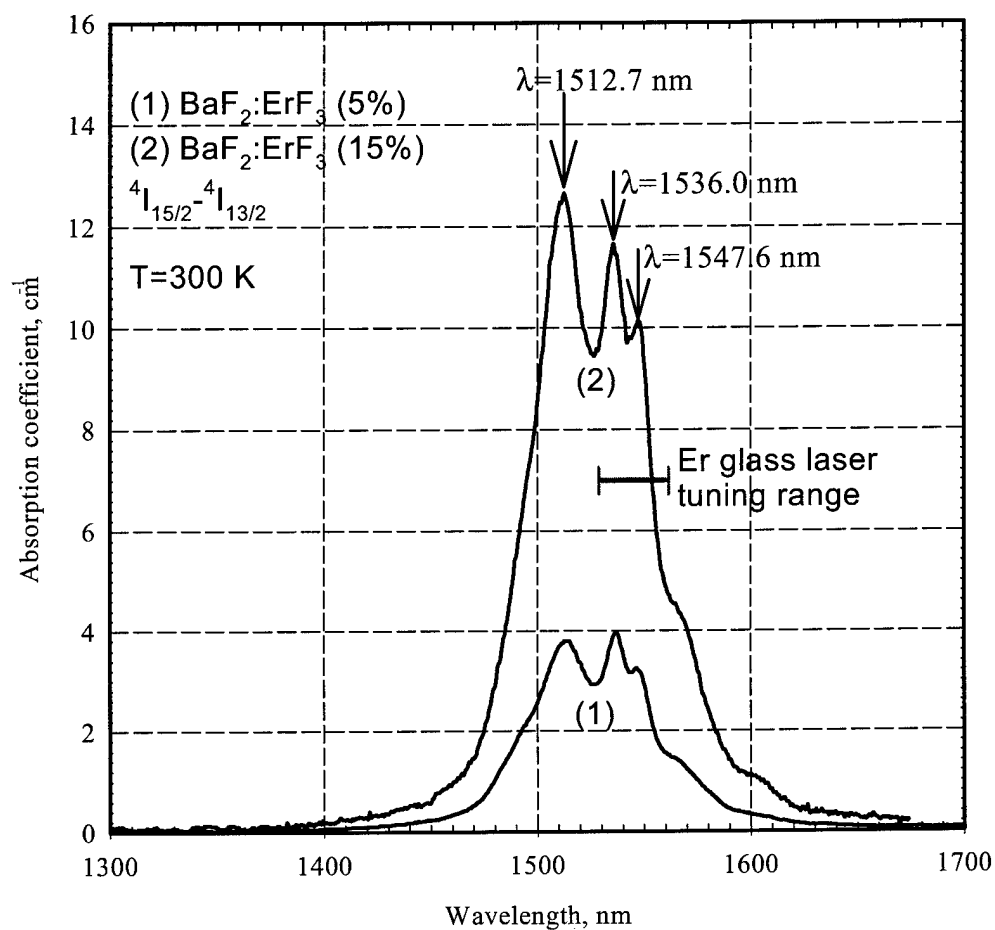


Fig. 6.4 Absorption spectra of  $\text{BaF}_2:\text{ErF}_3$ .



## **Chapter 7**

### **Nonradiative energy transfer and sensitization in fluorides, co-doped with $\text{Er}^{3+}$ - $\text{Ce}^{3+}$ and $\text{Nd}^{3+}$ - $\text{Ce}^{3+}$ with respect to 4-5 $\mu\text{m}$ laser transitions in $\text{Ce}^{3+}$ ions.**

Among the rare-earth ions having transitions suitable for obtaining oscillations within 4-5  $\mu\text{m}$  range, cerium ion can be mentioned. Its  $^2\text{F}_{7/2}$ - $^2\text{F}_{5/2}$  transition matches well the desired wavelength region, though its application is strongly limited by the absence of upper lying levels suitable for optical pumping. This drawback can be overcome by using sensitization by other rare-earth ion which can be easily optically pumped through higher-lying levels and can efficiently transfer energy to  $\text{Ce}^{3+}$  ion for further lasing. Here  $\text{Er} \rightarrow \text{Ce}$ ,  $\text{Nd} \rightarrow \text{Ce}$  and  $\text{Tm} \rightarrow \text{Ce}$  sensitization schemes were investigated in  $\text{La}_{1-x}\text{Ce}_x\text{F}_3$  solid solutions.

The  $\text{La}_{1-x}\text{Ce}_x\text{F}_3$  solid solutions with different amount of cerium ions from 0 to 100% (concentration  $x=0-1$ ) doped with low concentration of neodymium, thulium and erbium were studied. The crystal-chemical properties of  $\text{Ce}^{3+}$  ion are known to be most similar for that of  $\text{La}^{3+}$  ion and allow up to 100% substitution of the latter without noticeable distortion of the crystal lattice structure and changes of the activator ions optical properties.

$\text{La}_{1-x}\text{Ce}_x\text{F}_3:\text{Nd}$  and  $\text{La}_{1-x}\text{Ce}_x\text{F}_3:\text{Er}$  crystals were synthesized using Bridgeman technique in the fluorinating atmosphere. The dopant ions concentration was 0.3 at. % for  $\text{Nd}^{3+}$ , 1 at. % for  $\text{Er}^{3+}$  and 0.5 at. % for  $\text{Tm}^{3+}$  ions. Donor ions were excited by the second harmonics of the Q-switched GGG: $\text{Nd}^{3+}$  laser or by the nanosecond pulses of tunable Ti-sapphire laser. The donor fluorescence was dispersed by monochromator and registered by photomultiplier within 0.8-1  $\mu\text{m}$  spectral range or by Ge-photodiode within 1.5-1.6  $\mu\text{m}$  range. The decay curves of  $\text{Nd}^{3+}$  and  $\text{Er}^{3+}$  ions were measured by the digital oscilloscope TDS-380, connected to the PC.

Due to close values of  $\text{La}^{3+}$  and  $\text{Ce}^{3+}$  ion radius and  $\text{LaF}_3$  and  $\text{CeF}_3$  lattice constants the energy diagrams are practically unchanged when  $x$  is varied.

Comparison of the single cerium absorption transition energy with that for fluorescence transitions of neodymium, erbium and thulium shows that  $^4S_{3/2}$ - $^4F_{9/2}$ ,  $^4I_{9/2}$ - $^4I_{11/2}$  and  $^4I_{11/2}$ - $^4I_{13/2}$  transitions of erbium are in good resonance with the  $^2F_{5/2}$ - $^2F_{7/2}$  transition of cerium ion necessary for nonradiative donor-acceptor energy transfer. Regarding  $^4I_{13/2}$ - $^4I_{15/2}$  transition of erbium,  $^4F_{3/2}$ - $^4I_{15/2}$  transition of neodymium and  $^3H_4$ - $^3H_5$  transition of thulium no resonance with the cerium absorption can be observed. The short phonon spectrum of  $LaF_3$  and  $CeF_3$  lasting only  $400\text{ cm}^{-1}$  is also of great importance here.

The dependence of  $^4S_{3/2}$  level's decay lifetime  $\tau(^4S_{3/2})$  ( $Er^{3+}$  ion in  $La_{1-x}Ce_xF_3$

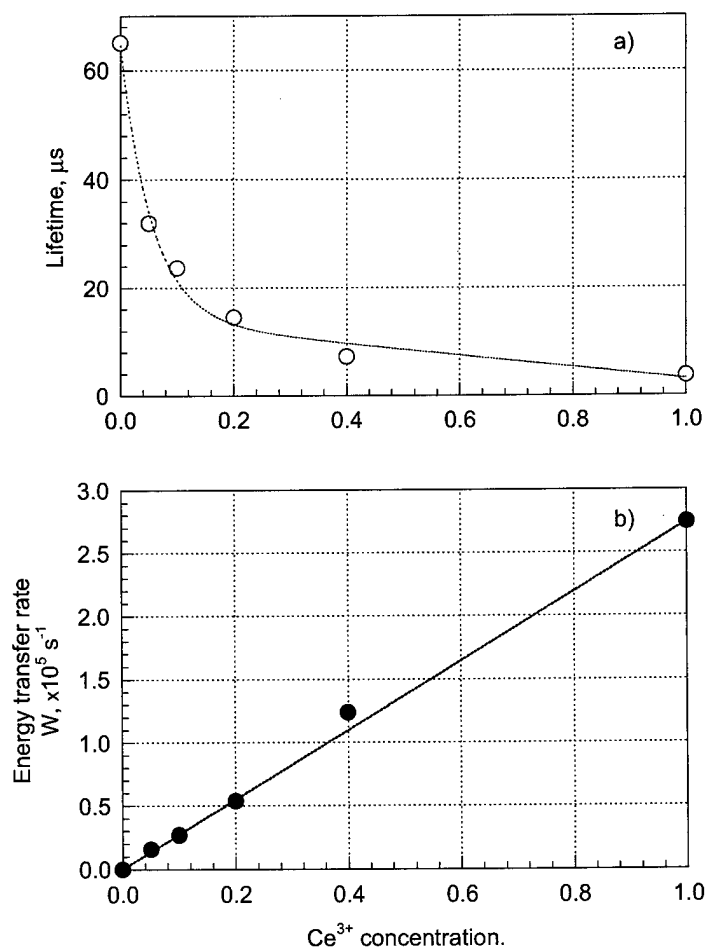


Fig. 7.1 Dependence of  $Er^{3+}$  ion  $^4S_{3/2}$  level lifetime (a) and energy transfer rate  $W_{Er-Ce}$  (b) in  $La_{1-x}Ce_xF_3$  solid solution on  $Ce^{3+}$  concentration (dots) and linear approximation of experimental data (solid line).

solid solution) measured at the initial ordered (or kinetic) decay stage on  $\text{Ce}^{3+}$  concentration ( $x$ ) is shown in Fig. 7.1(a). In Fig. 7.1(b) the corresponding values of quenching rate calculated as  $W_{\text{Er} \rightarrow \text{Ce}}(x) = 1/\tau(x) - 1/\tau(0)$  where  $\tau(0)$  is radiative lifetime, are presented. As can be seen from the Fig. 7.1(b) the experimental data are well fitted by straight line expected for kinetic limit (or direct ordered energy transfer) stage linear concentration dependence:  $W^m = a W^0 x$  [2], where  $a$  - coordination number of the neighboring cations, and  $W^0$  - the rate of elementary quenching interaction in the pair of neighboring ions at minimal distance  $R_{\text{min}}$ . As can be seen from Fig. 7.1(b) the value of the maximum quenching rate  $W_{\text{Er} \rightarrow \text{Ce}}^m(100\%)$  for pure cerium fluoride ( $\text{CeF}_3$ ) integrated over the whole cerium sublattice (which corresponds to situation when all the vacancies around the donor are occupied by acceptor ions) is  $W_{\text{Er} \rightarrow \text{Ce}}^m(100\%) = 270000 \text{ c}^{-1}$ . This value is the same order of magnitude as the value of direct  $\text{Nd} \rightarrow \text{Nd}$  self quenching rate in  $\text{NdF}_3$  crystal also with 100% acceptor concentration where the corresponding value was found to be  $W_{\text{Nd} \rightarrow \text{Nd}}^m(100\%) = 72000 \text{ c}^{-1}$  [7].

The measured decay curves of  $\text{Nd}^{3+} {}^4\text{F}_{3/2}$  metastable level in  $\text{La}_{1-x}\text{Ce}_x\text{F}_3$  solid solutions were single exponential. Open dots in Fig. 7.2(a) corresponds to the  ${}^4\text{F}_{3/2}$  metastable level lifetime dependence on cerium concentration  $x$ . Taking into account the constancy of radiative decay time, the observed lifetime decrease corresponds to concentration quenching. The values of nonradiative energy transfer rates calculated from the measured dependence  $\tau(x)$  as  $W_{\text{Nd} \rightarrow 2\text{Ce}} = 1/\tau(x) - 1/\tau(0)$ , are shown by closed dots in Fig. 7.2(b). Solid curve in Fig. 7.2(b) is the approximation of the experimental data by quadratic dependence of quenching rate on cerium ions concentration. The dashed line in the same Fig. corresponds to linear fit. If substitution of  $\text{La}^{3+}$  ions by  $\text{Ce}^{3+}$  ions in  $\text{LaF}_3$  lattice is an accidental process, then the chance to find a pair of cerium ions (formation of a cooperative acceptor ( $\text{Ce}_2$ )) in the nearest to the donor

coordination sphere should be proportional to the product of multiplication of the corresponding probabilities for a single ion and thus quadratic with respect to  $\text{Ce}^{3+}$  concentration. From the Fig. 7.2(b) sufficiently nonlinear, close to quadratic dependence, of the quenching rate  $W_{\text{Nd} \rightarrow 2\text{Ce}}$  on  $\text{Ce}^{3+}$  ions concentration up to 100% (pure  $\text{CeF}_3$ ) can be seen which disagree with the linear dependence characteristic for traditional mechanism of concentration quenching, observed in  $\text{Er} \rightarrow \text{Ce}$  or  $\text{Nd} \rightarrow \text{Nd}$  energy transfer process in highly concentrated  $\text{La}_{1-x}\text{Ce}_x\text{F}_3$  solid solutions.

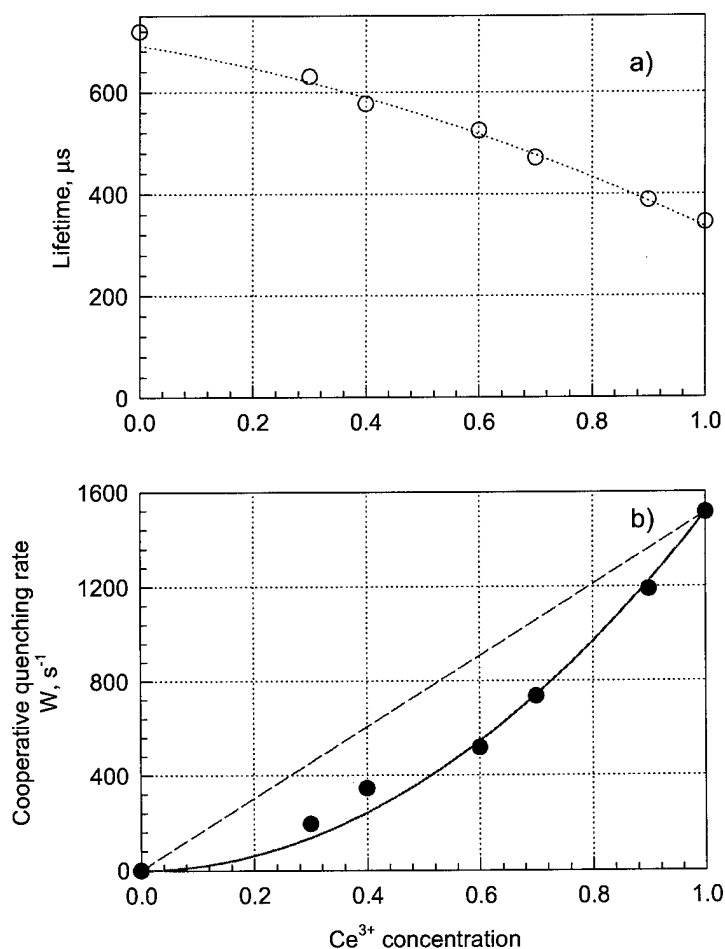


Fig. 7.2 Dependence of  $\text{Nd}^{3+}$  ion metastable  $^4\text{F}_{3/2}$  level lifetime (a) and cooperative quenching rate  $W_{\text{Nd} \rightarrow 2\text{Ce}}$  (b) on  $\text{Ce}^{3+}$  concentration  $x$  (dots) in  $\text{La}_{1-x}\text{Ce}_x\text{F}_3$  solid solution and linear (dashed line) and quadratic (solid line) approximation of experimental data.

The total rate of cooperative quenching  $W_{\text{Nd} \rightarrow 2\text{Ce}}^{\text{m}}(100\%)$  for pure cerium fluoride ( $\text{CeF}_3$ ) was determined to be  $W_{\text{Nd} \rightarrow 2\text{Ce}}^{\text{m}}(100\%) = 1570 \text{ c}^{-1}$ , which is orders of magnitude lower than that for traditional linear mechanism of energy transfer (see above).

Similar conditions for energy transfer from single  $\text{Tm}^{3+}$  to the pair of  $\text{Ce}^{3+}$  ions exist in  $\text{La}_{1-x}\text{Ce}_x\text{F}_3$  solid solution as the energy gap between  $^3\text{H}_4$  and  $^3\text{H}_5$  electronic levels is approximately twice of that for  $^2\text{F}_{7/2} - ^2\text{F}_{5/2}$  transition of  $\text{Ce}^{3+}$ . In Fig. 7.3(a) the measured  $^3\text{H}_4$  level lifetime  $\tau(^3\text{H}_4)$  dependence on  $\text{Ce}^{3+}$  concentration  $x$  is presented. The energy transfer rates calculated from the measured dependence  $\tau(x)$  as

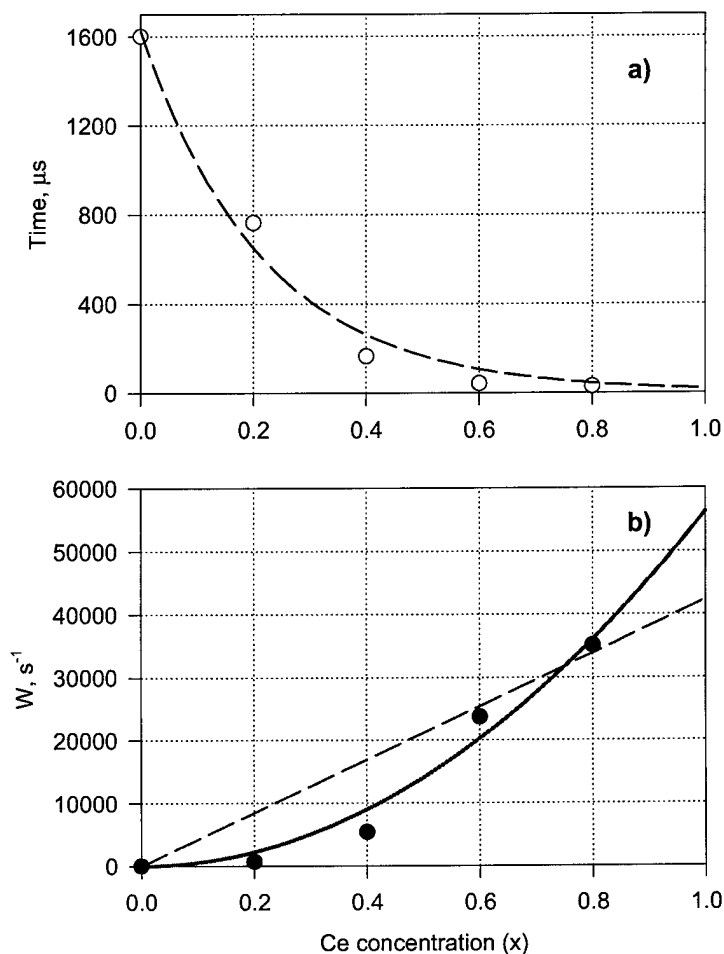


Fig. 7.3 Dependence of the  $\text{Tm}^{3+} ^3\text{H}_4$  level lifetime (a) and cooperative quenching rate  $W_{\text{Tm}-2\text{Ce}}$  (b) on  $\text{Ce}^{3+}$  concentration  $x$  (dots) in  $\text{La}_{1-x}\text{Ce}_x\text{F}_3$  solid solution and linear (dashed line (b)) and quadratic (solid line (b)) approximation of experimental data.

$W_{Nd \rightarrow 2Ce} = 1/\tau(x) - 1/\tau(0)$ , are shown by closed dots in Fig. 7.3(b). The solid curve in Fig. 7.3(b) corresponds to the quadratic approximation of the experimental data. As can be seen from the Fig. the values of the quenching rates in case of  $Tm \rightarrow 2Ce$  energy transfer process are sufficiently larger than in case of  $Nd \rightarrow 2Ce$  energy transfer.

Analogous situation of nonlinear concentration quenching was observed when  $^4I_{13/2}$  level of  $Er^{3+}$  ions in  $La_{1-x}Ce_xF_3$  solid solutions was excited. Here traditional linear energy transfer mechanism is also strictly forbidden and only cooperative

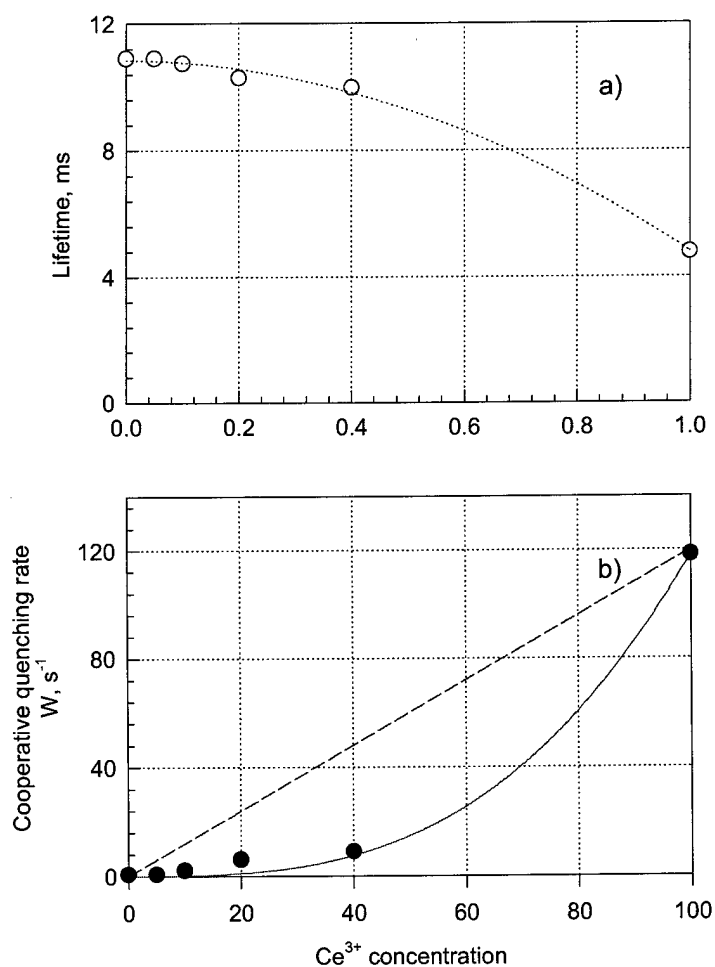


Fig.7.4 Dependence of  $Er^{3+}$  ion  $^4I_{13/2}$  level lifetime (a) and cooperative quenching rate  $W_{Er-3Ce}$  (b) in  $La_{1-x}Ce_xF_3$  solid solution on  $Ce^{3+}$  concentration x (dots) and linear (dashed line) and cubic (solid line) approximation of experimental data.

energy transfer can take place. Open dots in the Fig. 7.4(a) the dependence of  ${}^4I_{13/2}$  lifetime  $\tau({}^4I_{13/2})$  of erbium ions on cerium concentration is shown. The filled dots in Fig. 7.4(b) represent the corresponding values of cooperative quenching  $W_{Er \rightarrow 3Ce} = 1/\tau(x) - 1/\tau(0)$ . The probability of a triple acceptor ( $Ce_3$ ) should be just more nonlinear and proportional at least to cube of cerium concentration. The solid line in Fig. 7.4(b) is the approximation of the experimental data by cubic dependence of the quenching rate on  $Ce^{3+}$  ions concentration and dashed line is the linear approximation. As can be seen from Fig. 7.4(b) the cubic dependence is close to experimental data, which corresponds to the cooperative model of nonradiative energy transfer from single erbium ion simultaneously to three cerium ions, acting as a single cooperative acceptor ( $Ce_3$ ). The value of the total cooperative energy transfer rate  $W_{Er \rightarrow 3Ce}^m(100\%)$  in  $CeF_3$  crystal was determined to be  $W_{Er \rightarrow 3Ce}^m(100\%) = 120 \text{ s}^{-1}$ , which is the order of magnitude lower than that for cooperative quenching  $Nd \rightarrow 2Ce$  and orders of magnitude lower than energy transfer rate for traditional linear mechanism.

$Ce^{3+}$  luminescence in the 4-5  $\mu\text{m}$  spectral range was measured for  $La_{1-x}Ce_xF_3:Er^{3+}$  crystals. As was mentioned above highly efficient energy transfer from excited  $Er^{3+}$  ion to  $Ce^{3+}$  ions in  $La_{1-x}Ce_xF_3:Er^{3+}$  crystals can be observed. Thus the pumping scheme of  $Ce^{3+}$  ions via excitation of  $Er^{3+}$  ions can be applied to optically pump the upper level of  $Ce^{3+}$  ion. In these experiments the pumping  $Er^{3+}-Ce^{3+}$  scheme was realized to observe the 4-5  $\mu\text{m}$  fluorescence of  $Ce^{3+}$  ions when pumped by 802 nm laser diode into  ${}^4I_{9/2}$  level of  $Er^{3+}$  ion. The dopant ions concentration for the crystals investigated was 1 at. % for  $Er^{3+}$  and 5-40 at. % for  $Ce^{3+}$  ( $x=0.05-0.4$ ). The 4-5  $\mu\text{m}$  fluorescence of  $Ce^{3+}$  ions was excited by a CW ADLAS 1W laser diode via  $Er^{3+}$  ions absorption and further rapid energy transfer to  $Ce^{3+}$  ions. The fluorescent spectra of  $Ce^{3+}$  ions in the 4-5  $\mu\text{m}$  region were measured using double grating SDL

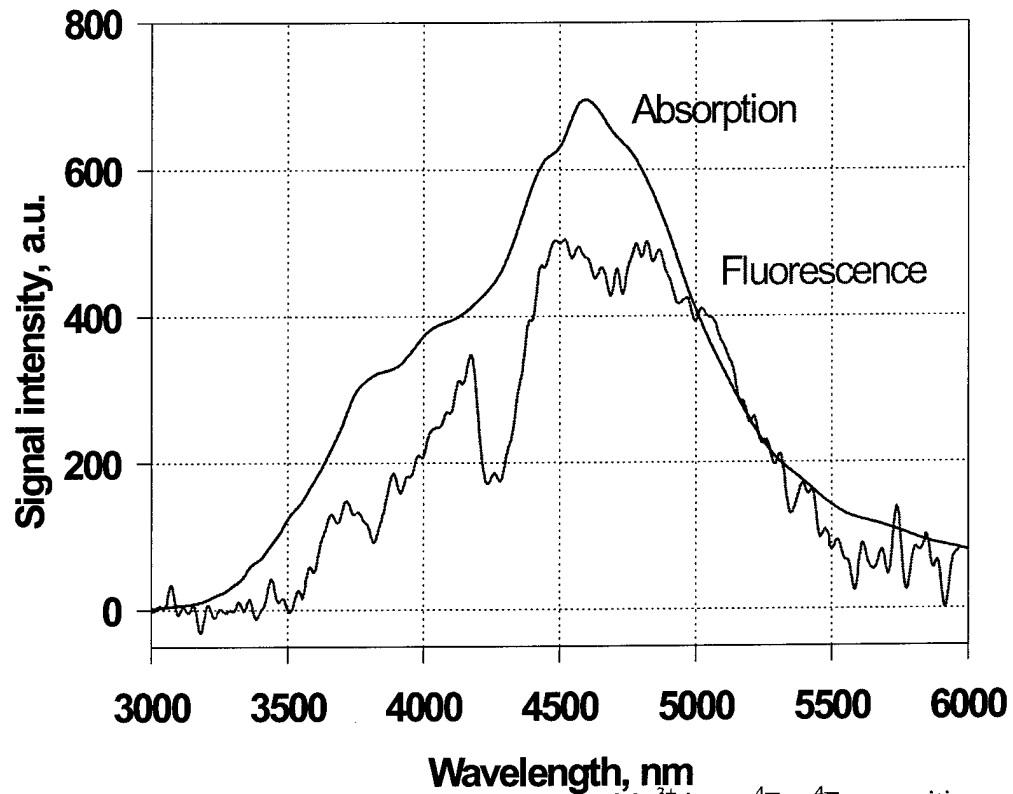


Fig. 7.5 Measured fluorescence and absorption spectra of  $\text{Ce}^{3+}$  ion at  $^4\text{F}_{5/2}$ - $^4\text{F}_{7/2}$  transition.

monochromator with 100 grooves/mm gratings. The slits width was 1.5-2 mm. To separate the 4-5  $\mu\text{m}$  fluorescence from intensive 1.5-3.0  $\mu\text{m}$  fluorescence observed in higher diffraction orders the special filter transparent in 3.5-6  $\mu\text{m}$  region was used. The fluorescent signal was detected by the Ge-Au liquid nitrogen cooled photodetector. To increase the signal to noise ratio the method of synchronous signal detection was applied. The detected signal was then recorded using an analog-digital converter and a PC. In Fig. 7.5 measured fluorescent spectrum of  $\text{Ce}^{3+}$  ions is shown. The measured absorption spectrum of  $\text{Ce}^{3+}$  ions at  $^4\text{F}_{5/2}$ - $^4\text{F}_{7/2}$  transition in  $\text{LaF}_3:\text{Ce}^{3+}$  crystal is also shown in the Fig. 7.5 for reference.



References to chapter 7

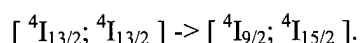
1. D.L. Dexter, J. Chem. Phys., 21, 836 (1953).
2. V.P. Sakun, Fiz. Tverdogo Tela, 14 (8), 2199 (1972).
3. O.K. Alimov, M. Kh. Ashurov, T.T. Basiev *et al.*, Proc. of GPI, ed. V.V. Osiko, 9, 67 (1987).
4. P.P. Feofilov, V.V. Ovsyankin, Appl. Optics, 6, 1828 (1967).
5. L.D. Livanova, I.G. Saitkulov, A.L. Stolov, Soviet Physics - Solid State, 11, 750 (1969).
6. F.W. Ostermayer, L.G. Van Uitert, Phys. Rev., B1, 4208 (1970).
7. T.T. Basiev, Yu. V. Orlovskii, Sov. JETP, 96, 1965 (1989).

## **Chapter 8**

### **Pumping sources and cavities arrangement.**

#### **8.1 Erbium glass lasers for spectroscopic studies and for laser pumping of erbium-doped crystalline lasers operating in 4 - 5 $\mu\text{m}$ range**

In this part of work the special attention is paid to potential possibilities of erbium-doped crystals as laser media operating at  $^4\text{I}_{9/2}$ - $^4\text{I}_{11/2}$  transition of  $\text{Er}^{3+}$  ion. One of the possible methods of  $^4\text{I}_{9/2}$  level population providing is optical pumping by means of  $\sim 1.5$  microns radiation into  $\text{Er}^{3+}$  absorption band corresponding to  $^4\text{I}_{15/2}$ - $^4\text{I}_{13/2}$  transition. In case of high Er concentration in laser matrix the efficient energy upconversion can be obtained due to non-radiative energy transfer between two excited erbium ions with the excitation energy summation according to following scheme:



It is obvious that this upconversion pumping scheme requires high-power pump laser oscillating  $\sim$  at 1.5 microns wavelength. Actually, flashlamp pumped erbium glass lasers can satisfy the required condition. In the frames of this work we used the large LMTRC experience in the designing of erbium glass lasers and in developing the methods of their radiation parameters control. One of our papers concerning controlling of radiation parameters of erbium glass lasers is [1]. In this paper an efficient method of forming microsecond-long giant pulse by FTIR-shutter (FTIR- frustrated total internal reflection) is described. One of our latest papers concerning this theme is [2] where an efficient passive saturable Q-switcher on the base of  $\text{MgAl}_2\text{O}_4:\text{Co}^{2+}$  spinel crystals is suggested.

Taking into consideration the peculiarities of the mentioned Q-switchers two erbium glass flashlamp pumped lasers have been assembled.

As an active element erbium glass rod 3 mm in diameter and 50 mm long was used. The erbium ions concentration in the glass was  $2 \times 10^{19} \text{ cm}^{-3}$ . The laser cavity was formed by plane (84%) and concave ( $R=1 \text{ m}$ , 100%) mirrors, the cavity length being 20 cm. The initial transmittance of the filter was chosen to be 90 – 92 %. The transverse mode selection properties of passive Q-switcher provided a stable generation of giant pulses with  $\text{TEM}_{00}$  mode structure without additional apertures in the laser cavity. The pulse duration was 60-80 ns and output energy value was 8-10 mJ.

In the previous part it has been found that the typical  $^4\text{I}_{9/2}$ -population decay is of microsecond time range. It is possible to achieve high-energy pump density in the new erbium-doped crystals, but in order to avoid optical damage of the crystals the long giant pulses produced by erbium glass laser should be used. For this purpose we have designed laser with the FTIR Q-switch.

100%, R=1 m

Er-glass laser rod, 6x80 mm

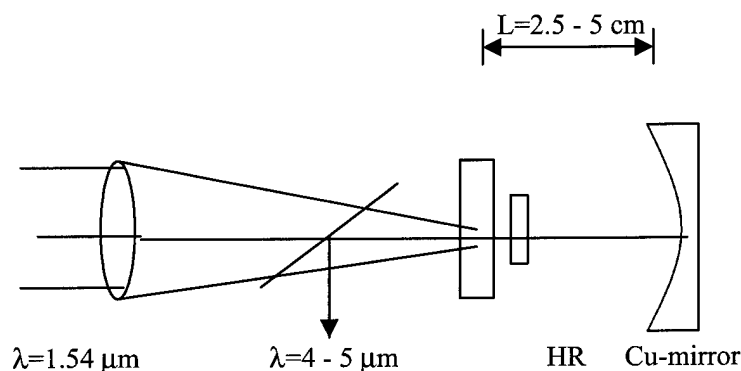
100%

FTIR-switch

100%

The FTIR-shutter has been operating at a low switching rate, voltage arising time was about one microsecond. This laser provided output energy up to 50 mJ and pulse duration about one microsecond.

To study the lasing properties of erbium-doped crystals we use longitudinal laser pump. The pump radiation from Q-switched erbium glass laser is focused into crystal sample by focusing lens with 30-mm focal length. The beam spot on the sample is varied in the range of 150 - 400 microns. The two types of laser cavity are used. One of them is a compact one ( $l=2-3$  mm) consisting of two high reflectivity plane dielectric mirrors. Another one is a stable cavity made of plane dielectric mirror and concave Cu-mirror with curvature radius 5 cm.



In both cavities the 1 mm crystal sample is placed close to plane mirror and is adjusted parallel to mirror surface. The luminescence and laser emission is registered by cooled InSb-photodiode. Emission wavelength is selected and controlled by the monochromator with the grating with 200 lines/mm. In this optical scheme we test few Er doped crystals as active laser elements for near IR oscillation. As a result we got lasing on  $2.8 \mu\text{m}$  but till now  $4-5 \mu\text{m}$  lasing was not attained. The reason for that probably low lasing crosssection of this transitions and relatively high losses in active crystals and laser mirrors.

## 8.2 Flash lamp pumped Tunable dye and Ti:Sapphire lasers for selective excitation of mid-infrared solid state lasers

Solid state tunable dye and Ti: sapphire lasers operating in the spectral range of 400-800 nm with the spectral width of 0.05-0.5 nm and output energy of 0.1-0.5J was developed and now under improvements.

Active media of the dye laser will be original dyes (complex modifications of rhodamine and oxazine) dissolved in the modified polymethyl methacrylate (PMMA) of the highest purity. The dye modification with the most photochemical stability and solubility in PMMA will be chosen. The size and shape of the solid state dye active element will be optimized to have the desired output energy and minimal thermo-optical distortions.

Commercial Ti:sapphire crystals and original solid state dye rods pumped by a coaxial lamp with discharge gap of 100-150 mm and pump pulse energy of 100-300 J at voltage of 20-50 kV. To minimize the discharge circuit inductivity, we develop a special coaxial feeder system for connection of the capacitor battery with the flash lamp. For the discharge commutation, a special high-pressure discharger sharpening the front edge of the current pulse is under development.

For narrowing the laser spectrum and for its frequency tuning, it is planned to use a standard dispersive cavity with a prism or a grating. For further line narrowing, an additional tunable short base Fabri-Perrot interferometer will be used. Special attention was paid for cavity optimization in order to minimize thermo-optical distortions. These distortions are the main factor limiting the pulse repetition rate, which is estimated to be less than one pulse per minute. The dye and Ti:sapphire solid state tunable lasers is applied as pump sources for pumping of the mid infrared 4-5  $\mu\text{m}$  solid state laser based on new crystals and glasses studied in this project.

### 8.3 Construction of laser resonators.

To study the lasing properties of dysprosium-doped LaGaGeS:Dy<sup>3+</sup> sulfide glass and KPb<sub>2</sub>Cl<sub>5</sub>:Dy<sup>3+</sup> crystal we built the laser setup with the longitudinal laser pump. The pump radiation from free running ( $P_{av.} = 135$  mW) or Q-switched ( $P_{av.} = 75$  mW,  $f = 1$  Hz,  $t_p = 60$  ns) 1.32  $\mu$ m YAG: Nd laser is focused into the sample by focusing lens with 50-mm focal length. The beam spot on the sample can be varied in the range of 150 - 400 microns. A stable 2.5- 5 cm cavity is made of plane dielectric mirror (100% reflectivity in the 4.3- 5  $\mu$ m spectral region) and a concave Cu-mirror (98% reflectivity) with 5 cm curvature radius made on CaF<sub>2</sub> substrate (Fig. 8.1). In both cavities Dy<sup>3+</sup> crystal or glass sample is placed close to the plane mirror and adjusted parallel to the mirror surface. 4.3  $\mu$ m fluorescence and laser emission is registered by cooled Ge(Au)-photodetector with large sensitive area. Emission wavelength is selected and controlled by the special filter having 3.0- 5.3  $\mu$ m transmission spectral range placed after the output coupler. As the output coupler concave Cu- mirror is used.

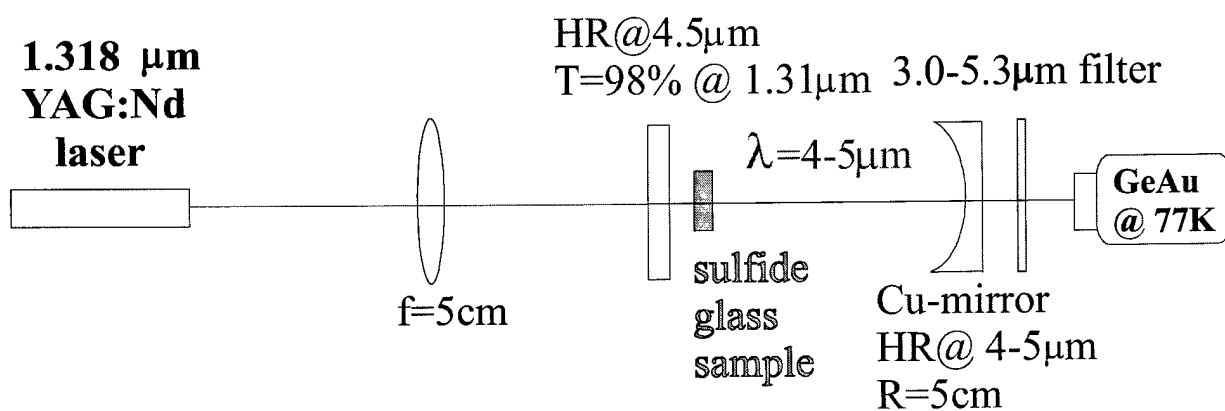


Fig. 8.1 4-5  $\mu$ m laser oscillation setup with 1.318  $\mu$ m YAG:Nd laser pumping.

During this stage the possibility of lasing existence of  $\text{CdF}_2\text{:Er}$  crystals in 4-5  $\mu\text{m}$  spectral range was investigated. In order to selectively excite the upper term  $^4I_{9/2}$  of  $\text{Er}^{3+}$  the free-running short pulse Ti:sapphire laser was used. The structure of pump laser was described above. This laser consists of two-flashlamps cavity with cooling liquid and system of liquid propulsion. As a cooling liquid we chose the Coumarine-30 solution in ethanol to absorb the UV-radiation of the lamp and re-emit it in the blue-green spectral range. The Ti:sapphire rod 8 mm in diameter and 60 mm long was used as active element. The laser reliably operated with up to 20 mJ energy at pulse duration of 5  $\mu\text{s}$ . The pump radiation was focused by focusing lens with 50-mm focal length. The diameter of focal spot can be varied in the range of 100- 300  $\mu\text{m}$ . The lens provided the intensity up to 25  $\text{MW}/\text{cm}^2$  in the focal spot within the specimen of  $\text{CdF}_2\text{:Er}$ .

The spectrum of pump radiation was presented on Fig.8.2. One can see the good correlation of it with the profile of  $^4I_{9/2}$ -level of  $\text{CdF}_2\text{:ErF}_3$  (Fig. 8.3). This agreement allowed us to produce effective exciting  $^4I_{9/2}$  level of  $\text{Er}^{3+}$ .

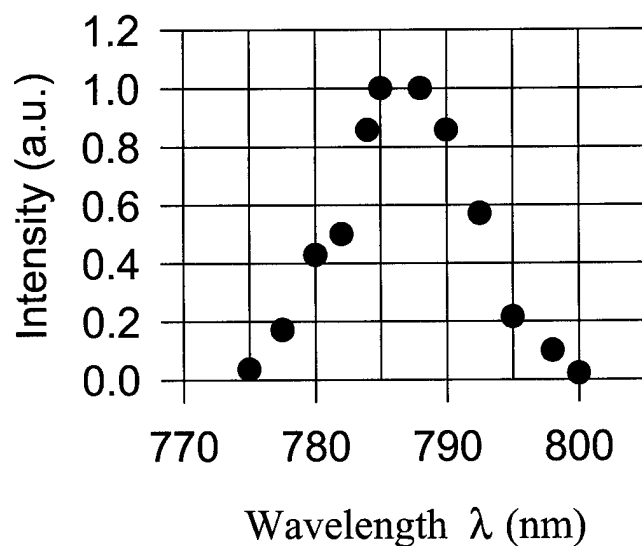


Fig.8.2 The spectrum of Ti:sapphire laser radiation.

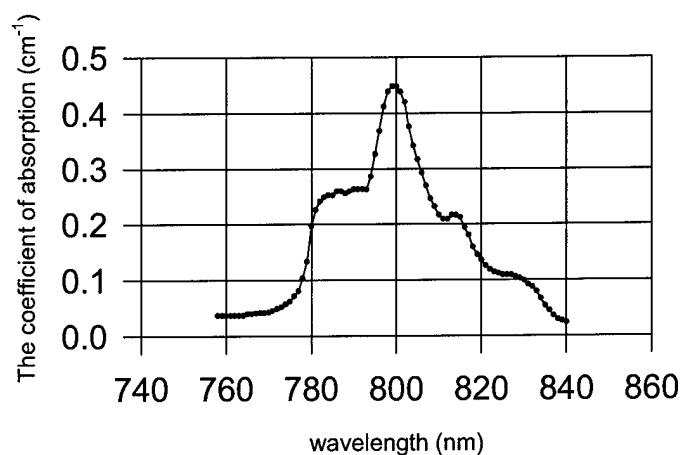


Fig. 8.3. The profile of  $^4I_{9/2}$  level of  $CdF_2:ErF_3$  (5%).

The  $CdF_2:Er$  crystals were prepared in the rod shape of 7-20 mm length and 5 mm in diameter. To determine the absorption of pump radiation in  $CdF_2:Er$  we measured the input energy and transmitting the one. The characteristics of different specimens are shown in table 8.1.

Table 8.1

No.	Concentration of Er (%)	Length of rod (mm)	Absorption
1	5%	10	40%
2	10%	20	80%
3	20%	7	64%

Optical requirements in the 4-5  $\mu m$  spectral region are somewhat different than those in the visible. The transmission curve of glass and fused silica exhibits strong absorption at 3  $\mu m$  and longer. The optical materials that are totally acceptable over the range of 4-5  $\mu m$  are  $CaF_2$  and  $BaF_2$ . Both of them transmit the radiation of whole the range from visible to 7-8  $\mu m$ . In order to guarantee the output of IR-radiation from the cavity all usable laser mirrors were made of  $CaF_2$  or  $BaF_2$ . Transmission curve of the laser mirror presented on Fig.8.4. One can see the small absorption of pump



radiation (780-800 nm). All dielectric mirrors used in studied schemes have reflectivity about 95%-99% in 4-5  $\mu\text{m}$  spectral region.

To detect the possible generation laser radiation the Ge: Au low-temperature detector was used. It was cooled with liquid nitrogen (77 K). The spectral dependence of detector's sensitivity had the maximum near 5  $\mu\text{m}$  wavelength. Emission wavelength is to be selected and controlled by the special filters. These filters separated the spectral region of 3.5-5.2  $\mu\text{m}$  or spectral region of 2.5-3.2  $\mu\text{m}$  to detector adjusting.

We tested some laser cavities with the longitudinal Ti:sapphire laser pumping and  $\text{CdF}_2\text{:Er}$  rod active element.. There are many different optical cavity shemes, which can be used for lasing. During this works stage we tested three of them (see Fig.8.5). There are: a) - semiconfocal, b) - concentric and c) – V shape three-mirror Kogelnik's cavity. The crystal  $\text{CdF}_2\text{:Er}$  routinely was put at the focal point of the laser cavity in order to obtain high gains and low thresholds for laser operation.

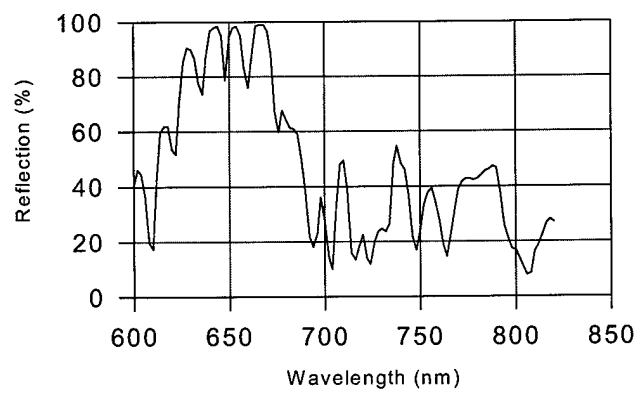
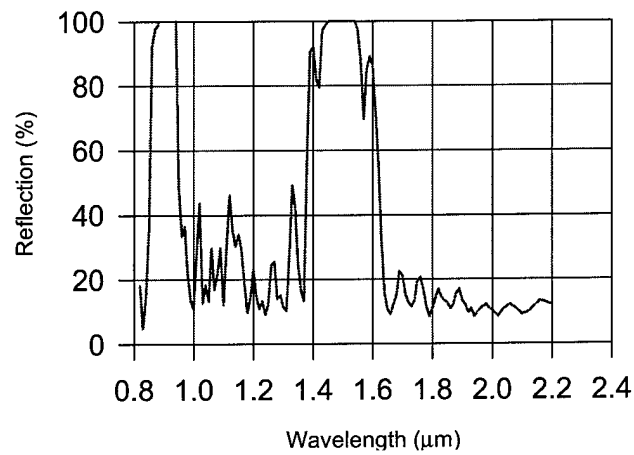
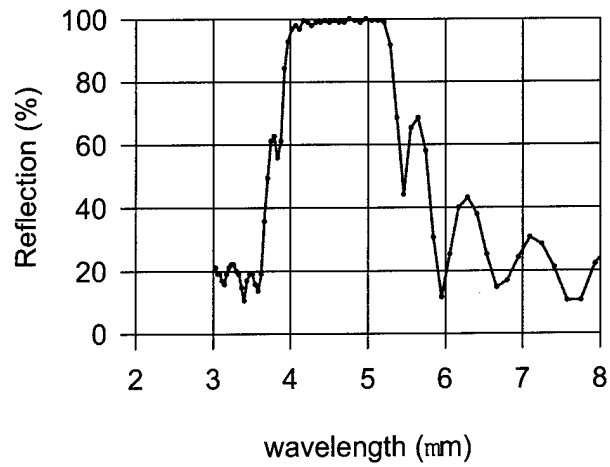
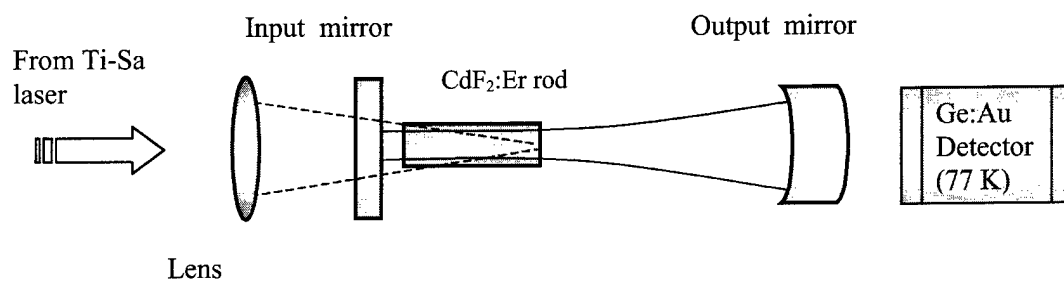
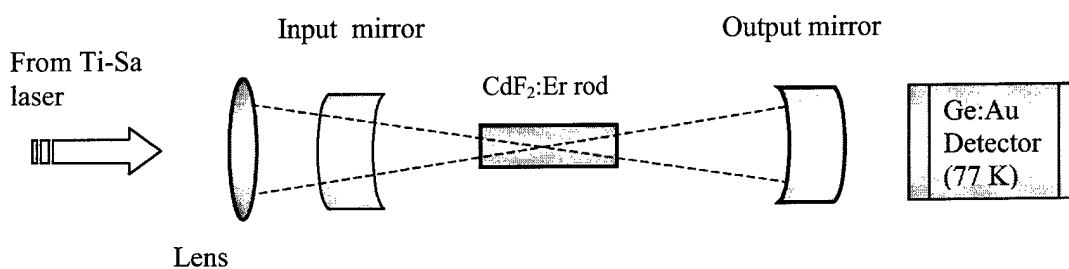


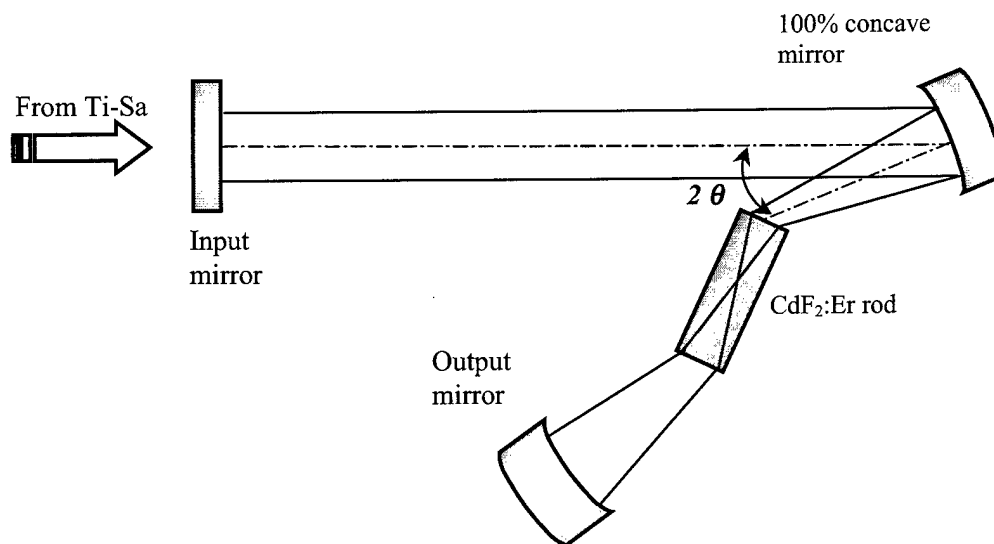
Fig.8.4. The coefficient of laser mirrors reflectivity.



a)



b)



c)

Fig.8.5. The schemes of use laser cavities.

Due to large cavity mode the first design a) required for its operation collinear pumping with small focusing. The stable ~5 cm length cavity consist of plane dielectric mirror (99% reflectivity for 4-5  $\mu\text{m}$  range) and a concave mirror with curvature radius 10 cm with identical coating. For effective gain we have to provide good overlap of the pumping region in laser element with the lowest-order-mode volume of the laser resonator. For this reason the crystal  $\text{CdF}_2\text{:Er}$  was placed into the focus of the pump radiation near the flat mirror. The face of the rod is adjusted parallel to the mirror surface.

In order to obtain a low threshold for laser oscillation, the beam waist must be kept to a minimum. The second scheme b) minimized the beam waist and volume of pumping region. This cavity was made of two concave dielectric mirrors with 5 cm and 10 cm curvature radii. This scheme provide the diameter of the beam waist smaller than the first one and need tight focusing by short focal length lens.

The third scheme c) was three-mirror Kogelnik's cavity. To achieve low losses the active element is oriented at Brewster's angle. The pump beam had horizontal polarization which is necessarily identical to the polarization of eventual Er-laser. The dominant aberration of the third cavity is astigmatism. This scheme provided the astigmatism compensation when the angle  $\theta$  is obtain from the relationship

$$f \sin\theta \tan\theta = [t (n^2-1)(n^2+1)^{1/2}]/n^4$$

Where  $f$  is the focal length of the mirror (50 mm),  $t$  is the crystal thickness and  $n$  is its index of refraction. In our case the value of  $n$  is equal to 1.57, length of the crystal  $t = 7$  mm and the optimal angle  $\theta$  was calculated is about 14 degrees.

Unfortunately, the coma in this cavity do not compensated if the crystal thickness was larger than 1-2 mm. In addition to this only the one our active element (20% Er) may be used because other specimens can't to be oriented at the Brewster's angle in the cavity.

To check the alignment of laser cavity scheme (a), pumping sources and detection system the scheme (a) was modified. Laser crystal YAG:Er ( $\varnothing 5\text{mm} \times 16\text{mm}$ ) was used instead of  $\text{CdF}_2\text{:Er}$  active crystal. The pumping system was the same (Ti:Sa laser). In this experiments two dichroic mirrors were used. Output concave mirror had the curvature radius 10 cm, other mirror was plane. The reflection curve of dichroic laser mirrors was shown in Fig.8.6. It had the maximum of reflection (close to 100%) at 2.5-3.3 $\mu\text{m}$  range. One can see the large transmission of pump radiation (780-800 nm). This provide the possibility to pass pump radiation into the cavity through the flat laser mirror.

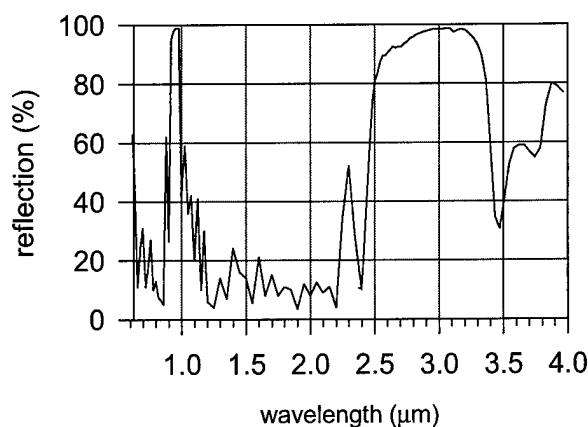


Fig.8.6. The coefficient of mirrors reflection of YAG-Er laser.

The time-resolution picture of oscillations is shown on fig.8.7, where are A – the pulse of YAG-Er laser oscillation (sensitivity- 20 mV/div.), and the B – the pumping pulse (0.2V/div).

With pump energy 3mJ and higher the laser generated pulse of IR 2.94  $\mu\text{m}$  radiation with pulse duration of 0.3-0.5  $\mu\text{s}$ . This radiation was observed to appear at the end of pumping pulse (see Fig 8.7), where A- is the Ge:Au detector signal, B- the pump pulse detected with Ge photodiode.

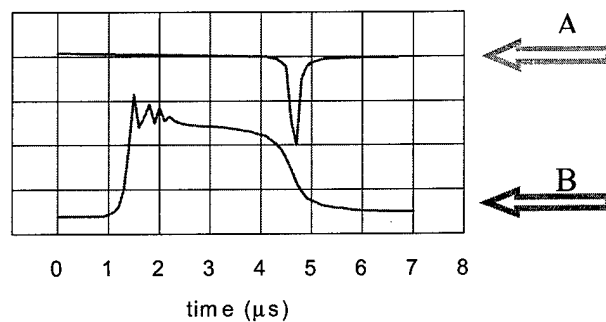


Fig.8.7. The oscillogramm of the 785 nm pump (A) and 2.94  $\mu\text{m}$  lasing (B) pulses.

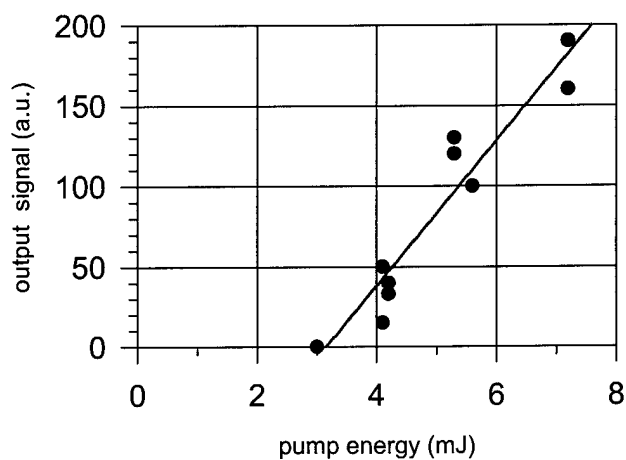


Fig.8.8. Characteristics of YAG:Er laser at 3  $\mu\text{m}$  spectral range.

The measured output energy of the oscillator is shown in Fig.8.8

The experiments with YAG:Er laser showed us the validity of the developed setup - pumping source, detector equipment and cavity scheme. Thus the developed setup can be applied to obtain 4-5  $\mu\text{m}$  range lasing on Er-doped crystals.

At present time lasing experiments within 4-5  $\mu\text{m}$  spectral region are in progress.

### References to chapter 8

1. B.I.Denker, V.V.Osiko, S.E.Sverchkov, Yu.E.Sverchkov, A.P.Fefelov, S.I.Khomenko. Sov.J.Quantum Electron. v.22,p.500 (1992).
2. B.I.Galagan, E.A.Godovikova, B.I.Denker, M.L.Meilman, V.V.Osiko, S.E.Sverchkov. Sov.J.Quantum Electron. v.29,p.189 (1999).

## Chapter 9

### The preparation and characterization of crystals and glasses.

#### 9.1 Fluoride crystals.

According to the statement of Work and the Technical Proposal the following fluoride crystals and fluorine dominated glasses were under special consideration.

Crystals:

1.  $\text{CaF}_2$ ,  $\text{SrF}_2$ ,  $\text{BaF}_2$ ,  $\text{CdF}_2$ ,  $\text{PbF}_2$  as individual compounds and their solid solutions;
2.  $\text{LaF}_3$ ,  $\text{CeF}_3$ ;
3.  $\text{CaF}_2\text{-YF}_3$ ,  $\text{SrF}_2\text{-LaF}_3$  and  $\text{BaF}_2\text{-LaF}_3$  solid solutions.
4.  $\text{BaY}_2\text{F}_8$ ,  $\text{BaYb}_2\text{F}_8$  as individual compounds and  $\text{Ba}(\text{Y}_{1-x}\text{Yb}_x)\text{F}_8$  solid solutions.

$\text{Er}^{3+}$ ,  $\text{Dy}^{3+}$ ,  $\text{Ho}^{3+}$ ,  $\text{Tm}^{3+}$ ,  $\text{Pr}^{3+}$ ,  $\text{Nd}^{3+}$ ,  $\text{Ce}^{3+}$ , and  $\text{Yb}^{3+}$  were used as active ions and co-dopants.

The tables below (Tables 9.1-9.3) present some physico-chemical and physical properties of undoped fluorides considered in this work.

Table 9.1.

	Melting temperatur e, °C	Boiling temperatur e, °C	Termoconduc tivity, cal/g · d egrees · cm · sec	Thermal expansion, $\alpha \cdot 10^{-6}$ degree <sup>-1</sup>	Specific heat, cal/g · Degrees	Chemical reactivity in molten stafe
$\text{CaF}_2$	1360	2500	0.02468	18.38	0.204	Very high
$\text{BaF}_2$	1280	2260	0.017	18.4	-	Very high
$\text{CdF}_2$	1072	1717	-	-	-	Very high
$\text{PbF}_2$	822	1292	-	-	-	Very high

Table 9.2.

	Density , g/cm <sup>3</sup>	Elementary cell parameter $D[\text{\AA}]$	Refractiv e index , $n$	Transparenc y region, $\mu$	Dissolve, g/100 g water	Dielectric constant, $\epsilon$
$\text{CaF}_2$	3.18	5.46295	1.4335	0.14-8	0.0016	6.7 ( $6.4 \cdot 10^5 \epsilon_u$ )
$\text{BaF}_2$	4.83	6.19	1.475	0.23-12	0.17	7,33 ( $2 \cdot 10^6 \epsilon_u$ )
$\text{CdF}_2$	6.64		1.57	0.22-13		9,77 ( $10 \cdot 10^6 \epsilon_u$ )
$\text{PbF}_2(\alpha)$	8.37					
$\text{PbF}_2(\beta)$	7.68					



Table 9.3.

	Melting temperature, °C	Boiling temperature, °C	Density, g/cm <sup>3</sup>	Element. cell parameters $a[\text{\AA}]$	Transparency region, $\mu$
LaF <sub>3</sub>	1493	2300	5.92	$a_0 = 7.186$ , $c_0 = 7.354$	0.2-

The single crystals of fluorides have been grown by crystallization from the melt using vertical directional solidification method. Due to relatively high melting point combined with high chemical reactivity of the melts the technology must meet some rigid requirements:

1. The crucible, heaters and all heated parts of the growth chamber should be made of pure and dense graphite.
2. Special fluorinating atmosphere should be used to prevent the contamination of the melt with the oxygen.

#### **Growth furnace.**

The growth furnace was designed to operate in vacuum, at fluorinating or inert gas atmospheres at pressure up to  $1,5 \cdot 10^5$  Pa and temperatures up to 2000°C. The chamber construction and the materials of the components are presented in Fig.9.1.

The graphite heater of a cylindrical shape with the diameter of 10 cm and 24cm length (1) is fixed on the water-cooled copper conductor (5) and is placed in the water-cooled cylindrical vacuum chamber of 100cm diameter (7). There is special sapphire window in the chamber (8) for visual observation of the growing process. The chamber is connected to a vacuum system, which provides pressure down to  $10^{-3}$  Pa. The special container for a polytetrafluoroethylene (teflon) (10) fixed on a steel rod (11) is placed in the chamber.

The graphite crucible, placed inside the heater, is fixed on a water-cooled rod (6) and can be lowered linearly with the rate from 0.2 to 30 mm / hours by special mechanism.

Three-phase voltage up to 20 V with the operating current of 1210 A is supplied to the heater. Adjustment of the heater temperature is provided by precise power control with  $\pm 2^\circ\text{C}$  accuracy.

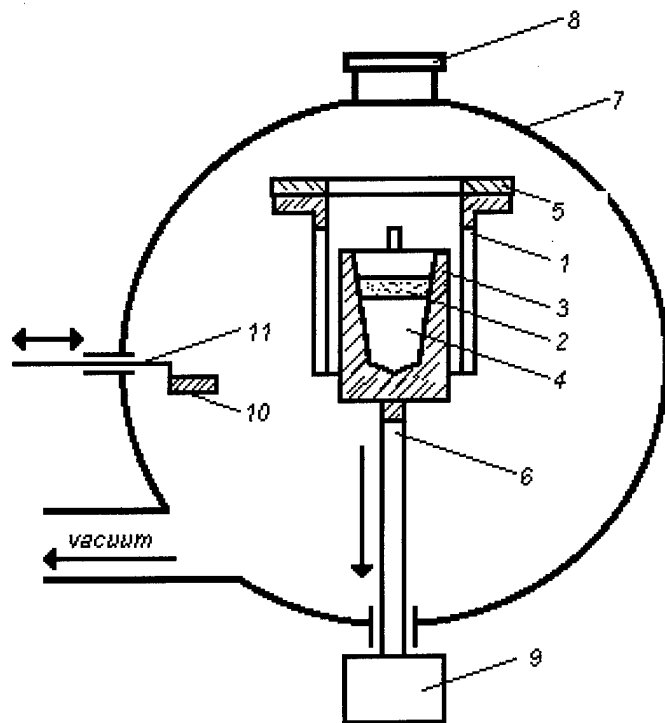


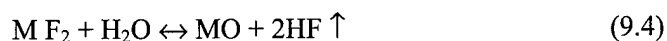
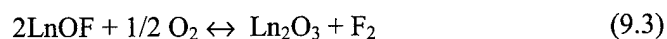
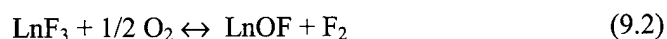
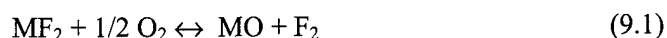
Fig.9.1.

1 - graphite heater, 2 - melt, 3 - graphite crucible, 4- growing crystal, 5 - copper conductor, 6 - lifting rod, 7 - vacuum chamber, 8 - sapphire window, 9 - driving mechanism, 10 - molybdenum container for teflon, 11 - steel rod.

#### Crystal growth technology.

Synthetic alkaline-earth  $\text{MF}_2$ , where  $\text{M} = \text{Ca}, \text{Ba}, \text{Cd}, \text{Pb}$  and rare earth  $\text{LnF}_3$ , where  $\text{Ln} = \text{La}, \text{Ce}$ , fluorides were used as initial raw materials. The concentrations of contaminating impurities in initial powders did not exceed  $10^{-3}\%$  (weight). Optically homogeneous crystals can be synthesized only in case when technology of initial

materials and conditions of synthesis provided rather low level of additional impurities. Among others the presence of oxides and hydroxides is mostly undesirable. During the crystal growth process the non-isomorphic impurity of the oxide segregates as a separate phase in the synthesized crystal and cause strong light scattering [1,2]. Chemical reactions of (9.1-9.3) type occurs in alkaline-earth ( $\text{MF}_2$ ) and rare earth ( $\text{LnF}_3$ ) fluorides in the presence of oxygen, and reactions of (9.4-9.6) type are initiated by moisture:



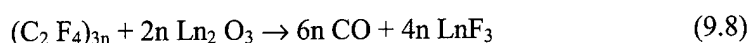
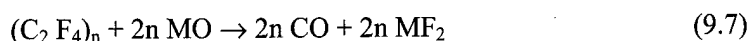
The oxidation and hydrolysis of rare earth fluorides can always be separated in two continuous phases - oxidation and hydrolysis of a fluoride up to oxyfluoride (reactions (9.2) and (9.5)) and then - up to oxide (reactions (9.3) and (9.6)). In [3] the kinetics of reactions (9.1 –9.6) in air were investigated and led to the conclusions, that:

- a. The probability of direct oxidation process in all fluorides under consideration is increased approximately by the order of magnitude with increase of temperature from 298K up to 1700K, but appears to have very low value even at high temperatures;
- b. The reaction of the fluorides hydrolysis is much more thermodynamically preferable than reaction of oxidation by oxygen. As well as in the previous case, the reactions (9.4-9.6) go easier with the temperature increase and the pressure decrease.

- c. At normal conditions all fluorides excluding those in the right part of the rare earth elements group appear to be stable to the hydrolysis reactions.

Optically homogeneous crystals can be obtained during the synthesis process only in the case of deep vacuum [4], special fluorinating admixtures or if active fluorinating atmosphere is provided.

In our laboratory the method based on the active fluorinating atmosphere synthesis is applied. In [5] the application of polytetrafluoroethylene (teflon) pyrolysis products in gas phase in the synthesis process is described. Then the following reactions occur between gas phase and oxides in the melt:



To avoid pyrohydrolysis reactions (9.4-9.6) during the single crystal growth the initial fluoride powders were premelted in active fluorinating atmosphere. For this purpose the materials were placed in a thoroughly annealed graphite crucible, which was installed inside the graphite heater of the crystallizing chamber. The inner diameter of the graphite crucible for the preliminary annealing was 6 cm. The chamber was evacuated up to residual pressure of  $10^{-3}$  Pa and then slow heating of the crucible began. The heating rate was selected so that the chamber pressure does not exceed  $10^{-3}$  Pa.

Then the growth chamber was cut off from a vacuum system and further fluorination in static atmosphere of polytetrafluoroethylene pyrolysis products was carried out. The polytetrafluoroethylene was loaded into the special container (10). To avoid the premature pyrolysis of teflon the rod was completely pulled out from the chamber, placing the container with teflon near an internal wall of the chamber, where it is protected by a heat radiation screen. When fluorination process started the container with teflon was moved towards "hot" zone through the special slot in a graphite screen. Thus teflon was heated above  $600^\circ\text{C}$  and polymeric gaseous

fragments of various structure pass into the chamber atmosphere. Contact with even more hot crucible and melt leads to further pyrolysis resulting in formation of carbon fluoride radicals in gas phase, which can be observed by appearance of free carbon on the melt surface and thermal shields. The products of a pyrolysis actively interact with oxygen-containing impurities in melt according to reactions (9.7-9.8).

The fluorination process lasts 2÷3 hours. The teflon quantity, loaded into the chamber, is usually about 20 g and corresponds to the quantity of treated material and concentration of oxygen-containing impurity.

Polycrystalline ingot which was transparent and free from other phase inclusions was used for the further single crystal synthesis. To remove the traces of oxygen-containing impurities and to prevent the melt pollution during the crystal growth due to chamber inleakage the crystallization process is also carried out in atmosphere of gaseous products of polytetrafluoroethylene pyrolysis. The premelted fluorides were loaded into a crucible, which was installed inside the heater of the crystallizing chamber. The crucible for single crystal synthesis had single or several channels in the form of a cone (Fig.9.1). After evacuation of the chamber up to  $10^{-3}$  Pa the heater power supply was activated and the heaters temperature was slowly increased up to the value necessary for the synthesis process, thus the melt was overheated 50-100° C above the melting point. The temperature gradient of about 100°C/cm was provided in the crystallization zone. When the fluorination process was finished the crucible was moved down during 10÷30 minutes by the special mechanism. As soon as the melt at the crucible bottom was overcooled enough, the formation of crystalline seeds starts, at the cone top, where the temperature was minimal, initiating the growth of several crystals. However, in the growth rate selection processes takes place resulting "survival" of the single crystal. Thus all melt volume was transformed gradually into single crystal. The dopants were added to the initial loading in the form of corresponding fluorides. To remove the residual

thermoelastic stresses, the synthesized crystals were subjected to annealing. The annealing was carried out in fluorinating atmosphere. The crystals were heated to the temperature 200 - 300°C below the melting point and were annealed at this temperature from 2 till 6 hours. Then they were slowly cooled with temperature decrease about 70°/hour.

## Results.

1. Following chemicals were purchased and previously tested:

MgF<sub>2</sub>, CaF<sub>2</sub>, SrF<sub>2</sub>, BaF<sub>2</sub>; ZnF<sub>2</sub>, CdF<sub>2</sub>, PbF<sub>2</sub>.

YF<sub>3</sub>, LaF<sub>3</sub>, CeF<sub>3</sub>, PrF<sub>3</sub>, NdF<sub>3</sub>, DyF<sub>3</sub>, ErF<sub>3</sub>, HoF<sub>3</sub>, TmF<sub>3</sub>, YbF<sub>3</sub>.

ZrF<sub>4</sub>, HfF<sub>4</sub>.

2. Premelting and fluorination of most of above mentioned fluorides were carried out.

3. Bulk graphite MG-1, which is characterized with high chemical purity and high density, was purchased. Crucibles, heaters, after-heaters and heat screens were fabricated of graphite mechanically in LMTRC.

4. Growth furnace was specially suited to the objectives of this contract.

5. Special furnace for fluoride glasses preparation was assembled.

6. Following crystals were grown (Tables. 9.4, 9.5, 9.6, 9.7)

Table 9.4.

Matrix	Dopant, (Co-dopant)	Conc., mole %
CaF <sub>2</sub>	ErF <sub>3</sub>	1; 0.3; 0.1; 0.03
CaF <sub>2</sub> :YF <sub>3</sub> (3 mole %)	ErF <sub>3</sub>	1; 0.3; 0.1; 0.03
CaF <sub>2</sub> :YF <sub>3</sub> (8 mole %)	ErF <sub>3</sub>	1; 0.3; 0.1; 0.03
CaF <sub>2</sub> :YF <sub>3</sub> (12 mole %)	ErF <sub>3</sub>	1; 0.3; 0.1; 0.03
BaF <sub>2</sub>	ErF <sub>3</sub>	1; 5; 14.1; 16.7; 23.6; 41
BaF <sub>2</sub>	DyF <sub>3</sub>	0.003; 0.01
BaF <sub>2</sub>	YbF <sub>3</sub>	4.5
	DyF <sub>3</sub>	0.03; 0.1; 0.3
BaF <sub>2</sub>	ErF <sub>3</sub>	4.5
	DyF <sub>3</sub>	0.03; 0.1
CdF <sub>2</sub>	ErF <sub>3</sub>	1; 5; 10; 15; 20; 30
CdF <sub>2</sub>	YbF <sub>3</sub>	10
	ErF <sub>3</sub>	5
CdF <sub>2</sub>	YbF <sub>3</sub>	20
	ErF <sub>3</sub>	5

CdF <sub>2</sub> :YF <sub>3</sub> (5 mole %)	ErF <sub>3</sub>	5
CdF <sub>2</sub> :YF <sub>3</sub> (10 mole %)	ErF <sub>3</sub>	5
CdF <sub>2</sub> :YF <sub>3</sub> (15 mole %)	ErF <sub>3</sub>	5
CdF <sub>2</sub> :YF <sub>3</sub> (20 mole %)	ErF <sub>3</sub>	5
CdF <sub>2</sub> :YF <sub>3</sub> (25 mole %)	ErF <sub>3</sub>	5
PbF <sub>2</sub>	ErF <sub>3</sub>	~2
PbF <sub>2</sub>	ErF <sub>3</sub>	~10

Table 9.5.

Matrix	Dopants (mole %)				
	NdF <sub>3</sub>	HoF <sub>3</sub>	DyF <sub>3</sub>	ErF <sub>3</sub>	TmF <sub>3</sub>
LaF <sub>3</sub>	0.5	-	-	-	-
	0.1; 1; 1.5	-	-	-	-
	-	0.3; 1; 3	-	-	-
	-	-	0.3; 1; 2	-	-
	-	-	-	1.23; 2.97; 6.17; 11.3; 0.3; 1; 2	-
	-	-	-	-	0.3; 1; 3
LaF <sub>3</sub> : CeF <sub>3</sub> (5 mole %)	0.5	-	-	-	-

Table 9.6.

Matrix	Dopant (Co-dopant)	Concentration, mole%
BaF <sub>2</sub> single cryst.	ErF <sub>3</sub>	0.1; 0.3; 1; 10; 30
	DyF <sub>3</sub>	0.1; 0.3; 1; 10; 30
CdF <sub>2</sub> single cryst.	ErF <sub>3</sub>	0.1; 0.3
	DyF <sub>3</sub>	0.1; 0.3; 1; 10; 30
CdF <sub>2</sub> +YF <sub>3</sub> (5%)	ErF <sub>3</sub>	0.1; 0.3; 1
BaY <sub>2</sub> F <sub>8</sub> poly cryst.	ErF <sub>3</sub>	0.5; 1; 3; 5; 10; 15
	DyF <sub>3</sub>	0.1; 0.3; 0.5; 0.7; 1; 1.5
La <sub>(1-x)</sub> Ce <sub>x</sub> F <sub>3</sub> single cryst.	ErF <sub>3</sub> (0.5%)	0; 0.4; 0.6; 0.8; 1
	TmF <sub>3</sub> (0.5)	0; 0.2; 0.4; 0.6; 0.8; 1

Special attention have been paid to Cd<sub>1-x-y</sub>Y<sub>x</sub>Er<sub>y</sub>F<sub>2-x-y</sub> solid solutions. Specific feature

of these crystals is that even at very high concentrations of ErF<sub>3</sub> (or YF<sub>3</sub>) equal to 20-30 mole %, the crystals remain optically uniform and do not contain variations of refractive index. On the contrary the optical perfection of BaF<sub>2</sub>:ErF<sub>3</sub> crystals dramatically aggravates even at 1 mole % of ErF<sub>3</sub>.

Table 9.7.

Dopant Matrix	ErF <sub>3</sub> , conc. mole %	YF <sub>3</sub> , conc. mole %	HoF <sub>3</sub> , conc. mole %
PbF <sub>2</sub>	0.1, 0.3, 0.5, 0.8, 1, 5	-	-
SrF <sub>2</sub>	0.1, 0.5, 0.8, 1, 5, 10, 20, 30,	-	-
	0.1	0.5	-
	0.3, 0.5	1	-
	0.8	5	-
BaF <sub>2</sub>	-	-	0.5, 1, 5, 10,
	0.1	0.5	-
	0.3, 0.5	1	-
	1	5	-
	-	-	0.5, 1, 5

7. Following glass samples were prepared (will be given in the chapter 9.2).

8. IR absorption spectra of some fluoride crystals have been reexamined (Fig.9.2).

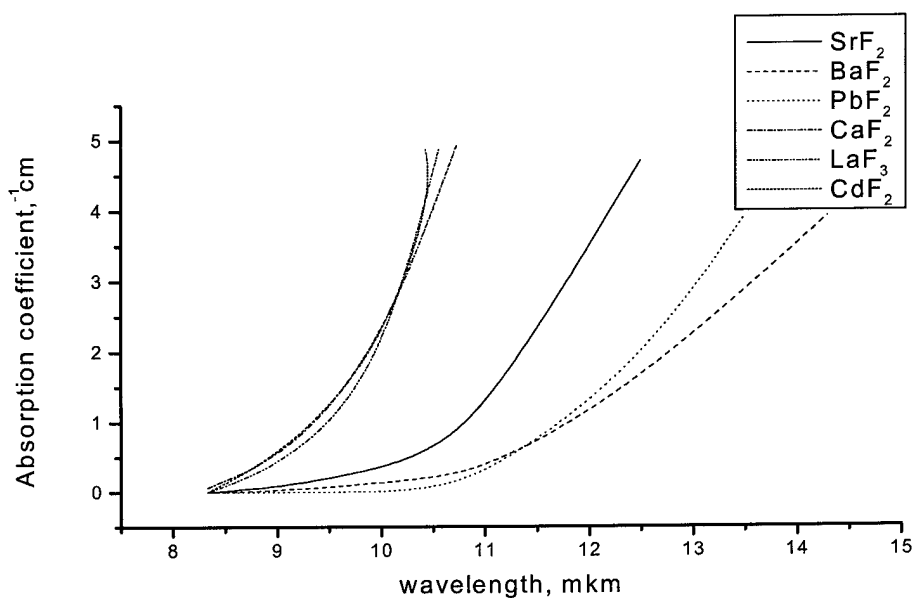


Fig.9.2. IR absorption spectra of some fluoride crystals.

Most of the crystals were structurally uniform, perfectly transparent and free of solid or gaseous inclusions. The dimensions of the samples were large enough to carry out spectroscopic and previous laser experiments.



## 9.2 Halide glasses for IR lasers

Halide glasses based on heavy metal halogenides have lower passive losses and less nonradiative relaxation at IR laser action in comparison with known oxide glasses due to good IR transmission. (Fig.9.3).

At present time the fluoride, chloride and bromide glasses are known. Chloride and bromide glasses as IR laser materials have evident advantage with respect to IR transmission. However these glasses are highly hygroscopic. Besides of there is a problem of eliminating of IR absorbing impurities (oxygen,  $\text{OH}^-$ ,  $\text{H}_2\text{O}$ ) from the raw materials and glasses.

A lot of fluoride glasses of different compositions were developed recently in connection with the optical waveguides problems. The high purity glasses based on Zr,Al,In,Cd,Zn and Th fluorides were prepared. The purification techniques of the raw fluorides were also developed. All fluoride glasses are multicomponent and contain from 3 to 8 different fluorides. The fluoride glasses are not hygroscopic and are stable in air atmosphere. The crystallization of glasses in the course of melt cooling is characteristic feature of many glass compositions. Some typical compositions of stable glasses are given in Table 9.8.

Table 9.8 The compositions of fluoride glasses stable to crystallization.

Glass Mol%	ZrF <sub>4</sub>	ThF	InF <sub>3</sub>	AlF	LaF	YF <sub>3</sub>	MgF <sub>2</sub>	CaF	SrF <sub>2</sub>	BaF	NaF	ZnF
		4		3				2		2		2
ZBLAN	53			3	4					20	20	
HBLAN	53 HfF <sub>4</sub>			3	4					20	20	
AYR				40		15	10	15	10	10		
IZBS		5	35						20	20		20

The fluorozirconate and fluorohafnate compositions of ZBLAN (HBLAN) type are the most studied among all fluoride glasses.

The fluorozirconate glass of ZBLAN type shows best glassforming properties. Critical cooling rate and difference between crystallization and glassforming temperatures ( $T_x - T_g$ ) which are the measure of glassforming ability are about  $1^\circ/\text{min}$  and  $120^\circ\text{C}$  respectively. It is possible to prepare high optical quality glasses with the thickness up to few cm. The fluorohafnate and fluoroaluminate glasses have similar glassforming abilities. The fluoroindate glasses have a slightly less glassforming ability. ( $T_x - T_g$ ) parameter of these glasses is about  $90^\circ\text{C}$ .

The physical and physics-chemical properties of some fluoride glasses are given in Table 9.9

Table 9.9 The properties of fluoride glasses

PROPERTIES	ZBLAN	HBLAN	AYR	IZBS
Refractive index $n_d$	1.498	1.505	1.439	1.52
Abbe value $v_d$	75.95	-	93.79	-
Absorption edge (5mm thickness)				
UV $\lambda_{T=50\%}$ ( $\mu\text{m}$ )	0.21	0.25	0.21	0.28
IR $\lambda_{T=50\%}$ ( $\mu\text{m}$ )	7.19	7.60	6.76	8.4
$(dn/dT)_{\text{rel}}$ ( $10^{-6}/^\circ\text{C}$ )	-13.45	-	-8.17	-
Rayleigh's ratio ( $\lambda=633\text{nm}$ ) $R_{90} \times 10^6/\text{cm}$	5.0		1.5	
Density, $\text{g}/\text{cm}^3$	4.33	5.85	3.85	5.20
Durability in humid air	stable	stable	stable	stable
Water solubility, Relative units	29.	25	0.2	20
Transformation point $T_g$ ( $^\circ\text{C}$ )	257	265	392	-
Thermal expansion coeff. in temp. Range ( $-30 \sim 70^\circ\text{C}$ ) $\times (10^7/^\circ\text{C})$	172	160	152	-
Young's modulus ( $\text{kg}/\text{mm}^2$ )	5380	5500	6500	-
Knoop hardness ( $\text{kg}/\text{mm}^2$ )	225	240	315	-

The IR absorption edges of all fluoride glasses are shifted to shorter wavelengths in comparison with that of chloride glasses. However it is still sufficiently transparent in order to satisfy the 4-5  $\mu\text{m}$  laser application.

At least two requirements should be satisfied in order to obtain suitable glass composition for IR laser. At first the glass network should be formed from the heavy cations and anions to decrease multiphonon relaxation. And secondly glasses must possess good glassforming properties to provide the preparation of high optical quality samples.

The laboratory set up and the preparation technique of the fluoride glasses doped with rare earth fluorides have been developed. Set up for fluoride glass preparation is shown in Fig.9.4. The batch was melted in glass carbon covered graphite boat at 820°C for about 40 minutes under argon atmosphere. Then the melt was cooled to room temperature at a cooling rate of 30-40°/min. The next fluoride glasses doped with rare earth fluorides have been prepared:

-54 HfF<sub>4</sub>,20BaF<sub>2</sub>, 3LaF<sub>3</sub>,2,5AlF<sub>3</sub>, 20NaF,0,5InF<sub>3</sub>+1%wt DyF<sub>3</sub>;

-54 HfF<sub>4</sub>,20BaF<sub>2</sub>, 3LaF<sub>3</sub>,2,5AlF<sub>3</sub>, 20NaF,0,5InF<sub>3</sub>+1%wt ErF<sub>3</sub>;

-54 HfF<sub>4</sub>,20BaF<sub>2</sub>, 3LaF<sub>3</sub>,2,5AlF<sub>3</sub>, 20NaF,0,5InF<sub>3</sub>+1%wt TmF<sub>3</sub>;

-54 HfF<sub>4</sub>,20BaF<sub>2</sub>, 3LaF<sub>3</sub>,2,5AlF<sub>3</sub>, 20NaF,0,5InF<sub>3</sub>+1%wt HoF<sub>3</sub>;

-54 ZrF<sub>4</sub>,20BaF<sub>2</sub>, 3LaF<sub>3</sub>,2,5AlF<sub>3</sub>, 20NaF,0,5InF<sub>3</sub>+1%wt DyF<sub>3</sub>;

-54 ZrF<sub>4</sub>,20BaF<sub>2</sub>, 3LaF<sub>3</sub>,2,5AlF<sub>3</sub>, 20NaF,0,5InF<sub>3</sub>+1%wt ErF<sub>3</sub>;

-54 ZrF<sub>4</sub>,20BaF<sub>2</sub>, 3LaF<sub>3</sub>,2,5AlF<sub>3</sub>, 20NaF,0,5InF<sub>3</sub>+1%wt TmF<sub>3</sub>;

-54 ZrF<sub>4</sub>,20BaF<sub>2</sub>, 3LaF<sub>3</sub>,2,5AlF<sub>3</sub>, 20NaF,0,5InF<sub>3</sub>+1%wt HoF<sub>3</sub>;

Some substituted fluorohafnate glasses have been developed on this stage of the project. The main idea is to achieve the compromise in shifting of the IR absorption edge to the longer wavelength in the one hand and keeping well glass forming properties, high mechanical and physico-chemical properties of the initial fluorohafnate glass – on the other. For this purpose we proposed:

- the substitution (partial or complete) of Al and Ba fluorides with the “heavier” In and Pb fluorides;
- the partial substitution of fluorine with chlorine.

melting and casting of glasses were carried out in graphite boats in Ar atmosphere.

The chlorine substitution was carried out by the replacement of NaF by NaCl, PbF<sub>2</sub> by PbCl<sub>2</sub>, and BaF<sub>2</sub> by BaCl<sub>2</sub>. Typical impurity levels in starting chemicals were as low as 500-2000 ppm. The glass melting temperatures were in the range of the glass forming properties of some modified compositions were estimated previously. The 800-840 °C. The cooling rate was about 40 °C/min. Polished samples 3mm thick and 6mm in diameter were examined by means of optical microscopy in order to estimate crystallization behavior. The Tables 9.10 and 9.11 presents compositions, glass forming ability and IR transmission edges of substituted fluorohafnate glasses. IR transmission spectra for some substituted fluorohafnate glasses are shown in figures 9.3 and 9.4.

As can be seen from presented data the substitution with “heavy” cations and with chlorine significantly shifts the IR absorption edge towards longer wavelength. Complete substitution of AlF<sub>3</sub> with InF<sub>3</sub> and BaF<sub>2</sub> with BaCl<sub>2</sub> gives maximal shift. Fig 9.5 displays absorption spectra of Dy<sup>3+</sup> and Er<sup>3+</sup> doped substitution glasses.

Table 9.10. Crystallization behaviour and IR absorption edge of some fluoride glasses with cation substitution .

Composition, mol. %	Melting	Samples*	Absorption edge at T=50% (3mm thickness), mkm
Base composition 57.5HfF <sub>4</sub> 20BaF <sub>2</sub> 3LaF <sub>3</sub> 2.5AlF <sub>3</sub> 17NaF	run 1 2 3	gl. gl. gl.	7.75
In/Al substitution 57.5HfF <sub>4</sub> 20BaF <sub>2</sub> 3LaF <sub>3</sub> 2.5InF <sub>3</sub> 17NaF	run 1 2 3	gl.+incl. gl. gl.	7.95
Pb/Ba substitution 57.5HfF <sub>4</sub> 10BaF <sub>2</sub> 10PbF <sub>2</sub> 2.5AlF <sub>3</sub> 17NaF	run 1 2 3	gl. gl. gl.+incl.	7.8
Pb/Ba substitution 57.5HfF <sub>4</sub> 20PbF <sub>2</sub> 3LaF <sub>3</sub> 2.5AlF <sub>3</sub> 17NaF	run 1 2 3	cr. gl.+incl. gl.+incl.	
In/Al and Pb/Ba substitution 57.5HfF <sub>4</sub> 20PbF <sub>2</sub> 3LaF <sub>3</sub> 2.5InF <sub>3</sub> 17NaF	run 1 2 3	cr. cr. cr.	

\* gl. - glass samples; gl.+incl. - glass with crystalline inclusions;  
cr. - crystalline samples.

Table 9.11 Crystallization behaviour and IR absorption edge of some 57.5HfF<sub>4</sub>20BaF<sub>2</sub>3LaF<sub>3</sub>2.5InF<sub>3</sub>17NaF glasses with anion substitution.

Chloride concentration, mol. %	Cl/F ratio	Melting	Samples	Absorption edge at T=50% (3mm thickness), mkm
5NaCl	1/60	run 1 2	gl. gl.	7.95
10NaCl	1/30	run 1 2 3	gl. gl. gl.+incl.	
20NaCl	1/15	run 1 2	cr. cr.	
5PbCl <sub>2</sub>	1/30	run 1 2	gl.+incl. cr.	
10PbCl <sub>2</sub>	1/15	run 1 2	cr. cr.	
10BaCl <sub>2</sub>	1/15	run 1 2	gl. gl.+incl.	8.10
20BaCl <sub>2</sub>	1/7.5	run 1 2 3	gl. gl.+incl. gl.+incl.	8.25

\* gl. - glass samples; gl.+incl. - glass with crystalline inclusions; cr. - crystalline samples.

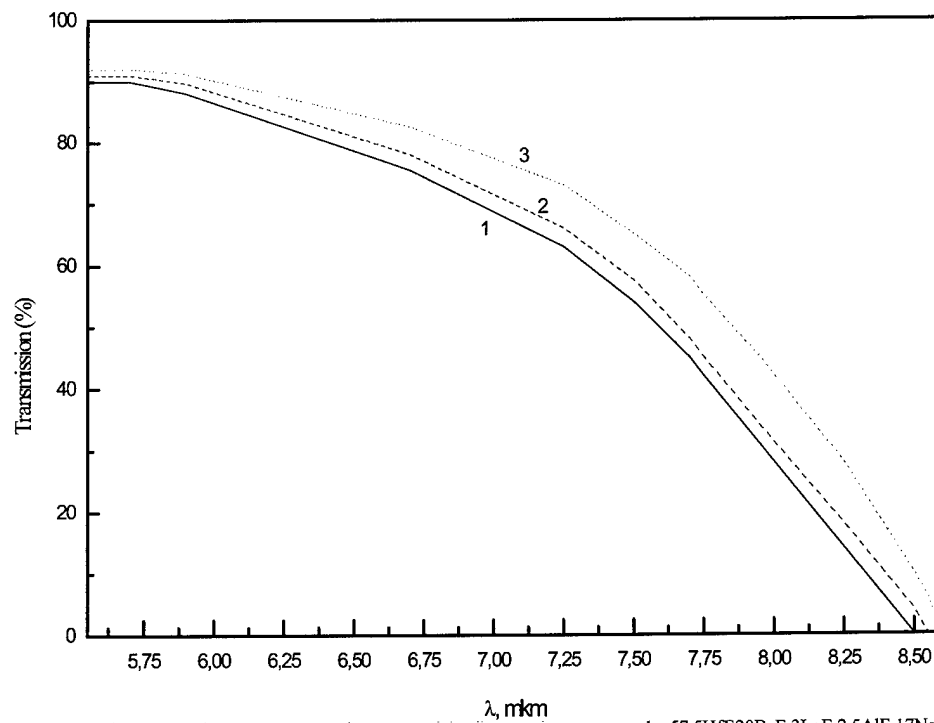


Fig 9.3 The IR transmission edges of some substituted fluorohafnate glasses.

1 -  $57.5\text{HfF}_4\text{20BaF}_2\text{3LaF}_3\text{2.5AlF}_3\text{17NaF}$ ;

2 -  $57.5\text{HfF}_4\text{10BaF}_2\text{10PbF}_2\text{3LaF}_3\text{2.5AlF}_3\text{17NaF}$ ;

3 -  $57.5\text{HfF}_4\text{20BaF}_2\text{3LaF}_3\text{2.5InF}_3\text{17NaF}$ .

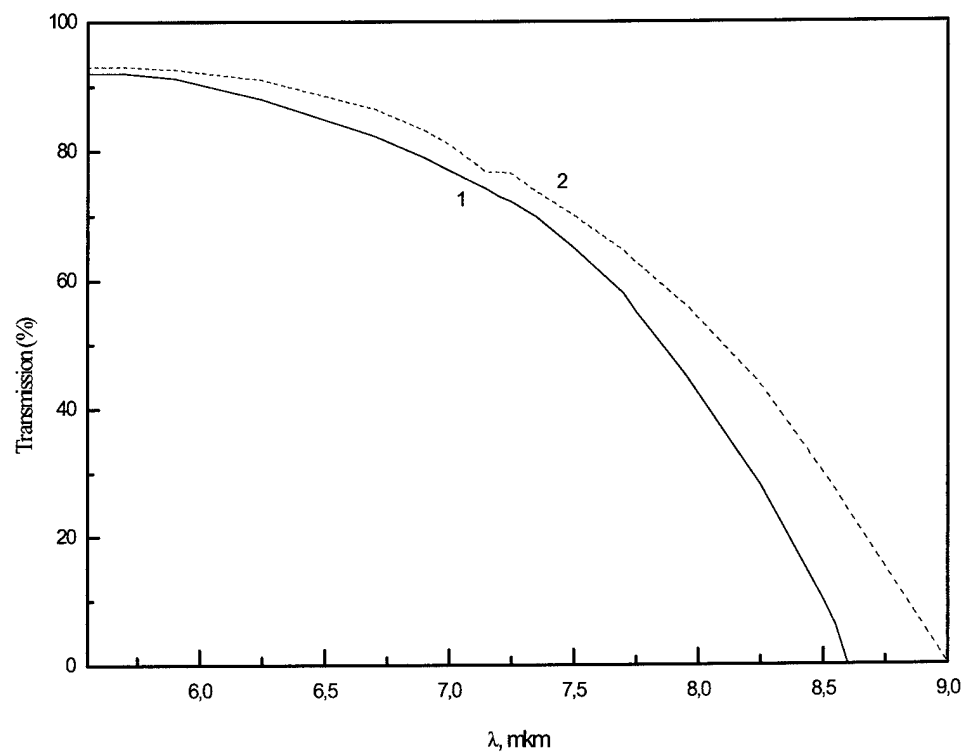


Fig 9.4 The effect of chlorine substitution on the IR transmission edge of fluorohafnate glasses.

1 -  $57.5\text{HfF}_4\cdot 20\text{BaF}_2\cdot 3\text{LaF}_3\cdot 2.5\text{InF}_3\cdot 17\text{NaF}$ ;  
 2 -  $57.5\text{HfF}_4\cdot 20\text{BaCl}_2\cdot 3\text{LaF}_3\cdot 2.5\text{InF}_3\cdot 17\text{NaF}$ .

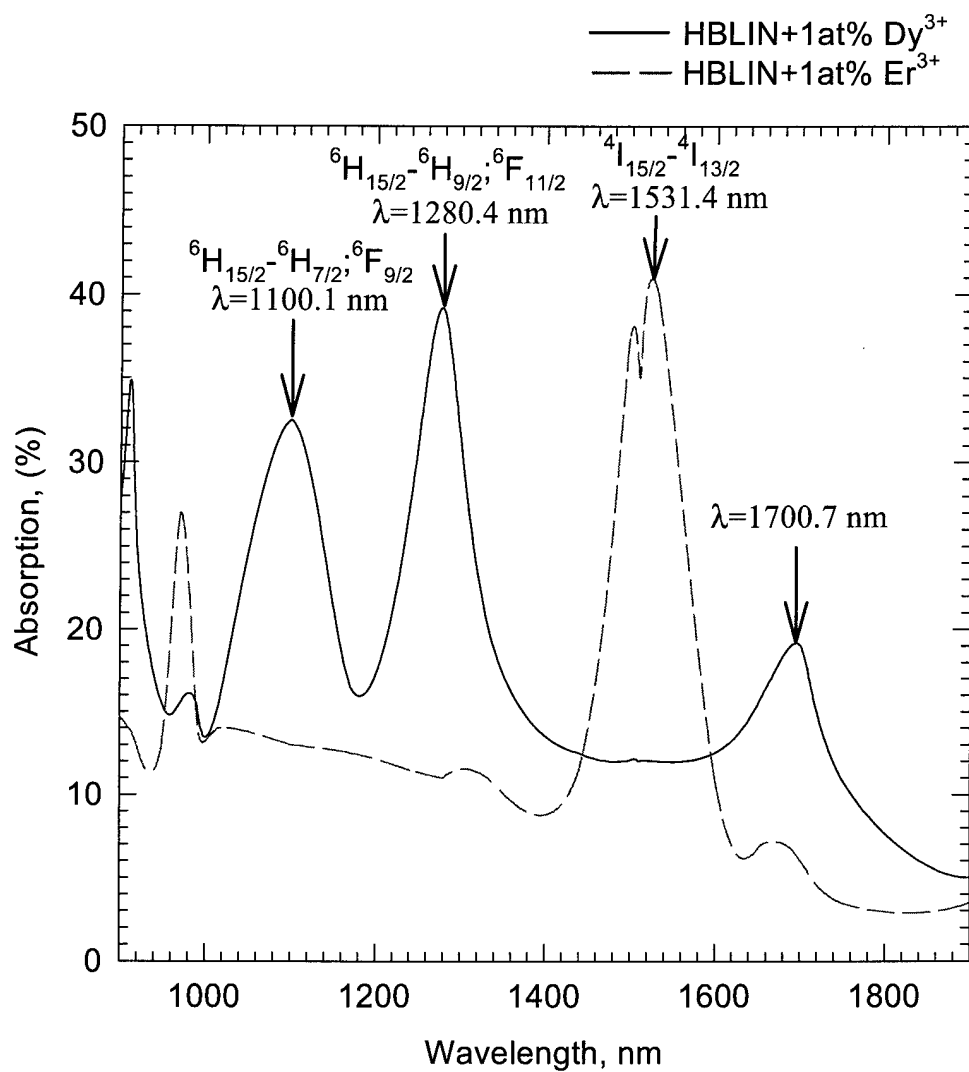


Fig. 9.5 Absorption spectra of the  $57.5\text{HfF}_4 20\text{BaCl}_2 3\text{LaF}_3 2.5\text{InF}_3 17\text{NaF}$  glasses doped with Dy<sup>3+</sup> and Er<sup>3+</sup>.



The crystallization behavior of the  $\text{HfF}_4$ -based fluoride-chloride glasses doped with 1-10 mol.% of  $\text{DyF}_3$  and 1-10 mol.% of  $\text{ErF}_3$  was studied to determine the maximum content of  $\text{RF}_3$  which can be incorporated into the  $\text{HfF}_4$ -based fluoride-chloride glasses. The glass compositions were  $55.5\text{HfF}_4\text{-}20\text{BaCl}_2\text{-}x\text{RF}_3(5\text{-}x)\text{LaF}_3\text{-}2\text{InF}_3\text{-}17\text{NaF}$  ( $\text{RF}_3$  -  $\text{DyF}_3$ ,  $\text{ErF}_3$ ,  $x=1\text{+}5$ ) in the case of  $\text{RF}_3$  content less than 5 mol.% and  $(55.5\text{-}y)\text{HfF}_4\text{-}20\text{BaCl}_2\text{-}(5\text{+}y)\text{RF}_3\text{-}2.5\text{InF}_3\text{-}17\text{NaF}$  in the case of  $\text{RF}_3$  content more than 5 mol.%.

Ten compositions with different  $\text{RF}_3$  concentrations were melted simultaneously under identical conditions. The cooling rate of the melts was about  $40^\circ/\text{min.}$  in the temperature range of crystallization ( $430\text{-}350^\circ\text{C}$ ). The glass or crystalline samples were obtained depending on  $\text{RF}_3$  concentration. The results are shown in Table 9.12.

Table 9.12 The fluoride-chloride samples doped with  $\text{DyF}_3$  and  $\text{ErF}_3$ .

$\text{DyF}_3$ content, mol.%	Sample	$\text{ErF}_3$ content, mol.%	Sample
1	glass	1	glass
3	glass	3	glass
5	glass	5	glass
6	glass	6	glass
7	glass	7	glass
8	poly-crystalline	8	poly-crystalline
10	poly-crystalline	10	polycrystalline

DSC measurements for some glasses were carried out at heating rate of  $10^\circ/\text{min.}$  between  $200\text{-}600^\circ\text{C}$  using "Setaram" model. A typical DSC scan at  $10^\circ/\text{min}$  for  $55.5\text{HfF}_4\text{-}20\text{BaCl}_2\text{-}5\text{DyF}_3\text{-}2.5\text{InF}_3\text{-}17\text{NaF}$  glass is shown in Fig.9.6.

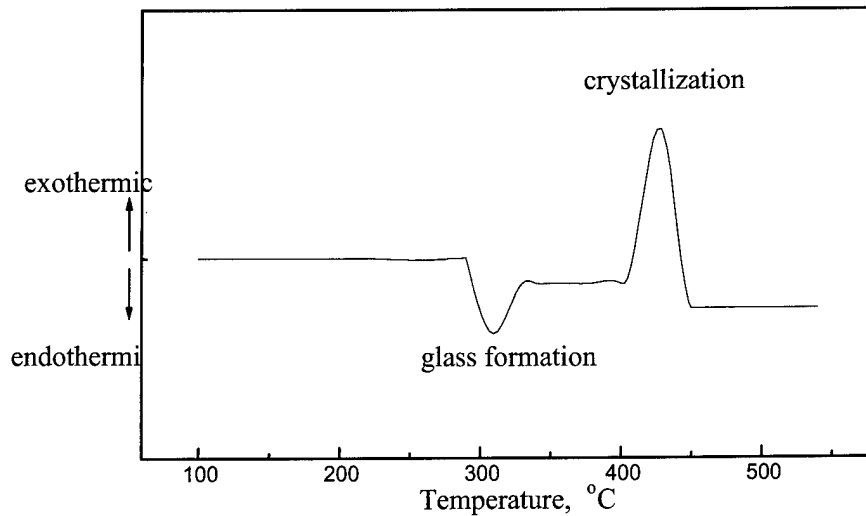


Fig. 9.6 DSC scan at 10 °/min for 55.5HfF<sub>4</sub>-20BaCl<sub>2</sub>-5DyF<sub>3</sub>-2.5InF<sub>3</sub>-17NaF glass. Characteristic temperatures of some fluoride-chloride glasses from DSC measurements are shown in Table 9.13.

Table 9.13. Characteristic temperatures of the fluoride-chloride glasses doped with RF<sub>3</sub>

Glass composition	Glassforming temperature T <sub>g</sub> , °C	Crystallization temperature T <sub>x</sub> , °C	T <sub>x</sub> -T <sub>g</sub> , °C
55.5HfF <sub>4</sub> -20BaCl <sub>2</sub> -2InF <sub>3</sub> -17NaF-3LaF <sub>3</sub>	277	398	121
— " — " — " — 5 ErF <sub>3</sub>	282	400	118
— " — " — " — 5DyF <sub>3</sub>	281	400	119
— " — " — " — 7ErF <sub>3</sub>	285	401	116
— " — " — " — 7DyF <sub>3</sub>	286	399	113

From the data of Table 6 and Table 7 one can see that fluoride-chloride glasses doped with DyF<sub>3</sub> and ErF<sub>3</sub> show good glass forming properties up to 7 mol.% DyF<sub>3</sub> or ErF<sub>3</sub>. Therefore conventional casting technique can be used to prepare the laser glass rod with RF<sub>3</sub> concentration up to 7 mol.% RF<sub>3</sub>.

### 9.3 Growth of $\text{KPb}_2\text{Cl}_5$ crystals.

As a first step growth of  $\text{KPb}_2\text{Cl}_5$  crystals was examined by Chochralsky technique. Stoichiometric batch of  $\text{KCl}$  and  $\text{PbCl}_2$  were melted in platinum crucible using high frequency heating. Intensive evaporation of lead chloride was observed.

Therefore at present time we proffered the growth of  $\text{KPb}_2\text{Cl}_5$  crystals by vertical direct crystallization method. Preliminary we tested different crucible materials (silica glass, platinum, corundum, graphite). It was found that silica glass is the most convenient material for melting  $\text{KPb}_2\text{Cl}_5$  among of all tested materials. We found that silica does not reacts chemically with  $\text{KPb}_2\text{Cl}_5$  melt, and the grown crystal easily comes off from the silica vessel.

The laboratory set up for growth of the  $\text{KPb}_2\text{Cl}_5$  single crystal have been assembled. The scheme of set up is shown in Fig. 9.7. The set up consists of two zone resistant furnaces, pulling mechanism and temperature control unit.

The growth process included the melting of ingot, adjusting temperatures of «hot» and «cold» zones and slow pulling down silica glass ampule. The choice of convenient temperature conditions, growth rate as well as preliminary chemical treatment of raw materials allows to prepare transparent  $\text{KPb}_2\text{Cl}_5$  single crystals of 5 mm diameter and some cm length.

### 9.4 Sulfide glasses

The sulfide glasses of  $\text{La}_2\text{S}_3\text{-Ga}_2\text{S}_3\text{-GeS}_2$  composition were prepared in glass-graphite crucibles under nitrogen atmosphere in RF furnace. The initial chemicals were previously sulfurized and were 99.99% pure.  $\text{Dy}^{3+}$  ion was added in the form of  $\text{Dy}_2\text{S}_3$  in 0.1÷1 mole % of concentration. The samples were optically clear and had light yellow coloration.

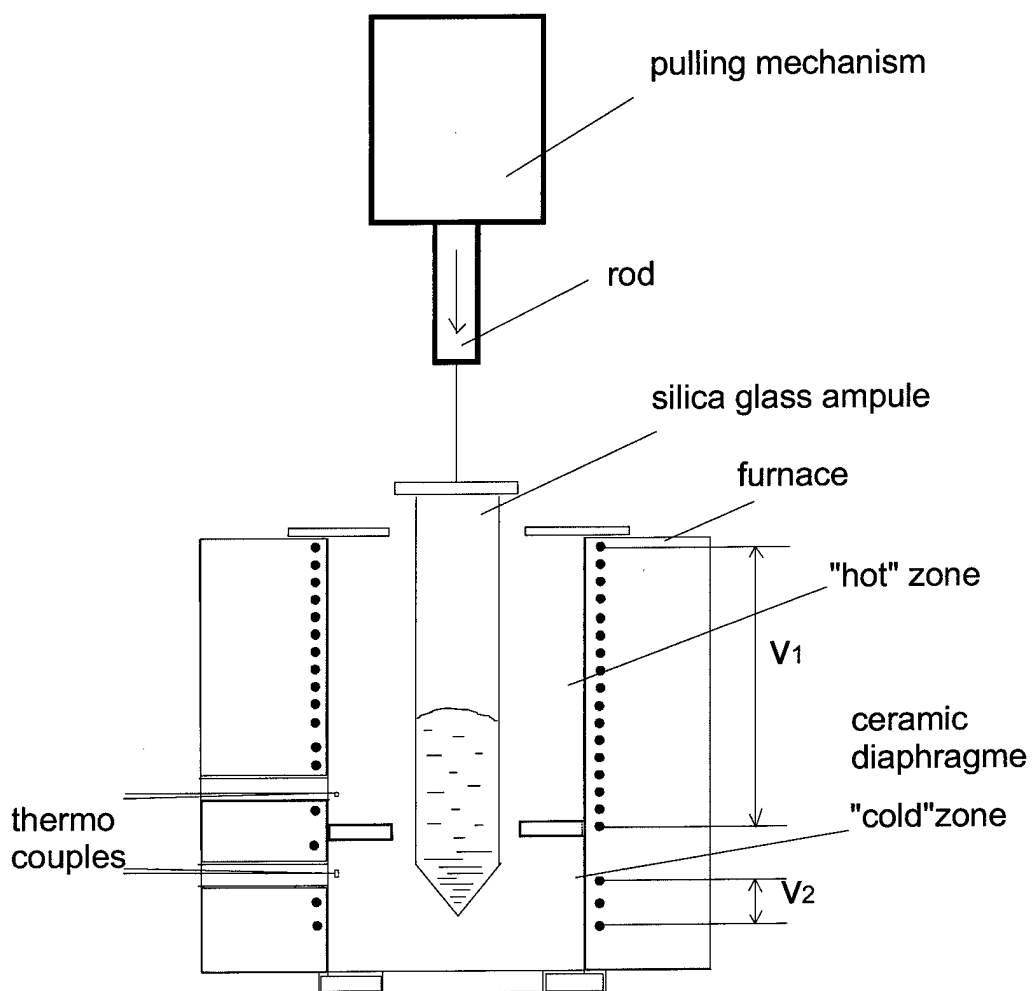


Fig. 9.7 The scheme of set up for growth the  $\text{KPb}_2\text{Cl}_5$  single crystals

### References to chapter 9.

1. I.V. Stepanov, P.P. Feofilov, Crystal growth, Proc., v.1, Ed. Acad. nauk SSSR, M., 1959, p.115
2. L.M. Shamovskii, Yu.N. Jvanko, Materials of VII Conference on Luminescence (crystallophosphors), Ed. Acad. nauk SSSR, Tartu, 1959, p.66
3. O.G. Poliachenok, Inorganic materials, 11 (1966) 958-965
4. P. Gorlich, H. Karras, R. Reiman, Sitzungberichte der Deutschen Akademie der Wissenschaften zu Berlin (Math. Phys. Techn.), 3 (1960)
5. Yu.K. Voronko, V.V. Osiko, V.T. Udovenchik, M.M. Fursikov, Sov. Solid State Physics, v.7, 1965, p.267
6. B.P. Sobolev, K.B. Seiranian, L.S. Garashina, P.P. Fedorov, Journal of Solid State Chemistry, 28 (1979) 51-58.